UNIVERSITA' DI BOLOGNA

ALMA MATER STUDIORUM

DOTTORATO DI RICERCA IN INGEGNERIA ELETTRONICA, DELLE TELECOMUNICAZIONI E TECNOLOGIE DELL'INFORMAZIONE (ET-IT)

Ciclo XXX

Settore Concorsuale: 09/F1 Campi Elettromagnetici

Settore Scientifico Disciplinare: ING-INF/02 Campi Elettromagnetici

Radio Channel Characterization for Future Wireless Networks and Applications

Presentata da:
Ing. Marco ZOLI

Supervisore:
Dr. Franco FUSCHINI
Co-Supervisori:
Dr. Marina BARBIROLI
Prof. Vittorio DEGLI ESPOSTI
Dr. Enrico M. VITUCCI
Coordinatore Dottorato:
Prof. Alessandro VANELLI

Esame finale anno 2018

"There is nothing noble in being superior to some other man; true nobility is in being superior to your previous self."

Ernest Hemingway

UNIVERSITA' DI BOLOGNA

Abstract

School of Engineering and Architecture
'G. Marconi' DEI

Dottorato di Ricerca

Radio Channel Characterization for Future Wireless Networks and Applications

by Ing. Marco ZOLI

The new frontier of Above-6GHz bands is nowadays revolutionizing the field of wireless telecommunications, requiring new flexible radio channel models to support the development of future Giga-bit-per-second systems. Recently, deterministic ray-based models as Ray Tracing are catching on worldwide thanks to their frequency-agility and reliable predictions. A modern 3D Ray Tracing developed at University of Bologna has been indeed calibrated and used to investigate the Above-6GHz radio channel properties. As starting point, an item-level electromagnetic characterization of common items and materials has been achieved successfully to obtain information about the complex permittivity, scattering diagrams and even de-polarization effects, both utilizing Vector Spectrum Analyzer (at 7-15GHz) and custom Channel Sounder (at 70GHz). Thus, a complete tuning of the Ray Tracing has been completed for Above-6GHz frequencies. Then, 70GHz indoor double-directional channel measurements have been performed in collaboration with TU Ilmenau, in order to attain a multidimensional analysis of propagation mechanisms in time and space, outlining the differences between Below- and Above-6GHz propagation. RT simulations compared to measurements have shown widely good results, especially thanks to the implementation of Effective Roughness model for diffuse scattering. Furthermore, multi-antenna systems, as Multiple-Input-Multiple-Output (MIMO) and Beamforming have been taken into considerations, as strategic technologies for Above-6GHz systems, focusing on their implementation, limits and differences. Finally, complex system simulations of Space-Division-Multiple-Access (SDMA) networks in indoor scenarios have been tested, to assess the capabilities of Beamforming. In particular, efficient Beam Search and Tracking algorithms have been proposed to assess the impact of interference on Multi-User Beamforming at 70GHz and, also, novel Multi-Beam Beamforming schemes have been tested at 60GHz to investigate diversity strategies to cope with NLOS link and Human Blockage events. Moreover, the novel concept of Ray-Tracing-assisted Beamforming has been outlined, showing that ray-based models represent today the promising key tools to evaluate, design and enhance the future Above-6GHz multi-antenna systems.

Acknowledgements

This work is the written evidence of the results achieved over three years of PhD made of research, studies and simulations. It has been a long journey and I think it is quite impossible to summarize the professional expertise I have been achieved, not only by means of hard work but especially interacting with people, especially my supervisors here in Bologna at Unibo. And I believe this is what makes the difference in the end. Also, thinking about the period abroad in Germany and the international meetings, it has been amazing to discover the passion and the dedication of the research community behind most of the presentations, papers or projects. Since the beginning of my PhD I have been welcomed as one of the "family" and this feeling is unique. I will be always grateful to Franco, Marina, Enrico and Vittorio.

Along the way I was never alone and I ought to say thanks to a lot of people: my "super-advisors": Dr. Franco Fuschini, Dr. Marina Barbiroli, Prof. Vittorio Degli-Esposti and Dr. Enrico Maria Vitucci, all the research group of Prof. Thomae in Ilmenau, all the research group of Prof. Kuerner in Braunschweig, all the people of Fondazione Ugo Bordoni at Villa Marconi, Prof. Alessandra Costanzo and Prof. Diego Masotti and all the community of the European COST (now IRACON) . Of course something special to the buddies of the "Shamenga" Lab: Francesco, Francesca, Marco, Giacomo, Massimo, Alex, Riccardo and Mazen. I would like also to thank Prof. Alberto Santarelli and Dr. Corrado Florian for their help with VNA measurements.

Contents

List of Abbreviations

PHY	Physical Layer
MAC	Medium Access Control
RAT	Radio Access Technology
WLAN	Wireless Local Area Network
mmW	Millimeter Waves
cmW	Centimeter Waves
MCS	Modulation and Coding Scheme
OFDM	Orthogonal-Frequency-Division-Multiplexing
PAPR	Peak-to-Average Power Ratio
BER	Bit-Error-Rate
PA	Power Amplifier
PAE	Power Amplifier Efficiency
VGA	Variable-Gain Amplifier
SNR	Signal-to-Noise-Ratio
SINR	Signal-to-Noise and Interference-Ratio
CINR	Carrier-to-Noise and Interference-Ratio
EVM	Error Vector Magnitude
NLS	Network Level Simulation
LLS	Link Level Simulation
FEC	Forward Error Correction
CSI	Channel State Information
SVD	Singular-Value-Decomposition
SISO	Single-Input-Single-Output
MIMO	Multiple-Input-Multiple-Output
STC	Space-Time Codes
MRC	Maximal-Ratio-Combining
DL	Dowlink
UL	Uplink
SU	Single-User
MU	Multi-User
RF	Radio-frequency
UE	User Equipment
BS	Base Station
TX	Transmitter
RX	Receiver
RR	Radio Resource
UWB	Ultra Wide Band
XHAUL	Front/Mid/Back-Hauling
RT	Ray-Tracing
CS	Channel Sounder
VNA	Vector Network Analyzer
CIR	Channel Impulse Response
DR	Dynamic Range

CDF	Cumulative Distribution Function
RMSE	Root-Mean-Squared Error
WRMSE	Weighted RMSE
BF	Beam-Forming
FOV	Field-of-View
LOS	Line-of-Sight
NLOS	Non-LOS
MBF	Multi-Beam BF
SBF	Single-Beam BF
HPBW	Half-Power-Beam-Width
DS	Delay Spread, Diffuse Scattering
AS	Angular Spread
DPS	Doppler Spread
PDP	Power Delay Profile
PAP	Power Angle Profile
XPOL	Cross-Polarization
CPOL	Co-Polarization
XPD	Cross-Polarization Discrimination
XPI	Cross-Polarization Isolation
SMC	Specular Multipath Component
DMC	Diffused Multipath Component
AOA	Angle of Arrival
AOD	Angle of Departure
EIRP	Equivalent Isotropically Radiated Power
RCS	Radar Cross Section
FDTD	Finite Difference Time Domain
GTP	Geometrical Theory of Propagation
GTD	Geometrical Theory of Diffraction
UTD	Uniform Theory of Diffraction
ER	Effective Roughness
KA	Kirchoff Approximation
ITU	International Telecommunication Union
IMT	International Mobile Telecommunications
3GPP	3rd Generation Partnership Project
ISM	The industrial, scientific and medical radio bands
WRC	World Telecommunication Conference

Introduction

The major aim of this work has been tackling the new frontier of "Above-6GHz" bands for future wireless applications from an electromagnetic and propagation point of view. The novel access to unusual chunks of spectrum (e.g. 28GHz or 60GHz) is triggering worldwide a revolutionary progress in the telecommunications field opening many opportunities, but raising new challenges. In particular, the properties of the radio channel Above-6GHz still need to be deeply investigated, especially for modern solutions with Multiple-Input-Multiple-Output (MIMO) and Beamforming (BF) techniques. Therefore, mmWaves measurement campaigns (around 60/70GHz), in collaboration with TU Ilmenau, and Ray Tracing (RT) simulations have been performed to analyze the nature of Above-6GHz radio channel, addressing some of the actual open issues regarding the multipath richness, diffuse scattering, dielectrics electromagnetic characterization and Beamforming applications.

In order to track the logic progression of the thesis everything is organized in this way:

- chapter (1) introduces the actual wireless technologies and systems, providing the right insights to remark the importance of Above-6GHz bands for new applications in future mobile networks.

- chapter (2) outlines the basics of radio channel characterization taking into account the challenges related to Above-6GHz frequencies. Different approaches, as ray-based models, are outlined and compared.

- chapter (3) focuses on the Geometrical Theory of Propagation and RT implementation in details, showing the advantages of deterministic channel models for Above-6GHz characterization.

- chapter (4) describes the study of electromagnetic properties of materials and objects at Above-6GHz bands. Two different experimental approaches are presented: a Vector Network Analyzer wide-band measurement campaign at 7-15GHz and a Channel Sounder (CS) measurement campaign in anechoic chamber at 70GHz. Also a unique collection of electromagnetic parameters is provided.

- chapter (5) includes a deep analysis of 70GHz radio channel in a small office scenario, comparing CS measurements to RT simulations. The properties of propagation mechanisms are evaluated in time and space domains.

- chapter (6) provides the basics of Multi-Antenna systems and their relationship with Above-6GHz frequencies.

- chapter (7) addresses the impact of BF on Above-6GHz indoor communications. In particular, a study on Multi-Beam BF and a study on Multi-User BF are presented. Moreover, RT tool is tested as a key enabler to assist BF schemes.

- Appendix includes extra details about RF Hardware issues of Above-6GHz multi-antenna circuits.

Chapter 1

Future Wireless Systems

1.1 Introduction

Over the last 8 years, I have made up my mind that "the next big thing" to come for the technology progress could not be a disruptive innovation but more likely a sophisticated seamless integration of different applications. By checking the trendy buzzwords which are currently dominating the Information and Communication Technology (ICT) business there are indeed: 5G, Internet of Things (IOT), Augmented/ Virtual/ Mixed Reality, Industry 4.0, Autonomous cars, Artificial Intelligence (AI) and so on. In my opinion, a key role will be played therefore by the wireless communications enabling the convergence of all of these emerging novelties into a valuable ecosystem.

In fact, clear technical guidelines are provided by International Telecommunication Union (ITU) agency, as documented by the ITU Report [1], to improve the performance of the International Mobile Telecommunications (IMT) and setting new ambitious goals for the incoming 2020, in line with the progress of the European Framework Horizon 2020 [2] in Europe.
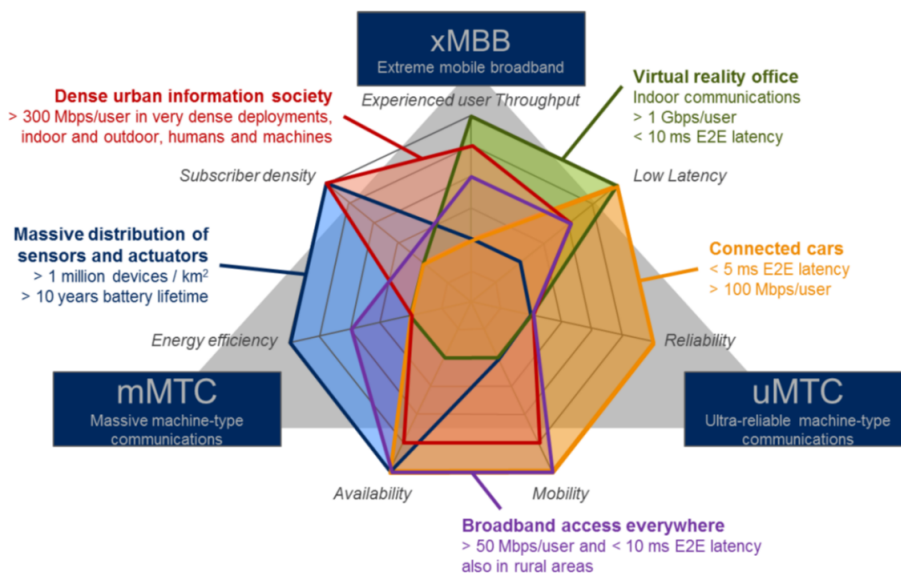

FIGURE 1.1: Different IMT2020 specifications for eMBB, URLLC and mMTC.

This is leading to the coordinated development of new communication types (Fig.1.1), defined as: enhanced mobile broadband (eMBB) for high speed links, ultra-reliable and low-latency communications (URLLC) for fast reliable connections, and massive machine type communications (mMTC), for huge numbers of monitoring

sensors (e.g. within the IOT paradigm). So, technically, a worldwide research effort in academia and industries is being carried out to achieve better user data rate, spectral efficiency, network capacity, energy efficiency and also service latency and reliability.

In fact, today, due to recent capacity-hungry mobile-based applications (e.g. videos streaming and social networks) the wireless bands so far utilized (e.g 0.7-6GHz) are becoming saturated and interference-limited. New upcoming radio systems, as 5th generation (5G), are envisioned to largely benefit from all available spectrum options from 500MHz to 100GHz, including licensed, unlicensed and license-shared access to radio channel. It is therefore worth introducing now a terminology to distinguish frequencies: 'Below-6GHz' and 'Above-6GHz'.

1.2   Below-6GHz Systems

Chasing the evolution of mobile communications in next years it is firstly necessary to speak about the work of 3rd Generation Partnership Project (3GPP) which unites seven telecommunications standard development organizations, and develops technical specifications, as [3], for complete end-to-end cellular systems including the user equipment (or devices), radio access, core network, and service framework. Since Release 8 in 2006, 3GPP has been working on LTE 4G, then on LTE-Advanced and now on bridging the gap towards the 5G, as recently published in Rel.15 [4].

As stated in papers by Ericsson [5], Motorola [6] and Agilent [7], "the main ingredients" of Radio Access Technology (RAT) for LTE communications today are Multiple-Input Multiple-Output (MIMO), Carrier Aggregation (CA) and Orthogonal Frequency Division Multiplexing (OFDM), besides other innovative network solutions, with respect to the "old" 3G. Respectively, by utilizing more antenna ports (e.g. multi-antenna systems), more separate or adjacent channels and more orthogonal sub-carrier signals, (as explained by Michailow [8] and Banelli [9]), it is possible to improve significantly the overall radio performance and reach practically hundreds of Mbps over the air. The spectrum bands implied in LTE span from 700 MHz to 2.6 GHz in Europe, staying Below-6GHz.

On the other hand, in order to get the whole picture it is secondly necessary to speak about the IEEE 802.11 standards. Indeed, Wi-Fi ®Alliance is the worldwide network of companies that defines innovative, standards-based Wi-Fi technologies and programs, certifies products. Since the first standard IEEE 802.11a in 1999, the Wi-Fi has experienced an exponential spread thanks to the usage of internationally unlicensed industrial, scientific, and medical radio band (ISM band). Respectively, the IEEE 802.11n [10] at 2.45GHz and the IEEE 802.11ac [11] at ~5GHz represent today the dominant standards for Wi-Fi. The technical specifications share again the same key wireless technologies of LTE (e.g. MIMO and OFDM), which are going to be further improved according to the accomplishment of future Wi-Fi generation (NG) as IEEE 802.11ax foreseen to bring Gbps data rate by 2019 [12]. The Wi-Fi spectrum is split around 2.4GHz and 5.8GHz, again Below-6GHz.

1.3   Above-6GHz Systems

In compliance with ITU World Radiocommunication Conference (WRC) in 2015 [13], in order to satisfy the aforementioned IMT2020 specifications, new bands up to 100GHz are meant to be allocated to mobile communications, as shown by Fig.1.2.

Technically, the lower part of spectrum from 6 to 30GHz is named as 'cmWaves' and the upper part from 30 and 100GHz 'mmWaves', due to the wavelength.
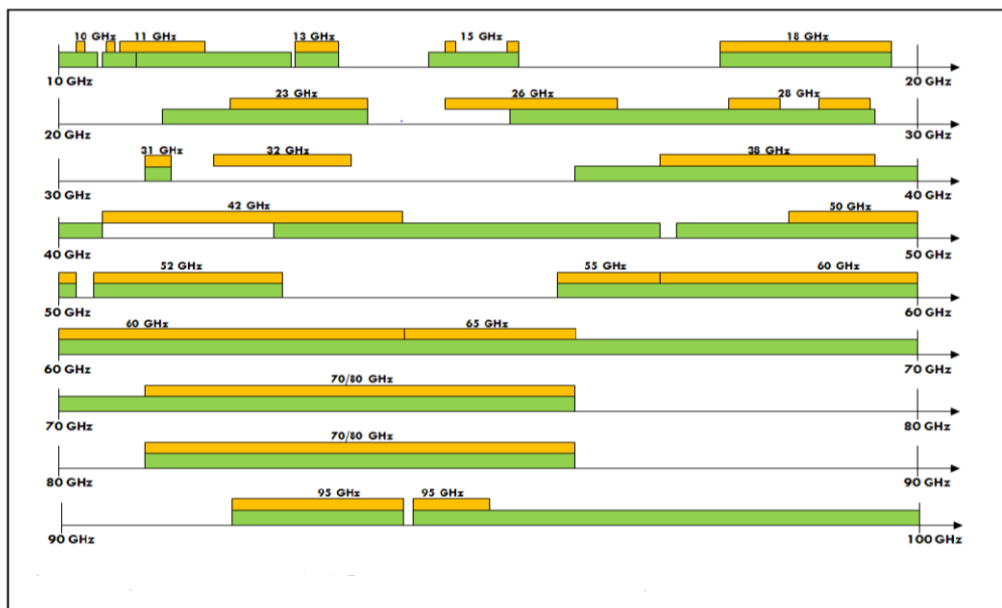
FIGURE 1.2: Possible new Above-6GHz bands for IMT2020 in Europe.

Recently, the feasibility of the proposed Above-6GHz wireless communications generated a debate in the scientific community, due to the novel idea to use higher frequency carriers and cutting-edge RF circuits with respect to the ones related to common 'legacy' lower bands. Today it is clear that cm/mmWaves are going to radically change the state-of-the-art of modern mobile communications in short-medium run, leading to a shift in the paradigm of designing wireless devices or networks, as reported by Rappaport [14], [15], [16] and by Samsung [17], [18], [19].

Attention is today especially drawn by 5G. In occasion of the XXIII Olympic Winter Games in PyeongChang in February 2018 the South Korean TLC operators, announced to realize the first demonstration of real-time 5G network exploiting Above-6GHz frequencies (i.e. 28GHz). However the decision about which bands are more suitable for 5G is a hot point of contention both from business and technical perspectives. The planned WRC 2019 will be likely to be decisive.

Exploring the new frontier of Above-6GHz, indeed, many research projects (within the overall EU Horizon 2020 5G Public Private Partnership) have started and are currently ongoing to find novel solutions :

- Metis II, [20]: Mobile and wireless communications Enablers for Twenty-twenty (2020) Information Society-II.

- mmMagic [21]: mm-Wave based Mobile Radio Access Network for 5G Integrated Communications.

- FlexWare [22]: Flexible and efficient hardware/software platforms for 5G network elements and devices.

- 5Gnow [23]: 5th Generation Non-Orthogonal Waveforms for Asynchronous Signalling.

- MiWeBa [24]: Millimetre-Wave Evolution for Backhaul and Access.

- XHaul [25]: Dynamically Reconfigurable Optical-Wireless Backhaul/Fronthaul with Cognitive Control Plane for Small Cells and Cloud-RANs.

In order to introduce the several issues related to radio channel characterization and waves propagation prediction Above-6GHz, an example of non-standalone 5G deployment is sketched in Fig.1.3, where mmWaves are used both for access and back-hauling: the Macro Base Station (BS) is an existing 4G BS (e.g. called eNodeB technically) covering a large area with usual 1-2GHz bands, whereas the mmWaves Small Cell is a new radio terminal around 28 or 60GHz for short distances links, according to the concept of cellular network densification. In this case, lampposts are hosting 5G BS to provide mmWaves radio access along the streets avoiding the costs of new installations.

In figure, the user device (e.g. UE) is connected both at 4G and 5G: mmWaves U-plane (i.e. User Plane, for the users traffic) indicates 5G Gbps links Above-6GHz, whereas Cellular C-Plane (i.e. Control Plane, for network signaling) indicates 4G Mbps links Below-6GHz. Moreover, thanks to the free bandwidth and directive antennas, mmWaves band is used also for backhauling (XHAUL), which is the fundamental communications between 5G BS and 4G BS for the overall network coordination. Considering the demand of data rate, this double advantage of cm/mmWaves could be very important providing Gbps services/applications and, at the same time, avoiding bottleneck effects, thanks to valid front/back-hauling capabilities.
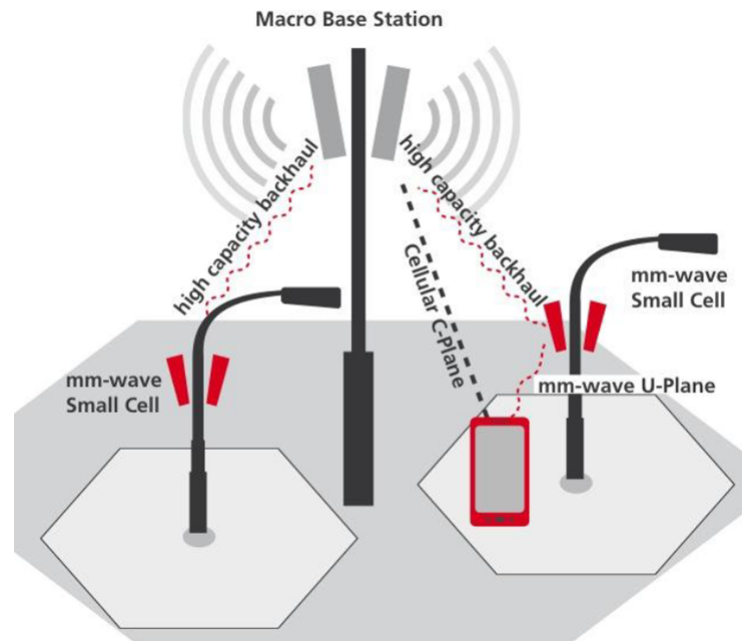
FIGURE 1.3: An example of 5G radio access.

Moreover, it is noteworthy to focus attention onto the novel ISM mmWave band centered around 60GHz, chosen to host very high data rate Wi-Fi according to the standard IEEE 802.11ad, named also WiGig ®[26] since 2012, similarly to IEEE 802.15.3c [27]. Even though a few WiGig compliant products are already commercially available today, an enhanced version of the 11ad, called 802.11ay or NG60 [28] is under development for 2019 targeting tens of Gbps over the air. This fact shows that even

in the Wi-Fi ecosystem, Above-6GHz bands represent again the key to reach unbelievable data rate far away from crowded usual frequencies.

This is confirmed by the following Fig.1.4, illustrating the well-known Edholm's Law about the trend of increasing data rate from 1970 to 2020, where, for example, 802.11ad overcomes all the other previous wireless technologies with more than 1Gbps.
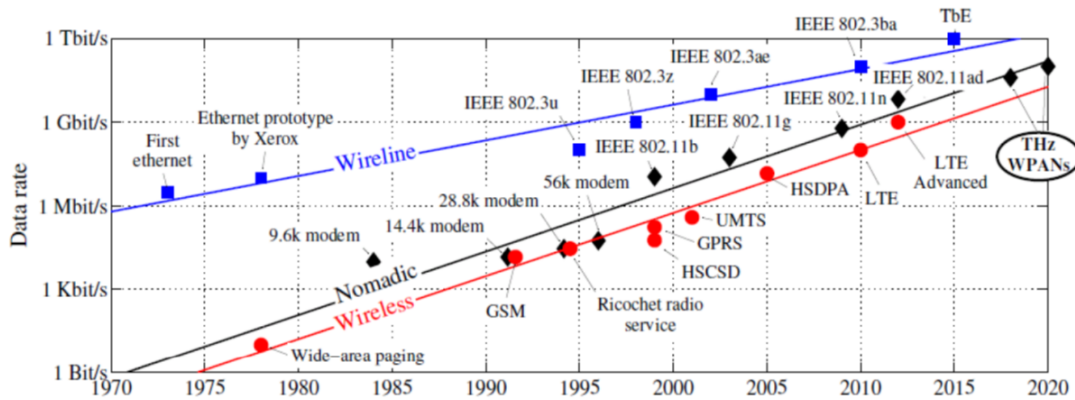
FIGURE 1.4: Edholm's Law for wired and wireless technologies.

1.4 Propagation and RF issues for Above-6GHz

Beyond the general outline about the state-of-the-art of current wireless communications, the main focus of the this work is to point out the main differences between Below-6GHz and Above-6GHz from an electromagnetic perspective, i.e. in terms of radio channel properties, material characterization, propagation and multi-antenna solutions.

Thus, with respect to Below-6GHz, cm/mmWaves differ for the following aspects:

- Spectrum: from 6GHz to 100GHz there are many spectrum portions available to be reserved primarily to mobile communications, as reported by Fig.1.2. The main problem is represented by the management of new spectrum in terms of license and permission, in order to harmonize worldwide the usage of these high-frequency bands for different applications. For example, the WiGig 60GHz ISM band is free and available in every country. Differently, the 'popular' candidate bands for 5G are nowadays primarily 28 and 38GHz and then 60 or 70/80 GHz, too. As shown before by Fig. 1.3, the first ones are likely to be for radio access and the second ones for back/front-hauling. These issues are still to be finalized by 2020.

- Bandwidth: being the carrier frequency in the order of tens of GHz at cm/mmWaves, the corresponding available bandwidth can reach up to GHz, so enabling Gbps data rate, in the end. For example, the whole bandwidth of WiGig is set from 57GHz to 70GHz with 6 channels of 2.17GHz of bandwidth. Anyway, it is worth noticing that the relative bandwidth is approximately the same between Below- and Above-6GHz: $100 * (80MHz/2450MHz) = 3.3\%$ and $100 * (2GHz/60GHz) = 3.3\%$.

- Antennas: due to the shorter wavelength, the antennas at cm/mmWaves can be designed with a compact layout placing more radiating elements in a given

area, Hong [29] and Yu [30]. The novel chance to implement 'massive' antenna arrays, especially at mmWaves, is a key aspect to be remarked because it is necessary for MIMO and BF techniques, as illustrated in chapter (6), and, secondly, it is the solution to cope with extra attenuation due to the propagation nature of higher frequency, with respect to 1-2GHz, (see next chapter (2)).

- Radio Channel: using frequencies higher than usual bands, there are big differences in the way how electromagnetic fields interact with the surrounding environment, as reported by Martinez-Ingles [31]. The right power balance among the fundamental propagation mechanisms (i.e. Reflection, Transmission, Diffraction and Scattering) is likely to be radically different, with respect to the actual knowledge Below-6GHz, as explained in chapter (5) with double directional 70GHz measurements. For example, being the penetration loss from outdoor to indoor (O2I) proportional to the frequency, can be prohibitive at cm/mmWaves to trespassing walls or obstacles, Diakhate [32]. This is a disadvantage for coverage purposes limiting the link distance to shorter path (e.g. 200-300m). An other open issue is represented by the impact of diffuse scattering, as explained in chapter (4), because details of buildings, streets and objects (e.g. terraces, roofs, poles, panels, vegetation, superficial roughness, volume inhomogeneity and so on), cannot be neglected at cm/mmWaves, due to the shorter wavelength, being responsible of important changes in the radio channel. Concluding, a vast comprehension of cm/mmWaves radio channels is yet far to be completed and further investigations are necessary.

- Noise and Interference: in RF circuits being the noise proportional to the frequency / bandwidth it limits the receiving sensitivity setting an upper bound in the link distance (given a fixed transmitted power output). On the other hand, thanks to MIMO/ BF schemes, the interference can be smartly rejected exploiting the properties of the radio channel in the spatial domain, as explained in chapter (6). So, combining these two facts, cm/mmWaves systems (with large bandwidth and adaptive BF) are likely to be noise-limited rather than interference-limited, Larsson [33]. In fact in Below-6GHz bands (let's think about the overcrowded 2.45GHz) the scarcity of radio resources (RR) represent today a bigger problem rather than complexity or costs, at expense of interference. A large number of antennas on both base stations and terminals is an essential characteristic of cm/mmWaves systems, but leading to an increased complexity of the RF front end due to architecture with multiple RF chains, as outlined in (6) and Appendix.

Chapter 2

Radio Channel Modelling

2.1 Channel Modelling

The term 'Channel Modelling' indicates generally the study of the modifications in terms of carried energy and/or information experienced by a given signal traveling through a medium (e.g. air) between two given points, a transmitter (TX) and a receiver (RX). In practice, the radio waves signals undergo a complicated "pinball" effect in real scenario, such as urban cities or indoor offices, where several surrounding entities (e.g. hills, buildings, trees, crossroads, walls, cars, pedestrian and pieces of furniture) obstruct and alter the propagation significantly. This aspect is named as multipath and may provoke the dispersion of the original signal in time and in space, then making the reception much harder with respect to the ideal free space Line-of-Sight (LOS) case, as described by Parson [34] and Bertoni [35]. Operatively, the purposes of Channel Modelling are to model the propagation of electromagnetic waves in order to develop algorithms and architectures, to perform link and system level feasibility studies and to investigate spectrum engineering regulatory issues, such as interference risks and coexistence.

In particular, in order to test modulation and coding scheme (MCS) or Medium-Access-Control (MAC) layer solutions, usually Network Level Simulator (e.g. NS-3 [36]) or Link Level Simulator are used to estimate network or link performance, respectively. Within these software, the radio channel model is the inner block in the physical layer (PHY) which provides reliable 'in-out' relationships among any terminals or communicating antenna ports. An accurate radio channel model is therefore essential to predict correctly the influence of real outdoor/indoor scenario on the radio signal integrity. In fact, radio channel impairments, as multipath, are significantly dominant in the evaluation of common link performance metrics as Signal-to-Noise-and-Interference-Ratio (SINR), Bit-Error-Rate (BER), effective Throughput and Error Vector Magnitude (EVM), as documented by Proakis [37] and Molish [38]. This is especially true in case of mobility of terminals and/or in case of crowded scenarios with vehicles and people, where both characterization and simulation of the radio channel become very demanding, due its a time-variant nature.

Recalling now the insights of the previous chapter, concerning the future requirements of wireless network it is worth tackling separately two remarkable trends in channel modelling:

- Above-6GHz frequencies: with respect to lower frequencies, at higher bands, as 28GHz or 60GHz, the radio channel shows different properties, which are still to be fully understood, as described in chapter (5). Approximately, assuming that the behavior of e.m. waves around 1GHz is much similar to FM radio whereas around 100GHz is similar to visible light, then it is clear the need for channel models capable to cover large frequency span with a sort of

'frequency-flexibility', taking into account carefully the frequency-dependent propagation differences. For example, a piece of furniture like a monitor, which could be considered negligible at 1GHz, may instead block and/or scatter part of the incoming power at mmWaves, due to the shorter wavelength.

- Multi-antenna technology: on the other hand, over the last decades novel architectures with multiple antenna at radio terminals have been adopted to achieve beneficial improvements in terms of power (e.g. Beamforming) and/or data rate (e.g. MIMO Spatial Multiplexing), as reported in chapter (6). In a nutshell, these multi-antenna technologies require a complete knowledge of the radio channel not only based on power levels, but on spatial-temporal (multi-dimensional) characteristics of multipath, due to multiple-antenna ports. In order to evaluate the performance of Gbps MIMO networks (e.g. 5G or NG 802.11) it is clear that the characterization of new radio channel should take into account also these advanced aspects of modern radio communications.

2.2   Different Approaches of Modelling

The ultimate goal of an ideal model would be showing the same results with respect to on-field measurements. Statistically speaking, this comparison is usually carried out over many different TX/RX locations and the corresponding accuracy is assessed in terms of prediction error (e.g. mean and standard deviation errors). Above-6GHz multi-antenna systems require also the joint evaluation of multi-dimensional and multi-antenna characteristics of radio channel so making even more challenging the matching between model and measurement results.

Therefore, generally, due to the complexity of propagation phenomena, every channel model shows indeed a point of trade-off between complexity and precision, offering pros and cons depending on its application. A simple classification based on the two different approaches is outlined in the following.

2.2.1   Measurement-First approach

Measurement-First approach means that the radio channel is sounded according to a planned measurement campaign and then a related model with several statistical parameters is extracted thanks to the data analysis. In the past this empirical/experimental approach used to be the way to test radio channels (e.g. Okumura-Hata) and is still fundamental for any wireless system validation. Within the research community, there are two main approaches in channel sounding: commercially available vector network analyzers (VNA) and custom channel sounders (CS). The VNA is a simple solution, which is typically used in indoor and stationary scenarios, working in the frequency domain. However, due to the greater measurement bandwidth in comparison to lower frequencies, it may be time consuming. Conversely, custom CS based on wideband signal, as pseudo random binary sequence (PRBS), although more expensive, offer a high resolution in the time delay domain, combined with a high spatial resolution, allowing for an easier identification of clusters and paths. Moreover the time variant aspects of the radio channel, as Doppler effect, can be detected with CS, thanks to its similarity to radar equipment as illustrated in the following chapters.

Of course the price to pay for radio channel measurement derives from a 'double' cost: hardware must be purchased/manufactured and then a long period of time must be allocated to perform measurements in different scenarios.

For example, the mm-Magic project [21] gathers many measurements campaigns performed in different out/in-door scenarios and, at different cm/mmWaves bands of interest covering the 6-100GHz spectrum. The final model is a so-called stochastic channel model (SCM): in a nutshell, as depicted in the flow chart in Fig.2.1, given the inputs about the scenario and the link set-up, a multi-stage simulation procedure generates realizations of several channel coefficients, differentiated as large and small scale fading parameters, Parson [34]. The entire set of these parameters represents the model of the radio channel which is flexible and capable to replicate the measured radio channel in terms of Channel Impulse Response (CIR) as accurate as possible, taking into account the propagation losses, temporal-angular dispersion, array antenna model, users mobility and even blockage events.
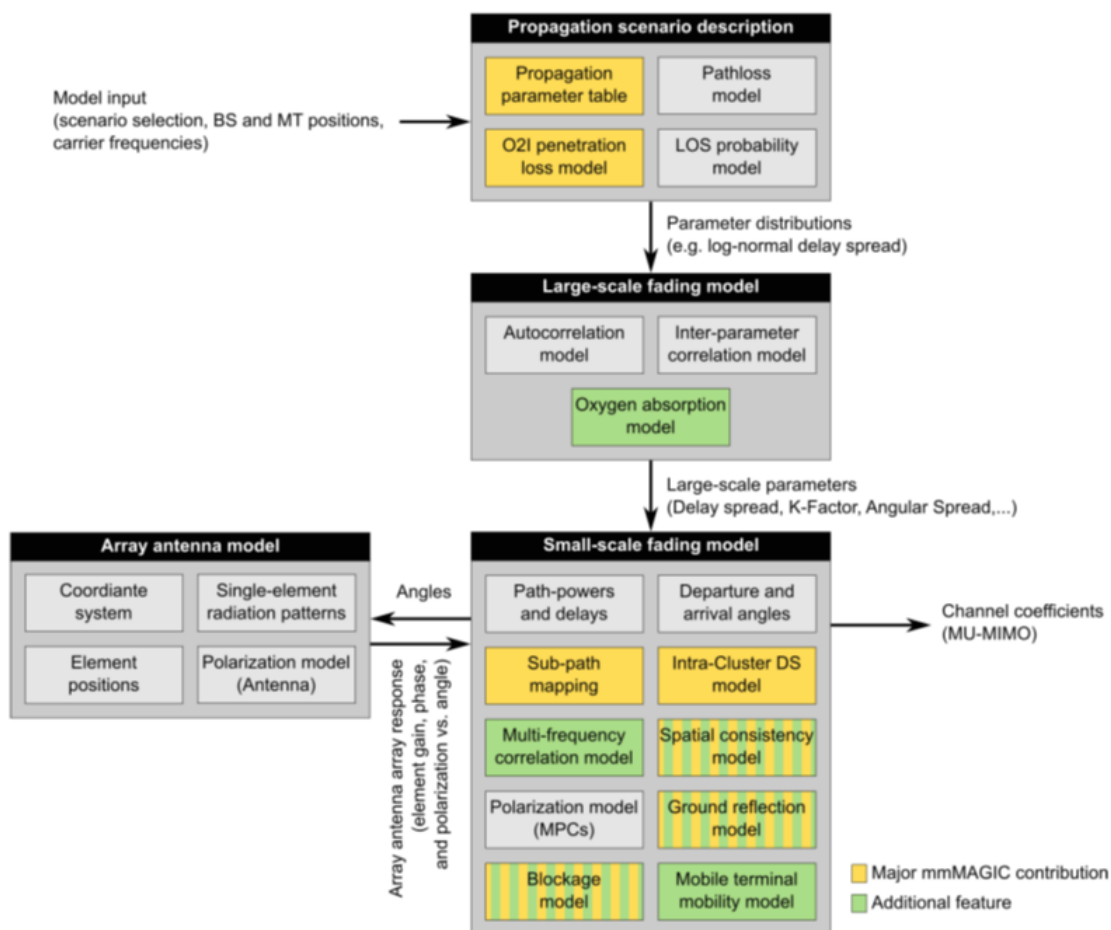
FIGURE 2.1: Flowchart of stochastic radio channel model of mm-Magic project. Notice the Array antenna model block on the left.

2.2.2 Physics-First approach

Physics-First approach is based on the application of the electromagnetic theory (e.g. Maxwell equations), to model the radio waves interactions and propagation. Now, measurements are needed additionally to calibrate the models, afterwards. Practically two 'families' of numeric simulators within the field of Computational Electromagnetics are available: so called full-wave algorithms, as FDTD or other numerical techniques, as illustrated by Ishimaru [39] and Sadiku [40], and ray-based models as Ray Tracing, Fuschini [41]. With respect to Measurement-First approach, the price

to pay for this approach is expressed by the simulations computational complexity and time. Regarding Above-6GHz, Physics-First models, as Ray Tracing, have the advantage to be flexible to simulate the radio channel at different frequencies (e.g. 6-100GHz) with no additional costs with respect to measurements, once a reliable tuning of the model itself is performed. In particular the calibration of the indoor Ray Tracing developed at University of Bologna is performed for the band 60/70GHz as described in the chapter (4).

2.2.3   Hybrid approach

Recently, concerning cm/mmWaves, novel interesting hybrid models have been proposed in order to merge the pros of Measurement-First approach (e.g. speed, simplicity) and Physics-First approach (e.g. frequency-agility, precision). In particular, in 3GPP TR 38.900 [3] is provided an alternative Map Based hybrid model where Ray Tracing/Launching tools take an active part in the channel coefficient generation procedure assisting the identification and manipulation of clusters, paths and subpaths of the multipath components. Similarly, an example is given by Fig.2.2, where the channel response generation is explained according to IEEE 802.11ay for indoor 60GHz communications. It is worth noticing the Ray-Tracer algorithm is a significant block in the initial part of the model procedure.
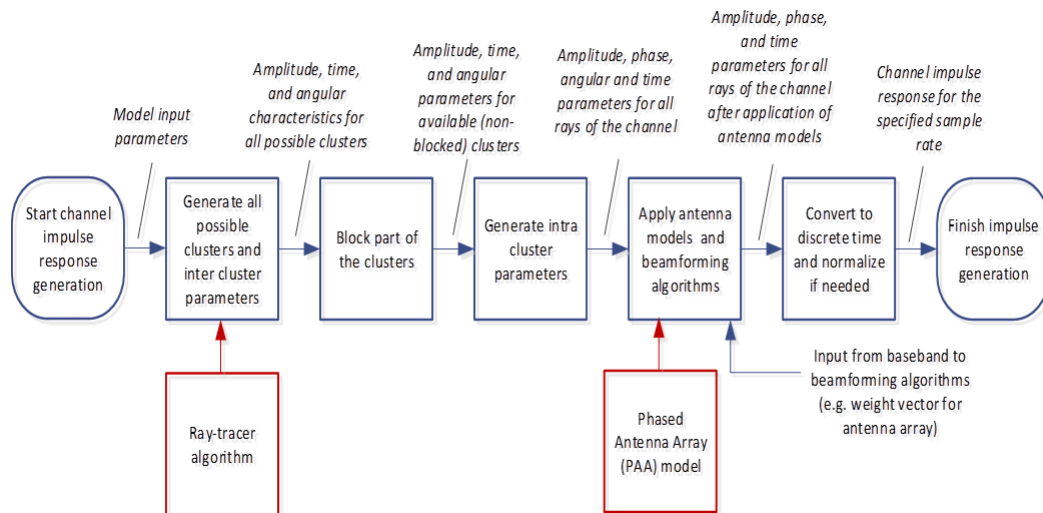
FIGURE 2.2: IEEE 802.11ay hybrid approach of channel modelling at 60GHz. Notice the Ray-tracer algorithm block on the left bottom.

Moreover, an other simple hybrid approach is the so-called quasi-deterministic (Q-D), proposed for modeling both access and backhaul mmWaves channels. The approach builds on the representation of the mmWaves CIR comprised of a few quasi-deterministic strong rays (D-rays), a number of relatively weak random rays (R-rays) and flashing rays (F-rays, originating by reflections from moving cars, buses and other dynamic objects), as in Fig.2.3. Also in this model deterministic elements as reflected rays are mixed with statistical elements as random decay paths to model as close as possible the mmWaves channel. See the MiWeBa project [24] for further details.
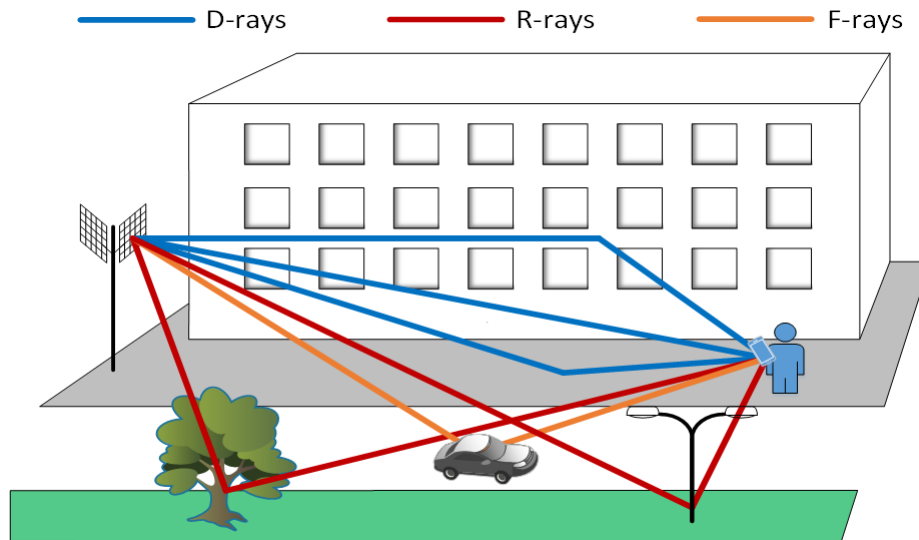
FIGURE 2.3: Q-D model: graphical representation of short-range link along the street with different interactions.

2.3 The Characterization of the Radio Channel Above-6GHz

As sketched before, the characterization of the radio channel is a wide topic that bridges the gap between the e.m. fields propagation mechanisms and the signals elaborated by the RF/digital circuits in any device. Since the radio channel has an unpredictable behavior due to multipath and mobility, it changes continuously its characteristics in time and space. This is one of the major reason why modern resilient wireless systems must 'adaptively' find the best communication settings. Practically, for example, LTE BS serves the network users managing the available radio resources (e.g. time subframes, frequency subcarriers, MIMO spatial streams and MCS) using a proper 'channel dependent' scheduler algorithm to cope with time-variant nature of radio channel. This confirms again the importance of radio channel modeling in many applications remarking overall the need of new Above-6GHz radio channel models.

In the following many different aspects of channel modelling are listed to take into account the novelties introduced by Above-6GHz bands.

- Antennas: due to the small wavelength at Above-6GHz, the RF front-end hosts antenna array enabling all the potentiality of BF e MIMO techniques, as discussed in chapter (7). Fig.2.4 shows an example of 60GHz antenna array with 24 elements made by Sibeam ®. As in Fig.2.1 and in Fig.2.2, the properties of the antenna arrays are part of the radio channel model because such smart antennas have the capability to spatially filter the multipath components, according to their radiation pattern and gain function. This is one of the biggest advantage of Above-6GHz systems implementing BF and/or MIMO.
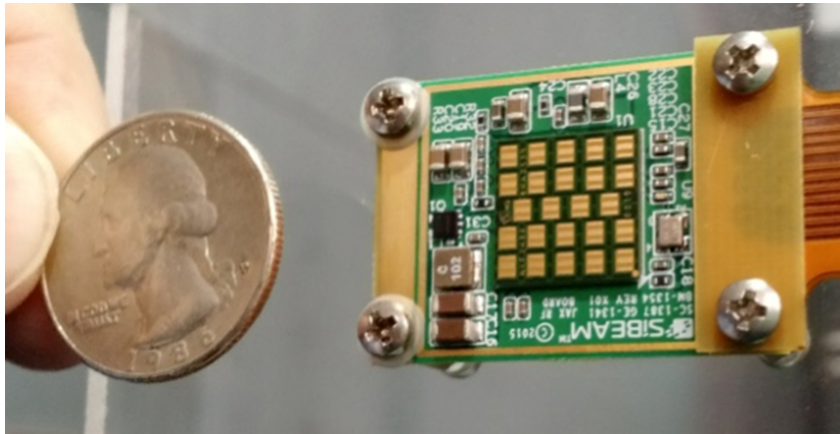
FIGURE 2.4: Sibeam ®60GHz antenna array.

- Free space path loss (FSPL): the power loss in free space is proportional to square of the frequency, due to the broadening of the wavefront. For example, going from 2GHz to 60GHz the FSPL increases 30dB, as confirmed by Martinez-Ingles [31]. This aspect could represent an issue for cm/mmWaves in terms of coverage and link budget. However with respect to Below-6GHz, at cm/mmWaves also the directivity and the gain of antennas increase significantly compensating the larger FSPL. Anyway the problem is not automatically solved. It is worth reminding that in order to properly use multi-antenna schemes onto the antenna array still precious information (e.g. Channel Information State) are needed to be retrieved (with a cost) and managed (with an unavoidable level of complexity). In a nutshell, in order to pilot with BF an antenna array, which may provide enough gain to overcome the FSPL, a terminal should know where to focus the power, and this is not a trivial task.

- Extra Attenuation: as explained in chapter (4), the higher the frequency the weaker the capability to penetrate and even pass thorough an obstacle. For cm/mmWaves this results in two big issues: a greater Outdoor-to-Indoor (O2I) attenuation which limits the link coverage limiting the Non-LOS communications and, then, an enhanced sensitivity to unexpected Blockage events, which may cause harmful drops of performance, as discussed in chapter (6). These are the reason why cm/mmWaves have been so far considered in 5G only for short-range radio access (e.g. hundreds of meter). However, the same aspect is instead an advantage to reduce unwanted interference in indoor communications, as investigated in chapter (7).

   On the other side, other minor effects as vegetation/foliage (see Fig.2.5) modelled in ITU Rec.833 [42] and climate phenomena modelled in ITU Rec.676 [43],840 [44],838 [45] could be included in the radio channel models Above-6GHz, especially for long-range links. For examples, at 60GHz there occurs an absorption peak due to the oxygen in the air which causes an additional attenuation equal to 15dB/km, which is 1.5 dB over 100m , or, moreover, considering a rain rate equal to 25 mm/hour the corresponding attenuation at 28GHz is about 7dB/km, which is only 0.7 dB over 100m.

FIGURE 2.5: Siradel ®Ray Tracing simulation of an outdoor long-range link. It is evident the rich presence of vegetation along around the buildings.

- Time-Angle dispersion: as stated in ITU Rec.1238 [46] and 1411 [47], the fluctuations of the received signal due to the evolving radio channel (i.e. called multipath fading) cause temporal and angular dispersion, Bertoni [35]. In time domain this means the overlapping of multiple replicas (e.g. rays or paths) of the original transmitted fields arriving with different time of arrivals onto the RX antenna. Delay Spread (DS) is commonly the spread coefficient used to quantify the impact of temporal dispersion. In space domain, equivalently, this means the overlapping of multiple replicas of the original transmitted fields arriving with different angle of arrivals onto the RX antenna. Angles Spread (AS) (often split into Azimuth and Elevation/Zenith angles) is commonly the spread coefficient used to quantify the impact of angular dispersion of the signal.

  Now, concerning Above-6GHz systems a very important role is played by antenna arrays and adaptive Beamforming scheme which are capable to mitigate the multipath fading. Instead of capturing the multipath components from all spatial directions, as well as Below-6GHz antennas, thanks to the greater directivity the antenna array can filter out spatially most of the incoming paths, focusing on the LOS dominant path, then reducing the dispersion of the signal received, consequently. All of this may end up in a temporal dispersion (e.g. delays of the signals) much shorter than the communication symbol time, preventing from Inter-Symbol-Interference (ISI), [34]. This advantage enables indeed Gbps data rate, as in 802.11ad, for example. Of course this is not the case of challenging NLOS cases, as documented in chapters (5) and (7).

- Frequency dispersion: with moving terminals the radio channel may be even affected by Doppler effect: because of the relative difference in speed between e.m. waves and mobile antennas, as well as for acoustic problems, frequency

shifts can occur at receiver side, causing impairments in the decoding / demodulation, especially in case of OFDM signals. This issue can have a significant impact on the quality of link especially for cars in highways, high-speed trains or even satellites. Doppler Spread (DPS), as well as DS and AS, is commonly the spread coefficient used to quantify the impact of frequency dispersion, Parson [34]. Doppler effect is overall more effective at cm/mmWaves communications since it is proportional to the carrier frequency. Doppler effect might be indeed 15-30 times greater at 28-60 GHz compared with Below-6GHz wireless systems.

- Blockage events: due to directivity of the antennas the cm/mmWaves links tend to be similar to optical ones with respect to Below-6GHz, reducing the negative influence of multipath but, at the same time, making the communication susceptible to unknown blockage events, which are hardly to be predicted and modelled. This issue depends mostly on the relative heights of the terminals. In fact, in outdoor scenarios the Base Station (e.g. eNodeB in LTE) is usually mounted on rooftop, whereas in indoor scenarios as office the Access Point (AP) is typically attached on a wall or located on a table. However, since the height of user device cannot exceed approximately 2 meters above the ground, approximately, moving cars/tracks or standing/walking people may shadow and block the communication paths, even in short range link. So, different blockage models have been proposed in literature for this purpose, including cylinders ([48]), slabs edges (Jacob [49]) or cuboids, mainly utilizing UTD, as Knife-Edge diffraction model. As reported by Jacob [50], a study on the Human Blockage (HB) has been performed with 60GHz measurements analyzing also the impact of skin and clothes. Fig.2.6 shows the shadowing losses (i.e. L_d in dB) due to HB presence on 60GHz: it is clear the "V-shaped" curve (i.e. black color) due to the obstruction of the LOS, with 40dB fade in the center and several ripples on the edges. In this study, multiple knife edge (MKE) model (i.e. red curve) has been compared to measurements and it is evident the good matching.
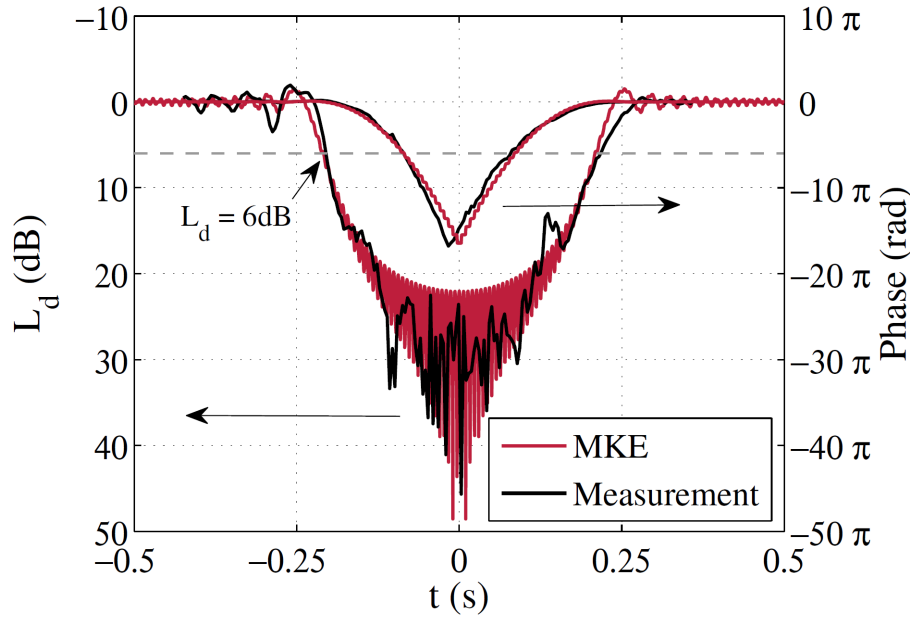
FIGURE 2.6: Human Blockage shadowing deep fade with power on
the left and phase on the right.

- Polarization: technically the radio waves, as well as light, can be polarized in 3 different ways: linear, circular and elliptical, tracing in the space respectively a line, a circle and an ellipse propagating along time. The polarization matching between the receiving antenna and the incoming paths with unknown polarization due to multipath, is generally an other important factor to be taken into account in channel modelling, because, hypothetically, the received power can drastically drop to zero in the worst case, Balanis [51]. The problem of polarization mismatch can be considered secondary at cm/mmWaves where the communication link, if possible, is based on the concentration of the power towards LOS direction, thanks to BF, as stated before. Differently, polarization decoupling can be harmful in NLOS scenario, depending on the antenna properties and on the number of the clusters / paths in the link. Furthermore, since the polarization state of the e.m. field Above-6GHz is more likely to be conserved with respect to lower bands due to the shorter wavelength, Co and Cross polarization properties of waves (Ludwig [52] and Roy [53]) can even be exploited to achieve diversity and multiplex signals, as reported in several works by Thompson in [54], by Kajiwara [55] and [56], by Manabe [57] and [58] and by Maltsev in [59]. Further insights about polarization are in chapter (4) and (7).

Chapter 3

Geometrical Propagation Theory: a ray-based perspective

3.1 Geometrical Propagation Theory

Geometrical Theory of Propagation (GTP) is the electromagnetic theory derived from Maxwell equations, which allows the description of electromagnetic propagation by means of optical rays (or just "rays") that can be properly traced between TX and RX. From a geometrical point of view, an optical ray is 3D line perpendicular in each point to the wave-front passing for that point. GTP may be exploited in different environments, form free space to complex scenarios with objects and obstacles around and in-between the antennas. In order to get a complete ray-based electromagnetic theory, two main issues must be addressed: 1) tracking of the rays trajectories: it is a purely geometrical problem, aiming at identifying the rays paths; 2) computation of the e.m. field: it aims at evaluating how the e.m. field evolves along the tracked rays.

The far-field of ideal source in free space is a spherical wave, i.e. wave-fronts are concentric spheres. Rays are therefore straight radial lines springing out from the source (Fig.3.1a), and their direction is therefore the direction of propagation.
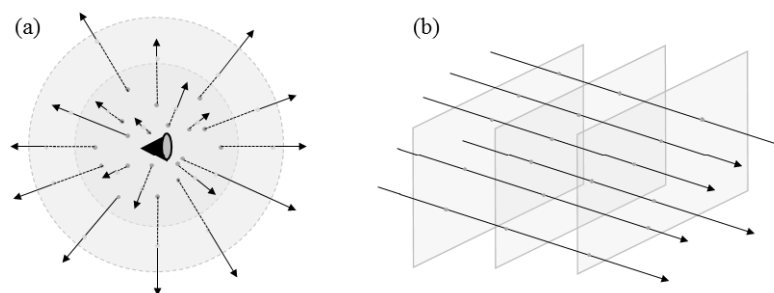
FIGURE 3.1: (a) Rays of spherical wave-front; (b) Rays of plane wave-front.

The plane wave solution of the Maxwell equations is also considered in Fig.3.1b, where the rays are clearly straight parallel line since the wave-fronts are parallel planes perpendicular to the direction of propagation. Considering the power carried by e.m. waves it is necessary to introduce the Poynting vector which represents the directional energy flux of an electromagnetic field. Now, the Poynting vector of a spherical wave is oriented towards the radial direction, which is the same direction of the optical rays. This means that rays are not just geometrical entities, but they have a clear, physical meaning, i.e. the power (e.g. W/m^2) carried by the wave propagates along the rays. In this regard, the magnitude of the Poynting vector is

often referred to as intensity of the ray indeed. Then, considering the field amplitude along a ray it is important to explain the concept of spreading factor.

With reference to Fig.3.2, let's consider a ray from P_0 to P, and a portion of wave-front around P_0 (with area Σ_0). The surface Σ_ℓ formed by the rays passing through the contour of Σ_0 intersect the wave-front containing P determining a second wave-front portion having area Σ. The closed surface made by the two wave-front sections Σ_0 and Σ plus the bunch of adjacent rays belonging to Σ_ℓ is known as ray tube (or tube of flux). Applying the power conservation law to the ray tube in case of vacuum, leads to the conclusion that the power coming into the tube across Σ_0 must be equal to the power outgoing through Σ.
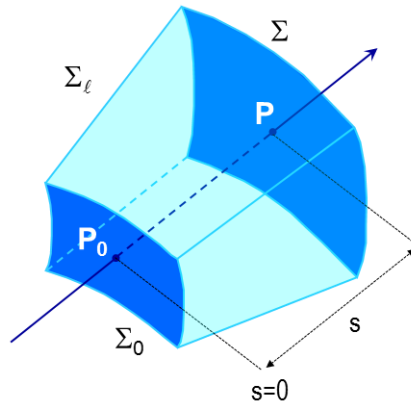
FIGURE 3.2: Ray Tube.

The spreading factor (SF) of the wave in the point P with respect to the reference point P_0 is then defined in the following, where **E** indicates simply the electric field and s the traveled path length:

$$ SF \equiv \lim_{\Sigma_0,\Sigma \to 0} \sqrt{\frac{\Sigma_0}{\Sigma}} = \sqrt{\frac{d\Sigma_0}{d\Sigma}} = \frac{\left|\vec{E}(P)\right|}{\left|\vec{E}(P_0)\right|} = \frac{\left|\vec{E_0}(s)\right|}{\left|\vec{E_0}(0)\right|} $$

Eq. 3.1

According to its definition, the SF relates the field amplitude in different point along the ray. In particular, for every real case $\Sigma_0 \leq \Sigma$, corresponding to $SF \leq 1$, the spreading factor accounts for the reduction of the field amplitude along the ray, due to the broadening of the wave-front area as the wave propagates into the medium. In a lossless medium, every wave-front carries the same power, which is distributed all over the wave-front surface. The larger the surface, the lower the field (ray) intensity, in order that the same overall power is preserved. Of course, if the medium is lossy, an additional intensity reduction is experienced along the rays, accounting for the partial conversion of the electromagnetic energy into heat (e.g. Joule effect). In a non-spherical case an infinitesimally narrow ray tube (as sketched in Fig.3.3) is in general "astigmatic", meaning that rays bounding the infinitesimal wave-front section $d\Sigma_0$ don not meet at a single point. Rather, 4 different focal points (C1-C4) can be highlighted, which furthermore determine 2 caustics (the lines C1C2 and C3C4). The distances of the reference point P_0 from the caustics (ρ_1 and ρ_2 in Fig.3.3) are the radii of curvature of the wave.
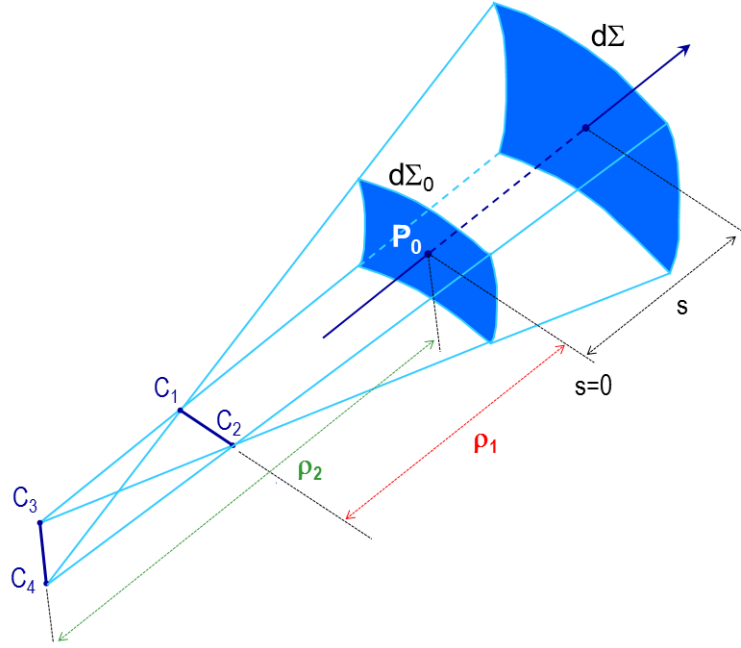
FIGURE 3.3: Astigmatic Ray Tube.

The wave spreading factor can be then expressed as follows, in general:

$$SF = \sqrt{\frac{\rho_1 \cdot \rho_2}{(\rho_1 + s) \cdot (\rho_2 + s)}}$$

Eq. 3.2

In the spherical case, $\rho_1 = \rho_2 = \rho$, being ρ the distance of the reference point from the source: a spherical wave has just a single focus in its phase center, whereas a plane wave has $\rho_1 = \rho_2 = \infty$, corresponding to SF = 1. This is physically sound, since the wave-fronts do not widen out in space (Fig.3.1b) and therefore the field amplitude does not change along the rays.

The previous considerations can be now collected all together in order to achieve a complete expression for the field propagating along a ray in a homogeneous medium:

$$\vec{E}(s) = \vec{E}(s = 0) \cdot SF \cdot e^{-j\beta s} = \vec{E}(0) \cdot \sqrt{\frac{\rho_1 \cdot \rho_2}{(\rho_1 + s) \cdot (\rho_2 + s)}} \cdot e^{-j\beta s}$$

Eq. 3.3

The field in point P is parallel (in the sense of complex vectors) to the field in P_0, i.e. they share the same polarization, and the field amplitude in P is reduced by a factor SF with respect to the amplitude in P_0. The equation includes a further phase relation, represented by the factor $exp(-j\beta s)$: as the field propagates along the ray, its phase undergoes a shift equal to '$-\beta s$', being s the traveled path length from P_0 to P and β is the propagation phase constant (named also k_0), equal to $2\pi/\lambda$, Balanis [60].

In order to apply GPT in real scenarios natural and man-made objects/obstacles need to be taken into account. Each object is usually assumed to be made of a homogeneous material, for sake of simplicity, and its electromagnetic properties are therefore taken into account by means of its (relative) electrical permittivity (ϵ) its (relative) magnetic permeability (μ) and its electrical conductivity (σ). In case of materials with frequency-dispersive behavior, different values of these parameter should be considered frequency-dependently (this could easily be the case of Above-6GHz bands). Furthermore, each object is also assumed to be formed by a finite number of flat-surface slab elements delimited by straight edges (Fig.3.4). The application of GTP in presence of objects therefore requires to give solutions to the following two issues: 1) change in the rays trajectories at the interfaces between different media; 2) assessment of the change (e.g. amplitude /phase/polarization) in the field value produced by the interactions. Variations in both the rays path and the field value depend of course on the kind of interaction, as depicted in Fig.3.4.
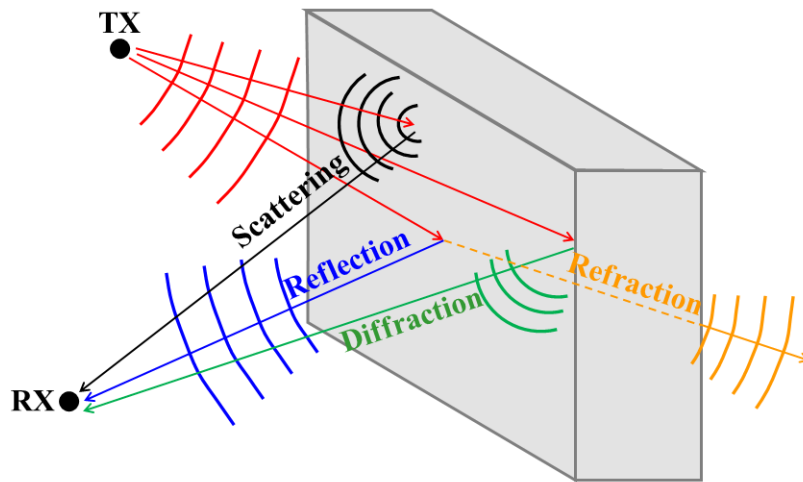
FIGURE 3.4:   Propagation Mechanisms: Reflection, Refraction, Diffraction and Scattering.

3.2   Propagation Mechanisms

Adopting a ray-based approach any complex interaction of the e.m. field can be decomposed into 4 different propagation mechanisms: Reflection, Transmission / Refraction, Diffraction and Scattering. Thanks to this concept of 'modularity' of the propagation mechanisms, deterministic ray-based models, as RT, are capable to handle complicated propagation problems simply by tracing the rays which bounce in the environment.

3.2.1   Reflection and Transmission

Reflection and Transmission or Refraction are usually treated together: reflection means a mirror effect and transmission is related to the penetration through the surface.

When a wave impinges on a flat, smooth surface, a reflected wave is generated in the backward half-space, as in Fig.3.5.
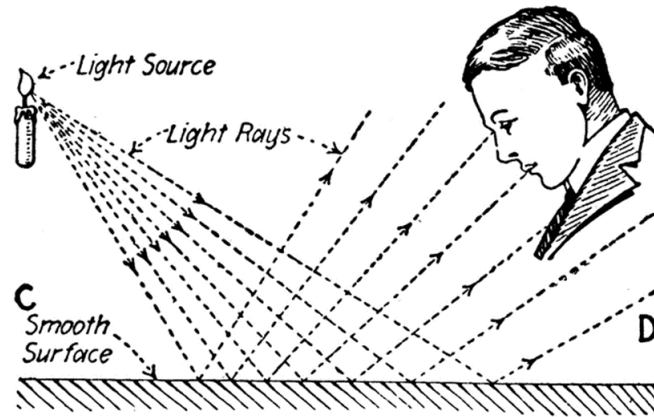
FIGURE 3.5: Reflection of light on smooth surface.

In particular, both the incident and the reflected rays belong to the same plane (incidence plane), where the direction of reflection is related to the direction of incidence through the well-known Snell law of reflection, Balanis [60]. The field value on the reflected ray just after the reflection point (Q_R in Fig.3.6) can be related to the incident field by means of a proper reflection coefficients (indicated with Γ in Eq.3.4) given by the well-known Fresnel equations, Balanis [60]. It is worth reminding that Fresnel coefficients need the knowledge of ϵ of the surface / object under examination. In particular, analytical expressions for the reflection coefficients are usually available for the TE polarization (incident and reflected electric field with linear polarization perpendicular to the incidence plane) and the TM polarization (incident and reflected electric field with linear polarization on the incidence plane). The combination of the two components of the field is given, as it follows in Eq.3.4, where Γ is the relative Fresnel reflection coefficient at the surface interface:

$$\vec{E}_r(Q_R) = \vec{E}_r^{TE}(Q_R) + \vec{E}_r^{TM}(Q_R) = \begin{bmatrix} \Gamma_{TE} & \Gamma_{TM} \end{bmatrix} \cdot \begin{bmatrix} \vec{E}_i^{TE}(Q_R) \\ \vec{E}_i^{TM}(Q_R) \end{bmatrix}$$

Eq. 3.4
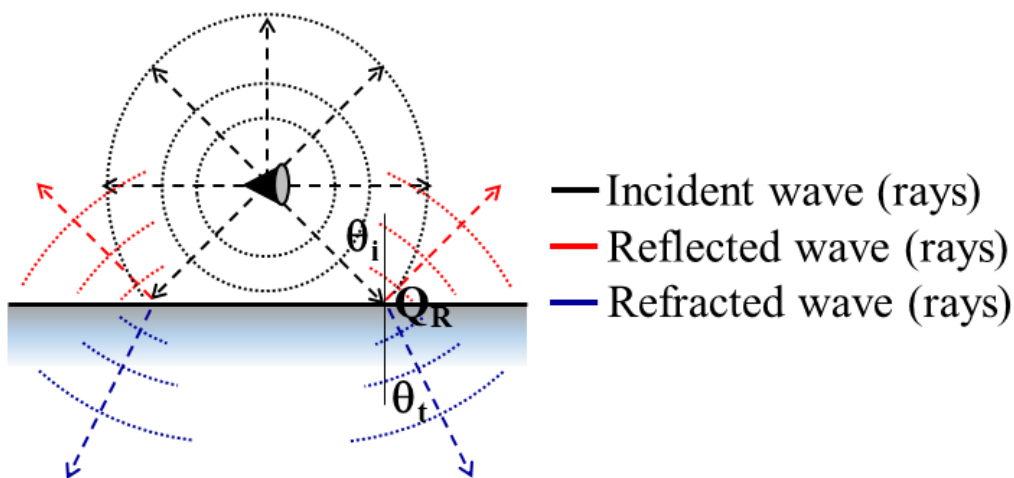
FIGURE 3.6: Reflections and Refractions from an ideal e.m. source.
Q_R is the point of interaction with the surface.

On the other hand, (Fig.3.6) the interaction between a wave (ray) and a smooth, planar boundary produces also refraction (or transmission), meaning that part of the incoming power can penetrate the interface between the two media going into the forward half-space. The transmitted rays also belong to the incident plane, where their direction is related to the angle of incidence through the well-known Snell law of refraction and can be described by proper refraction (transmission) coefficients (indicated with T in Eq.3.5) given by the well-known Fresnel equations, as well, Balanis [60]. It is worth reminding again that Fresnel coefficients need the knowledge of (ϵ) of the surface / object under examination.

Transmission through a single, planar boundary between lossless materials can be computed through the Snell refraction coefficients, according to the power conservation law, as it follows:

$$T_{\text{TE/TM}} = 1 + \Gamma_{\text{TE/TM}}$$

Eq. 3.5

In case of lossy materials, part of the power can be dissipated inside the object under examination. Thus, Fresnel equations need to be extended considering also (σ) of the surface / object under examination, as shown by Balanis [60], Roy [61] and Burnside [62], adding complexity to the Reflection and Transmission models, as discussed in chapter (4).

Concerning Above 6GHz, the role of reflections (named also specular multipath components (SMC)) is usually dominant in the multipath with respect to other propagation mechanisms in terms of power, as described in chapter (5). On the contrary, the impact of transmission/refraction mechanism only is less significant at cm/mmWaves due to the greater losses of penetration/attenuation, as described in chapter (4). For example, a human body at 100MHz can be approximately considered transparent, whereas at 60GHz it has a significant impact attenuating up to 40dB the transmitted power.

3.2.2 Diffraction

When a wave (ray) impinges on a surface with curvature smaller than or even similar to the wavelength, reflection/refraction no longer occur and diffraction is triggered, instead. This is the case of items with edges, wedges and holes, and it is important to remark that the nature of diffraction depends on the relationship between waves wavelength and the shape of the surface. First investigations on diffraction can be attributed to Fresnel, who exploited the 'secondary source principle' previously proposed by Huygens to model diffraction phenomena. Then Kirchhoff formalized the Fresnel empirical theory by means of the Maxwell equations. A geometrical theory (GTD) was later formulated by Keller, and then improved by Kouyoumjian and Pathak [63], gathering everything into the Uniform Theory of Diffraction (UTD), as described by Lubbers [64], [65], [66]. Differently from simple reflection and refraction, diffraction mechanism produces an infinite number of diffracted rays. According to GTD, in case of an edge the diffracted rays lay on the lateral surface of the so called Keller cone, as in Fig.3.7. The diffracted field value in a generic point in the space on the diffracted ray can be compute using diffraction coefficients defined within the UTD [63], as well as Fresnel coefficients for reflections and transmission.
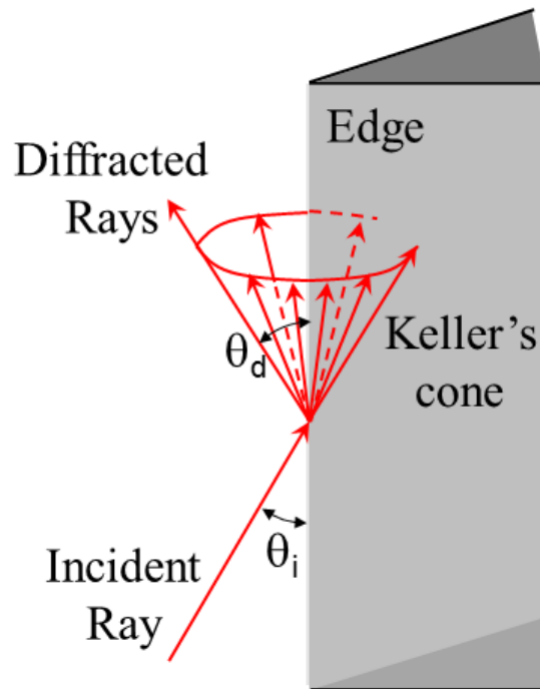
FIGURE 3.7: Diffracted rays according to Keller cone.

In real scenario diffraction Below-6GHz is a fundamental mechanism that helps out the waves to overcome obstacles, as hills or buildings. As depicted in Fig.3.8, when a link between a BS and mobile takes place in a street canyon, most of the power could come from Over-Roof-Top (ORT) propagation thanks to the diffraction phenomenon, because the LOS path and other Below-Roof-Top (BRT) paths are shadowed/blocked by buildings and crossroads, Bertoni [35]. Considering now Above-6GHz bands, due to the shorter wavelength, this advantage is not valid anymore and then diffraction becomes an unreliable and weak propagation mechanism, as shown in chapter (5). At cm/mmWaves just turning around a building corner at street level a 40dB drop both at 28GHz and 70GHz is experienced by the received signal strength level, as reported by Rappaport [15], for example.
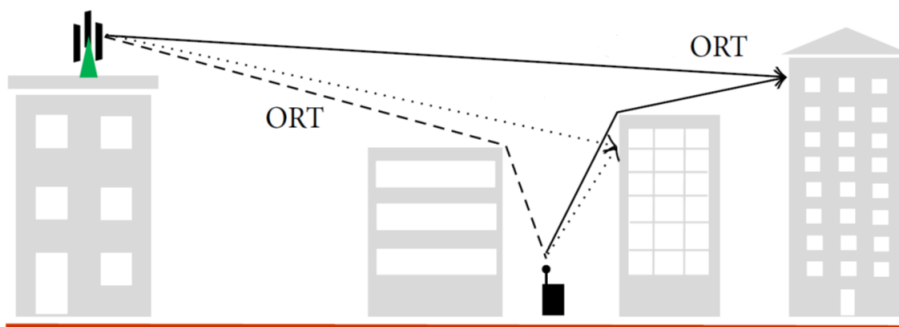
FIGURE 3.8: Example of Over-Roof-Top propagation in urban scenario.

3.2.3 Scattering

Nature of Diffuse Scattering

Besides Reflection, Transmission and Diffraction, an other mechanism is still missing, but rather important, overall for Above-6GHz: diffuse scattering (DS). For example, let's consider an external wall of an house: the outdoor surface is rough and in the inner part has tubes or even concrete reinforcement pillars. If an object is not flat and has no sharp edges, can anyway present rough and irregular surfaces in the real world, differently from computer-aided design (CAD) models. Moreover, considering the volume of the objects we can observe also inner irregularities as grids, pipes, panels or even different materials stacked together. All of these details cause different e.m. waves interactions with respect to "ideal" reflections, transmission or diffraction, which can be gathered into a the wide category of scattering. Differently from the well-known Radar-Cross-Section (RCS) used in radar field to estimate the overall scattering of targets like missiles or ships, adopting a ray-based approach is not straight-forward modelling the diffuse scattering, because DS is not a local mechanism (i.e. generated in a confined small region where the e.m. waves hit a given surface, as well as for Reflections), but rather a 'distributed' effect. Fig.3.9 shows indeed a qualitative microscopic view of scattered rays off a 2D random rough surface. A given RX could collect many of those rays which rise in a random distributed way from different sections (named dS in the following equations) of the whole surface. This results then in a superimposition of a large number of micro-contributions, i.e. with unknown, random phase value and polarization state, which are named commonly Dense Multipath Component (DMC), differently from SMC.
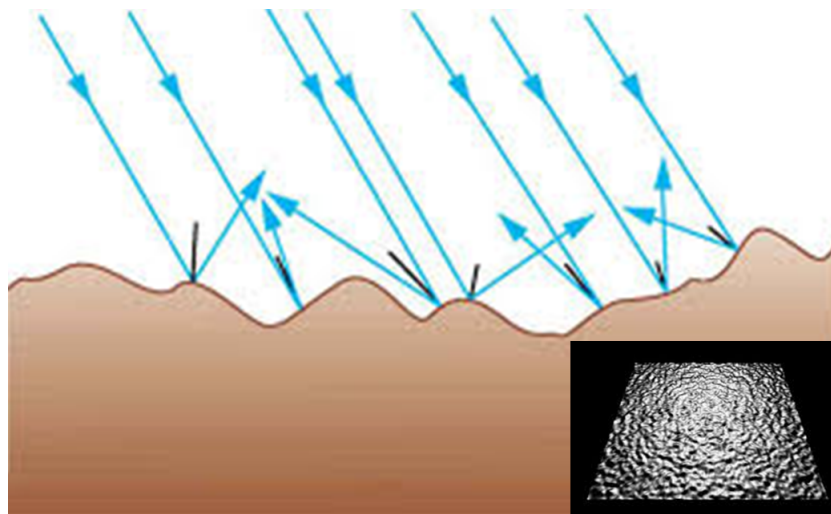
FIGURE 3.9: A qualitative representation of rays bouncing onto a rough scattering surface.

Let's think about cities digital map or CAD description of indoor places: we may lack of important items like trees, rooftops, poles, chairs, furnishings objects. It is by far remote the chance to have knowledge about the surfaces roughness or even the volumes irregularities. Thus, for any available database describing a given scenario there is a trade off between the cost and the reliability, limiting the applicability of any scattering model. At Below-6GHz frequencies, DS can be in fact attributed to the environmental clutter (e.g. the set of small items or building details) which is rarely taken into account in scenario representations, since both the urban furnishing

(outdoor) and the internal furniture (indoor) are often made of objects mainly acting as scatterers rather than reflectors, due to their size small or equal to the wavelength.

The extension of this analysis to the cm/mmWaves is still an open issue requiring further investigations, Pascual-Garcia [67]. On one hand, every material (including walls and floors) appears rougher as the frequency increases, but on the other hand, smaller penetration depths are experienced at higher frequencies. The former aspect might contribute to enhance the scattering due to surface irregularities, whereas the latter may lead to a reduction of the scattering effects related to volume unhomogeneities. Moreover, even small objects commonly not present in the input database may behave as specular reflector at cm/mmWaves due to the smaller wavelength and therefore could contribute also to SMC. Whether an increase or rather a reduction of DS is an issue hard to solve, especially because different results can be obtained at different frequencies or different scenarios. Preliminary results are provided in the next chapters (4) and (5).

Scattering modelling

Three main ways are available today in literature to model the diffuse scattering (Elfouhaily and Guerin [68] for more details): full-wave e.m. computational algorithms, Kirchhoff Approach (KA) and finally Effective Roughness (ER):

- Full-Wave approach: full-wave simulators are the most accurate solutions to model scattering once the exact details about the shape and the material of an object are known and digitally reproduced. With partial or no information about the object geometry it is impossible to use these algorithms by default. However, a big advantage of these algorithms is represented by the possibility to compute both near and far fields with no approximations.

- Kirchhoff Approach: as illustrated by Beckmann and Spizzichino [69], Harvey [70], Didascalou [71], Ding [72], Ouattara [73], the Kirchhoff Approach (KA) is a well-known method to model scattering of rough interface based on Helmoltz integral under some assumptions about the analyzed object. First of all, an estimate of the surface roughness must be available numerically. Usually a Gaussian distribution is assumed for walls. Secondly the surface should be "smoothly rough", without very sharp points or lines. The Kirchhoff approximation requires that the curvature radii of the surface must be large compared with the wavelength. However, as shown in Fig.3.10, approximating the surface locally with tangent planes it is possible to obtain the scattered field analytically in the far field. Many improved versions of this approach are known in literature as described by Ogilvy in [74] and offer good results within the region of validity of the assumptions, Jansen [75].
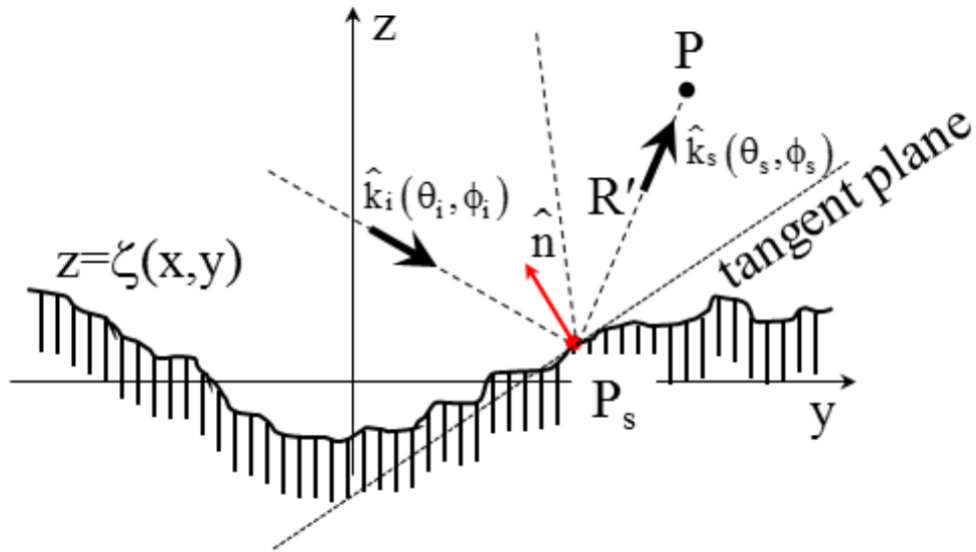
FIGURE 3.10: KA tangent plane computation. The $z = \zeta(x,y)$ is the 2D function describing the height of the surface.

- Effective Roughness approach: as illustrated by Degli-Esposti initially in [76],[77], then in [78],[79],[80],[81], and moreover in [82],[83], a valid alternative is represented by the Effective Roughness (ER) method, invented and developed at University of Bologna, by the research group I am belonging to. This physically-sound method is worldwide recognized as meaningful to model scattering, even though is not especially supported by strong theoretical groundings, but rather specifically conceived to be easily included into ray-tracing tools. ER approach aims at providing a scattering model based on a small set of parameters, which can be tuned with flexibility, as shown in chapter (4). As in Fig.3.11, ER model basically assumes that part of the power carried by a wavefront impinging on a surface is partly scattered in other directions rather than the specular direction at the expense of the reflected / transmitted power. As well as in reality, ER model unifies Reflection / Transmission and Scattering mechanisms, irrespective to the actual scattering causes, as surface or volume irregularities.

  In details, the overall amount of scattered power can be set through a proper scattering coefficients defined as S_R for backward space and S_T for forward space. The scattering parameter and the scattering pattern may be in general different in the backward half space and in the forward half space, especially for thick slabs due to inner composition. Regarding the scattering pattern, several studies have proved that a single-lobe (directive) pattern centered on the direction of the specular reflection / transmission is often the best representation, Mani [84] [85] , Fuschini [86] and Vitucci [87].
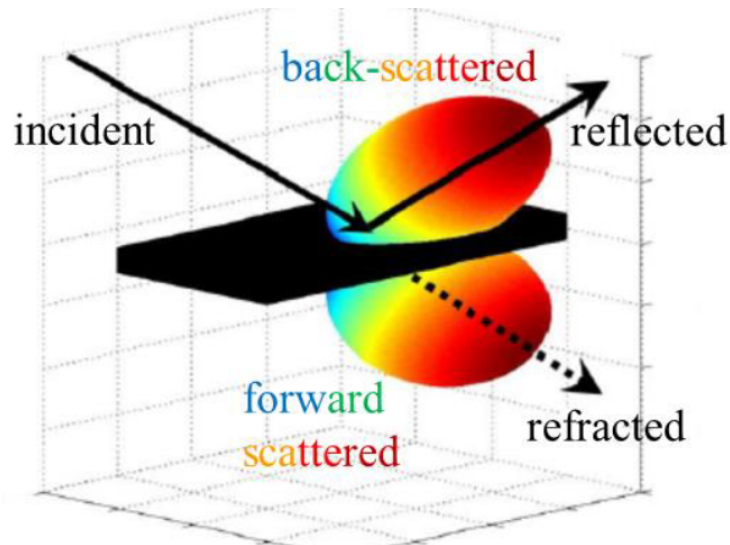
FIGURE 3.11: ER model scattering lobes in backward/forward half-spaces.
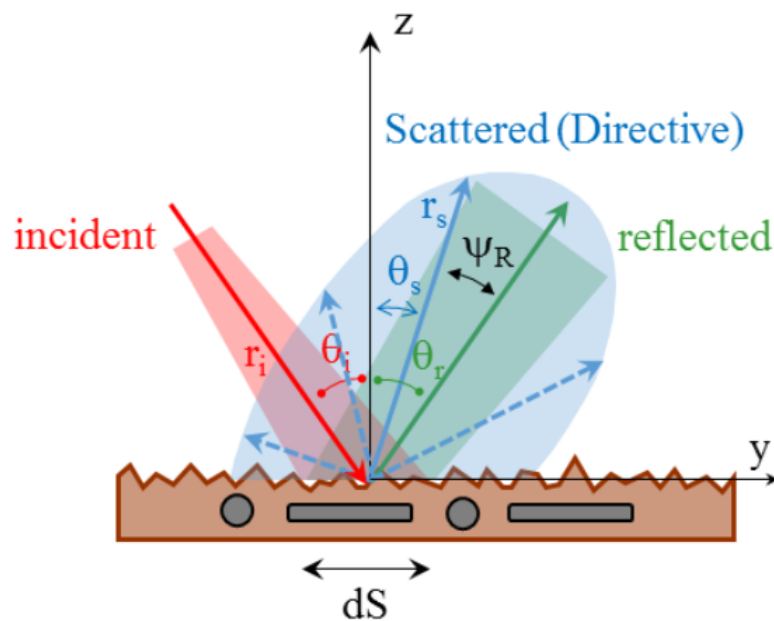
FIGURE 3.12: ER Scattering model with angles details.

In fact, in Fig.3.12, r_i and r_s are the lengths of the incident and of the scattered rays respectively, θ_i and θ_r are the angle of incidence and of reflection and, then, ψ_R is the angle between the direction of the reflected wave and the scattering direction (i.e. θ_s).

The power density (indicated with p in terms of W/m^2) of DS contributions are proportional to the scattering coefficients S_R and S_T, related to the overall amount of diffused power, as shown in Eq.3.6. Since DS occurs at the expenses of specular reflection and transmission, a proper reduction factor must be applied to reduce reflection/transmission coefficients, in order to preserve the overall power balance, [79].

$$
\begin{cases}
p(\psi_R) \propto S_R^2 \left(\dfrac{1 + \cos\psi_R}{2} \right)^{\alpha_R} \\[4mm]
p(\psi_T) \propto S_T^2 \left(\dfrac{1 + \cos\psi_T}{2} \right)^{\alpha_T}
\end{cases}
$$

Eq. 3.6

For sake of completeness, the power density of the scattered field in the backward half-space along θ_s is reported in equation 3.7, where the exponent α_R is the parameter related to the width of the scattering lobe, Γ is the Fresnel reflection coefficient at the surface interface and S is simply the S_R parameter. See Degli-Esposti [78], [76],[77], for further details.

$$
\left| \vec{S}_s\left(r_s, \theta_s\right) \right| = \frac{\left| \vec{E}_s\left(r_s, \theta_s\right) \right|^2}{2\eta} = \left(\sqrt{60 \cdot G_{Tx} \cdot P_{Tx}} \cdot \Gamma \cdot \frac{S}{r_i \cdot r_s} \right)^2 \cdot \frac{\cos(\theta_i)}{F_{\alpha_R}} \cdot \left(\frac{1 + \cos\psi_R}{2} \right)^{\alpha_R} dS
$$

Eq. 3.7

Recapping, all the ER model parameters are listed in Table 3.1 in the following:

TABLE 3.1: Effective Roughness parameters.

Symbol	Explanation
S_R	coefficient related to the percentage of scattering power in the backward space
α_R	coefficient related to the beam-width of scattering lobe in the backward space
S_T	coefficient related to the percentage of scattering power in the forward space
α_T	coefficient related to the beam-width of scattering lobe in the forward space
$\kappa_x pol$	coefficient related to the polarization decoupling of scattering power

According to some experimental investigations at Below-6GHz, S_R can range between 0.2 and 0.4 in rural and sub-urban environments, while values up to 0.6 have been achieved in scenarios with complex building structures. Typical values for α_R range between 2 and 4, corresponding to overall satisfactory prediction accuracy with respect to narrowband and wideband comparison with measured data. An assessment at 70 GHz in chapter (4) shows that backscattering from a brick wall seems slightly richer at mmWaves than Below-6GHz, with an upper bound for α_R values that can increase up to 6. Finally, an additional parameter ($\kappa_x pol$) has been included in the ER model in order to approximately take into account the depolarizing effect due to the unknown causes of DS. Its value basically sets the amount of power transferred into the orthogonal polarization state (see Eq.3.4) after a scattering interaction, Degli-Esposti [88]: $\kappa_x pol = 0$ means that polarization is perfectly preserved, $\kappa_x pol = 0.5$ that the power is equally split between the co-polar and cross-polar components, and $\kappa_x pol = 1$ that the power would be totally transferred to the cross-polar

component. Generally, $\kappa_x pol$ usually ranges between 0.0 and 0.2 in outdoor environment. On the contrary, $\kappa_x pol$ values up to 0.5 are achieved in typical office and laboratory environments. Novel values of $\kappa_x pol$ for cm / mmWaves can be found in chapter (4).

3.3 Ray Tracing

Ray Tracing/Launching (RT/RL) are advanced software which belong to the category of ray-based deterministic models, which rely on ray approximation and on GTP to represent the propagating field as a set of rays, implementing all the propagation mechanisms seen before in order to model the radio channel in a digitized scenario. RT models were initially applied to optical propagation problems and only in the early '90 applied to RF for field prediction in urban environments, especially for coverage purposes. Today RT represents much more than a good solution to provide accurate, site-specific field prediction and multidimensional characterization of the radio propagation channel in the time and space domains, as shown by Degli-Esposti [79], Vitucci [87] [89] and Fuschini [41].

3.3.1 Inputs

The inputs of RT are the most important information upon which the final radio channel prediction results rely, because the possible RT outcome flaws may derive from missing and/or erroneous input data, rather than errors in the physical propagation "engine", based on GPT. Then it is worth focusing attention on the sensitivity to inputs for the scenario description, as shown by Nix [90] for Below-6GHz in urban scenario.

As input, a digital description of the environment refers to both its geometrical and electromagnetic properties, named uniquely as RT database. The geometrical description concerns the shape, the dimension and the position of each object inside the environment. These data are often stored into a proper digital environment database in 'vectorial' or 'raster' files which feed the model as input file, as sketched in Fig.3.13 (2D top view)) and 3.14 (3D side view). In these raw figures, it is possible to observe the details of the digital RT database of a small office, as explained in chapters (5) and (7). An example of double-bounce reflection ray (e.g. second order reflection) is plotted from TX2 to RX4, for example.
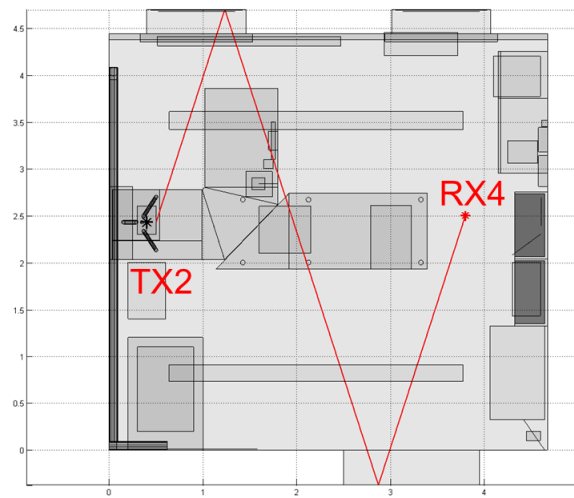
FIGURE 3.13: The 3D small office RT description: top view.
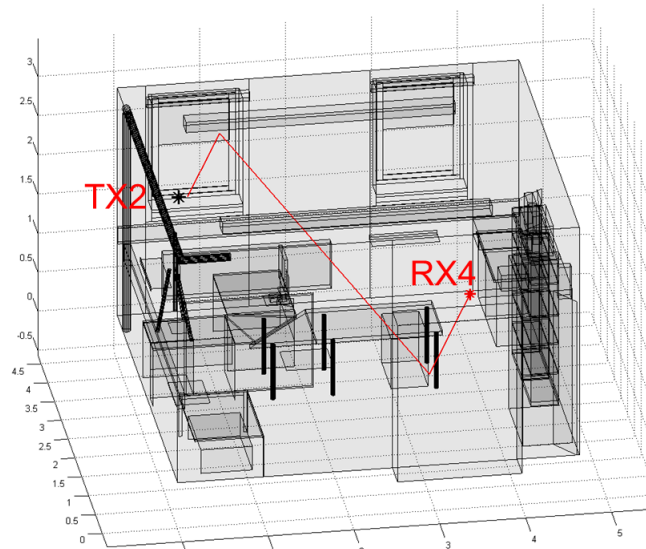
FIGURE 3.14: The 3D small office RT description: side view.

Secondly, the electromagnetic description of the environment requires to associate each object to the proper values of complex electric permittivity, so that its electromagnetic behavior can be computed. A full description can be found in chapter (4).

An other input for RT are the antennas which play a significant role Above-6GHz, as stated before. As documented by Gil [91] or Petrita[92], starting from 2D antennas description (e.g. datasheets usually include E-plane and H-plane radiation patterns), it is easy to create 3D pattern thanks to interpolation, and then feed the information to the RT. Unfortunately, the reconstructed 3D pattern in the volume external to the main beam may lack of accuracy, neglecting the presence of secondary lobes and/or mistaken the gain or polarization. This aspect is overall important for interference evaluation, as discussed in chapter (7).

Finally, in RT algorithms the positions of both the source (TX) and the destination (RX) need to be specified from the beginning of each prediction step. Also this point could represent a source of error, comparing RT results with on-field measurements, especially with moving terminals.

3.3.2 RT Engine

Given a TX-RX pair the main problem of RT algorithm is how to find all possible trajectories of rays undergoing up to a maximum number of bounces, which are compliant with GTP geometric rules and therefore are expected to correspond to existing propagating paths. Efficient algorithms must be adopted because the ray-search task is computationally very intensive and the number of rays to be found can be in the order of millions. The visibility concept and the corresponding visibility tree are usually adopted.

As a first step, the environment is decomposed into a set of objects such as polygonal walls, straight edges, or parts of them. Rays are assumed to propagate along straight lines in free space and to bounce on objects according to reflection, diffraction or scattering interactions. If objects are assumed penetrable rays can also propagate through them. Visibility is the potential existence of an unobstructed radio propagation path between two objects according to a given kind of interaction, as in Fig.3.15.
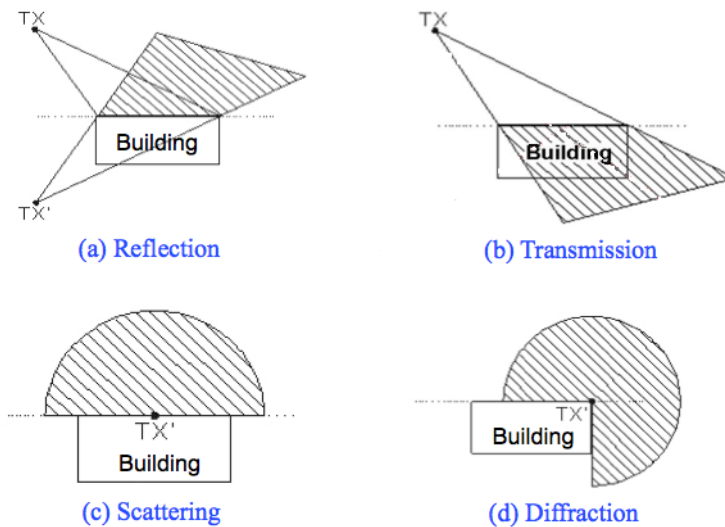
FIGURE 3.15: Visibility regions for different cases.

The RT algorithm arranges all the objects in a database containing all the visibility relationships among them, usually known as "visibility tree". Starting from the root of the tree, corresponding to the transmitter (TX), the visibility tree is built according to a recursive procedure: the first layer contains all the objects (or part of them) that can be seen directly from the TX and, in general, the n-th layer contains the objects that can be seen from those belonging to the (n-1)-th layer. In particular, objects are stored in the tree by means of proper "virtual transmitter" (VTx) (see Fig.3.15(a)). For example, the first-order reflection VTx is defined as the symmetric point (image) of the real TX with respect to the surface plane, according to the image ray tracing approach, Bertoni [35]. The visibility can be performed practically through the Binary Space Partitioning (BSP) algorithm, Glassner [93].

The next step is the selection of the rays that satisfy the requirements and the exact determination of the interaction points, meaning that the visibility tree must be climbed up in order to determine the exact interactions points, in a so-called backtracking procedure, assessing the real rays trajectories.

3.3.3   DS model implementation

Moving on, it is noticeable to remark that the embedding of Diffuse Scattering (in particular ER model) into ray-based model as RT is a sensitive task requiring additional algorithms to manage the radically different nature of DS mechanisms with respect to Reflection, Transmission and Diffraction. Thus, DS can strongly increase the actual computation time of simulations. However, several studies, Mani, [85], [86], highlighted that wideband multidimensional prediction capability of deterministic channel models can be improved using properly tuned DS models. With reference to the RT model used in this work, a Ray Launching (RL) approach is used to implement DS indeed, based on rays launched from the transmitter with a discrete angle step. Each ray is representative of a ray tube of given angular aperture, and thus, the field is assumed constant over the cross section of the ray tube (see Fig. 3.2). Therefore, an angular/spatial discretization is assumed, which limits prediction accuracy. As compensation, ray launching is more CPU-time efficient than image-RT algorithms for prediction over vast areas or volumes.

The adopted ER model requires the proper subdivision of each surface element in smaller "tiles". Several rays are launched from each TX/RX according to a preset angular discretization, and the scattering tiles are then identified as the intersection between the launched beams and the objects inside the scenario. The area of each tile is related to the angular discretization and to the distance from the ray source. A new VTx is then placed at the center of each scattering tile, and the visibility process is then repeated as if it were a new real transmitter.

With the rapid development of graphics hardware in the recent years, new solutions have been proposed to exploit the high computing power and large memory bandwidth of GP-GPU, as the Compute Unified Device Architecture (CUDA) by NVIDIA®, widely derived from the computer graphics field, where ray tracing is differently used for rendering of images/videos for games. Due to the massive parallelization capabilities of GP-GPU, considerable reduction in computation time of ray tracing/ray launching simulations can be obtained especially when the GPU-based implementation is combined with efficient shouting and bouncing ray algorithms like BSP or kd-tree, Petrin [94]: speedups of 2.5X for over-rooftop predictions and up to 160X for predictions in urban street canyons are reported, with respect to simulations carried out with a standard ray launching algorithm. In full-3-D ray/tube tracing simulations, average reduction factors of 30 times in computation time can be obtained, as reported by Yubo [95].

3.3.4   Field Computation

Finally, the e.m. received field is built up summing properly, in terms of amplitude and phase, the contributes of all the computed rays, according to the RT setting used. The e.m. field of the k-th ray is outlined in Eq.3.8 below, where: N_b^k is the number of bounces experienced by the k-th ray, $s_\ell{}^k$ is the length of the ℓ-th segment composing the k-ray, s^k is the total unfolded length of the k-ray, D_ℓ is the appropriate dyadic to decompose the field into the two orthogonal polarization (e.g. TE and TM) at the ℓ-th interaction point including the interactions coefficients (Eq.3.4), SF_k is the

overall spreading factor experienced by the k-th ray (Eq.3.2), N_R is total number of received rays, $E_{T0}{}^k$ is the field at a reference distance of 1m from the TX in the direction of departure of the k-th ray, the pair $(\theta^k{}_T, \phi^k{}_T)$ are the departure angles of the considered k-th ray in the TX-based local coordinate system and e^{-js^k} is the phase factor. See Balanis [60], [51] for further details.

$$\vec{E}_R^k = SF_k\left(s_\ell, \ell = 0,1,2,...,N_b^k\right) \cdot \left(\prod_{\ell=\min\{1,N_b^k\}}^{N_b^k} \underline{D}_\ell \right) \vec{E}_{T0}^k\left(\theta_T^k, \phi_T^k\right) \cdot e^{-js^k}$$

Eq. 3.8

If the signal at RX side is required at the antenna port, then it is necessary to take into account its pattern and polarization. Then the current phasor I_R^k induced at the RX antenna port by the k-th ray can be computed as in Eq.3.9, where: $Y_{AR} = 1/Z_{AS}$ is the admittance of the receiving antenna, the pair (θ_R^k, ϕ_R^k) are the arrival angles of the considered k-th ray in the RX-based local coordinate system, p_R is the polarization vector, E_R^k is the received field and g_R is the RX antenna gain function.

$$I_R^k = -j\lambda \cdot \sqrt{\frac{\Re\left(Y_{AR}\right) \cdot g_R\left(\theta_R^k, \phi_R^k\right)}{\pi\eta}} \cdot \left\{ p_R\left(\theta_R^k, \phi_R^k\right) \cdot \vec{E}_R^k \right\}$$

Eq. 3.9

3.3.5 Outputs

Besides predicting radio coverage, RT is naturally valuable to evaluate the multipath propagation providing all possible multidimensional results: time, angle and frequency dispersion, Angle of Departure (AOD) and Arrival (AOA), cross and co-polarization decoupling, MIMO coefficients, paths trajectories and so on. One of the important advantage of RT is that the e.m. fields is modeled as a set of rays (which have a null transverse spatial dimension) at a single frequency, and therefore RT can potentially provide outputs with a "zero-spatio-temporal" resolution, easily comparable with any kind of measurements, using proper post-processing. Moreover, compared to SCM models used for Monte Carlo NLS simulations with nodes/users dropping, RT preserves naturally the spatial consistency of results thanks to GPT, leading to meaningful outcomes regardless of the location of the RXs.

3.4 Ray Tracing Above-6GHz Summary

Let's summarize the pros of RT for the radio channel characterization and investigation Above-6GHz:

- frequency-agility: considering the whole frequencies from 500MHz to 100GHz, the RT is a valid channel model candidate for channel modeling both Below- and Above-6GHz because it is more flexible than others models based on measurements.

- scenario-independent: RT is a radio channel model independent from the kind and the size of scenario because based on the e.m. theory (e.g. GTP / UTD) which is valid everywhere. Nevertheless the only limits are set by the inputs availability, as database or antenna information.

- spatial analysis predisposition: RT is naturally suitable to evaluate the spatial characteristics of radio channel, especially to assess BF and MIMO, thanks to ray concept.

- results accuracy and speed: considering future wireless systems Above-6GHz with short-medium range links (i.e. scenario have a limited size) and also the wide availability of high-speed computers with GP-GPU (e.g. NVIDIA®CUDA), RT has become today an efficient and fast tool, providing accurate results in a short time, as well as other popular models.

Chapter 4

Item-Level Characterization Above-6GHz

Since the radio multipath is caused by the different interactions between the matter (environment) and the e.m. fields (which carry the information), it is actually essential to characterize the e.m. properties of the materials which objects and items are made of. The data available for e.m. parameters in literature concerns mainly Below-6GHz bands limiting the applications of deterministic channel models as RT Above-6GHz, consequently. Using fundamental e.m. parameters as electric permittivity ($\epsilon = \epsilon_R \epsilon_0$ where $\epsilon_R = \epsilon'$ and $\epsilon_0 = 8.85 * 10^{12} F/m$), magnetic permeability (μ) and electric conductivity (σ) it is possible to model the interactions of e.m. waves (Balanis [60]). Considering the smaller wavelength Above-6GHz, in the following are presented two new experimental methods to characterize electromagnetically indoor objects and pieces of furnishing. With this "item-level" perspective we are able to essentially to provide valid input data to ray-based tools, at cm/mmWaves, and then, to obtain reliable radio channel predictions, as outlined in chapter (5) ,where an entire office is considered as testing scenario.

4.1 A Method for the Electromagnetic Characterization of Construction Materials Based on Fabry-Perot Resonance

4.1.1 Introduction

Several methods for measuring the complex permittivity of materials have been developed over the years, Salous [96], Afsar [97], Venkatesh [98]. Each method being suitable for specific frequency ranges, material types and applications. The most popular methods can be classified into four groups, (see Agilent [99] and Rhode-andSchwarz [100], for further details):

- 1) Transmission/reflection line methods [101];

- 2) Open ended coaxial probe methods[102];

- 3) Resonant methods [103];

- 4) Free space methods [104], [105], [106], [107], [108], [109], [110];

It is worth noting that construction materials are often coarse compound materials (e.g. concrete, asphalt, bricks, etc.) heavily exposed to humidity and temperature changes, showing large variability between different samples, so that an accurate characterization is hardly possible. Also simplicity and speed of execution are important features for a good characterization method of construction materials. For

these reasons free space methods 4) are the most commonly used methods at radio frequencies. Such methods allow the estimation of average or effective electromagnetic parameters of compound materials, which would be difficult or impossible to measure using smaller-scale methods. Potential problems are the presence of unwanted multipath propagation and the need for complex calibration procedures, since the absolute value of the complex reflection and transmission coefficients is commonly measured. Moreover, conventional free-space material characterization approaches usually need multiple measurements for different incidence/reception angles and the use of complex maximum-likelihood parameter determination (optimization) methods.

Since most construction materials are available into slab form (e.g. walls, plasterboard, wooden boards, glass, etc.) a measurement technique ([111]) is proposed on the basis of the Fabry-Perot resonance of the material slab: a well known phenomenon that is particularly evident when a large enough bandwidth is considered. Instead of performing multiple measurements on a material sample for different incidence/reception angles, wide measurement bandwidth are exploited to extract the same information from the difference between adjacent resonance frequencies using a simple setup. Roughly, a bandwidth of 1 or 2GHz should be enough to highlight more than two resonance peaks and dips and to apply the method in most cases: over such a bandwidth the complex permittivity of construction materials at frequencies Above-6GHz is generally constant. Methods based on a similar background have been proposed in the literature to determine the dielectric constant of microcrystalline liquids and gases or other materials mainly used in optical and electronic devices, [112], [113], [114], [115]. However, such methods make use of mirrors to implement a Fabry-Perot resonator beforehand to determine material parameters from the changes in the resonance frequencies caused by the material insertion. This would be difficult to be implemented at radio frequencies over large-scale construction material samples. Therefore, the mirror-less resonance of the material slab itself is used herein instead. Unlike other free-space methods, the slab frequency response pattern is directly observed in this method, and therefore the need for calibration using reference material samples, i.e. metal plates, is eliminated. Moreover, the determination of the real part of the permittivity of low-loss materials is virtually decoupled from that of the imaginary part and therefore the parameter determination procedure is simpler. This is a big advantage.

4.1.2   The method based on Fabry-Perot Resonance

If a plane wave impinges on an infinite lossless dielectric slab a resonant phenomenon takes place due to the series of waves undergoing multiple reflections - and transmissions - within the slab (see Fig.4.1):

$E_{r,tot} = E_{r,1} + E_{r,2} + \ldots$

$E_{t,tot} = E_{t,1} + E_{t,2} + \ldots$
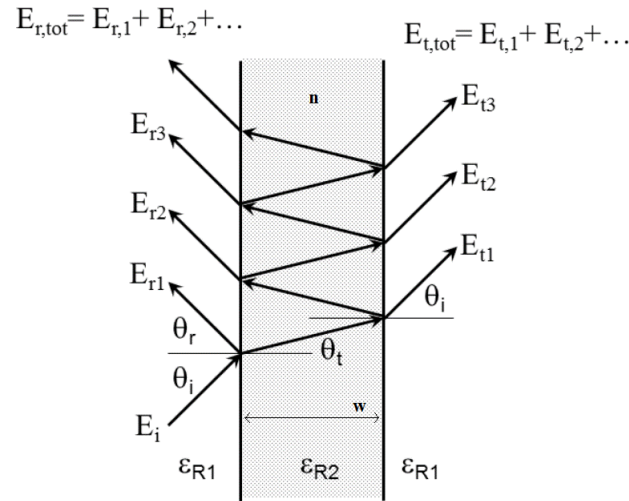
FIGURE 4.1: Graphical representation of the field "ping-pong" effect
inside a thick slab, due to multiple reflections and transmission of a
plane wave.

The effect can be formally described using the Fabry-Perot interferometer model: resonant conditions corresponding to minima of slab reflectivity and maxima of transmittivity, occur for:

$$\sin\left(\frac{\delta}{2}\right) = 0 \quad \Rightarrow \quad \delta = 2k\pi \qquad k = 0,1,2,\ldots$$

Eq. 4.1

where δ is the phase difference between each successive transmitted path at the medium-air interfaces, which is equal to:

$$\delta = k_0 \cdot \sqrt{\varepsilon_r} \cdot 2w \cdot \cos\theta_t$$

Eq. 4.2

where $k_0 = 2\pi / \lambda_0$ is free space wavenumber, and the rest of the right hand-side term is the excess optical path of each wave bounce, where ϵ_R is the relative dielectric permittivity of the medium, w is slab width and θ_t is the refraction angle (Snell law). Using the above equations, ϵ_R can be extracted as a function of the distance between two adjacent resonant frequencies Δf, as in Eq.4.3 (where c is the speed of light):

$$\varepsilon_r = \left(\frac{c}{\Delta f \cdot 2w}\right)^2 + \sin^2\theta_i$$

Eq. 4.3

Therefore by measuring the reflectivity of the slab for a given incidence angle θ_i over a wide enough bandwidth to show at least a couple of resonance notches (see Fig.4.2), the frequency-distance between two adjacent notches Δf can be derived and ϵ_R estimated through (Eq.4.3) with a single measurement shot. Of course Δf must

be small enough to assume ϵ_R constant over it, otherwise the average value of ϵ_R over the Δf window could be estimated. The slab thickness w must be large enough to keep Δf low given ϵ_R, as shown in (Eq.4.3). A thickness of a few centimeters is enough for most materials.

Formula (Eq.4.3) can be used also for low-loss materials, where $\epsilon_R = \epsilon' - j\epsilon''$ with $\epsilon' \gg \epsilon''$ (i.e. $\epsilon'' = \sigma / (2\pi f \epsilon_0)$) with σ the material conductivity [S/m]), which include the vast majority of building construction materials, approximately. To show this, the plane-wave series formula of a slab reflection coefficient, derived in Orfanidis [116], is used equivalently to Fabry-Perot model, but for lossy media. Such a formula is shown below for the case of normal incidence for simplicity:

$$\Gamma(f) = \frac{\Gamma_1\left(1 - e^{-2jk'w}\right)}{1 - \Gamma_1^2 e^{-2jk'w}} = \frac{\Gamma_1\left(1 - e^{-2\alpha'w}e^{-2j\beta'w}\right)}{1 - \Gamma_1^2 e^{-2\alpha'w}e^{-2j\beta'w}}$$

Eq. 4.4
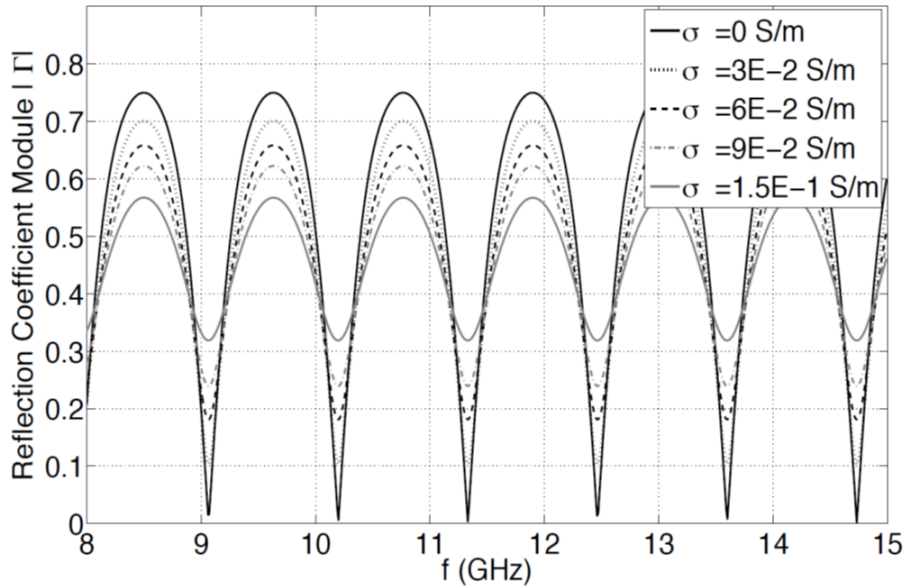
FIGURE 4.2: Reflection coefficient $|\Gamma(f)|$ module versus frequency, for different conductivity (σ) values., with $\theta_t = 0\,°$and $\epsilon' = 7$.

where Γ_1 is the Fresnel reflection coefficient at the air-medium interface and $\kappa' = \beta' - j\alpha'$ is the propagation constant of the slab material. By expanding the terms in (Eq.4.4) that depend on ϵ_R in a Taylor series under the low-loss assumption and truncating them at first order it is possible to show that the resonance frequencies of (Eq.4.4) do not change with respect to the lossless case. This is also shown in Fig.4.2 where $\Gamma(f)$ is plotted versus frequency for a material with $\epsilon' = 7$, for example: it is evident that the resonance dips do not appreciably change their position with the conductivity σ, even when σ is equal to 0.15 S/m, i.e. at the limit of the low-loss condition case.

Therefore, the parameters of low-loss materials can be determined as follows:

- a) ϵ' is estimated using (Eq.4.3);

- b) ϵ' is inserted into formula (Eq.4.4), or the equivalent formula for a generic incidence angle θ_i;

- c) ϵ'' (or σ) is determined by optimizing its value in (Eq.4.4) (or in the equivalent formula) for best match between the measured and computed $|\Gamma(f)|$ over the considered bandwidth.

Since the last step c) can be difficult due to peaky shape of $\Gamma(f)$ with narrow reflectivity dips, ϵ'' can be determined using instead the plane-wave series expression for the transmission coefficient, derived from the corresponding formula, under the assumption that the two media before and after the slab are the same:

$$\tau = \frac{\left(1 - \Gamma_1^2\right) e^{-jk'w}}{1 - \Gamma_1^2 e^{-2jk'w}}$$

Eq. 4.5

The transmission coefficient from (Eq4.5) is used for step c) in the following, indeed. Since reflection or transmission coefficients for inhomogeneous materials such as wood often do not show such a clean and regular trend versus frequency as shown in Fig.4.2, it is necessary to use caution when estimating Δf (step a)) or matching the measured and simulated coefficients (step c)). Spectral analysis using the Fast Fourier Transform (FFT) on the measured $\Gamma(f)$ can be used to estimate Δf, while careful visual matching or graphical curve fitting techniques such as least-squares methods can be used for step c).

4.1.3 Measurement Setup and Examples

Measurements have been performed in a common medium-size room using two vertically polarized, wideband horn antennas with a gain of 15 to 18dBi connected with an Anritsu 37397D Vector Network Analyzer (VNA). The bandwidth is 8GHz from 7.5GHz to 15.5GHz with a frequency step of 5MHz. All the set-up (e.g. VNA, cables and antennas) has been SOLT calibrated with Coaxial CalKit Maury 3.5mm 8050J. The antennas (Fig.4.3) have been positioned on their pedestal at a height of 20 cm over the measurement table and at a distance of 30cm from the Material Under Test (MUT) to ensure far field conditions. The antennas -6dB lobe footprints are always contained within the front surface of the different MUT.
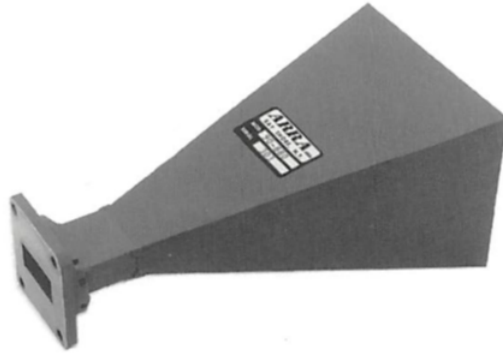
GENERAL SPECIFICATIONS

Frequency Range . . . . 2.6 - 40.0 GHz
Gain . . . . 15 - 18 dB min
VSWR . . . . 1.25 max
Material . . . . Aluminum
Output Connector :
    Series 860 . . . . .Type N Female Coax
    Series 862 . . . . .SMA Female Coax
    Series 880 . . . . .W/G Flange (Cover Std)*
Finish . . . . .Black paint per
                      MIL-L-81352

FIGURE 4.3: Measurement antennas specifications.
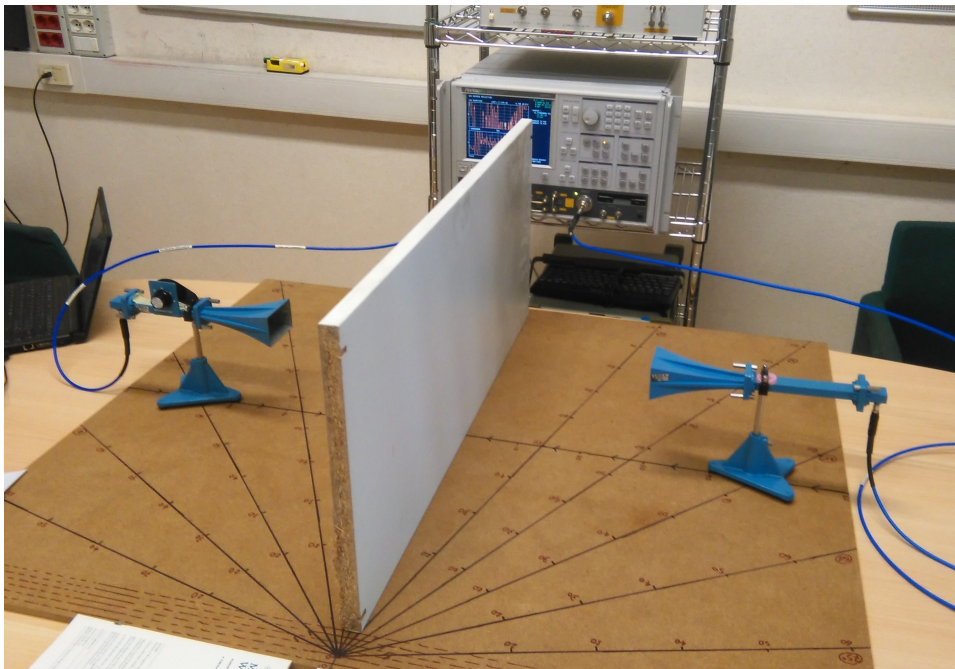
FIGURE 4.4: 0° Transmission upon the chipboard wood slab.
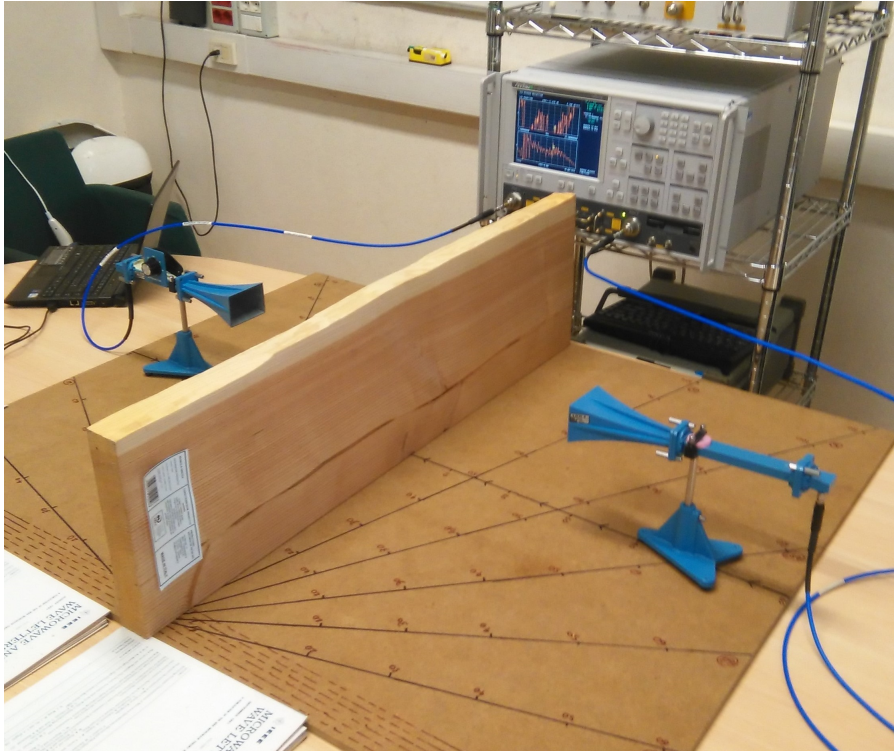
FIGURE 4.5: 0° Transmission upon the thick wood slab.
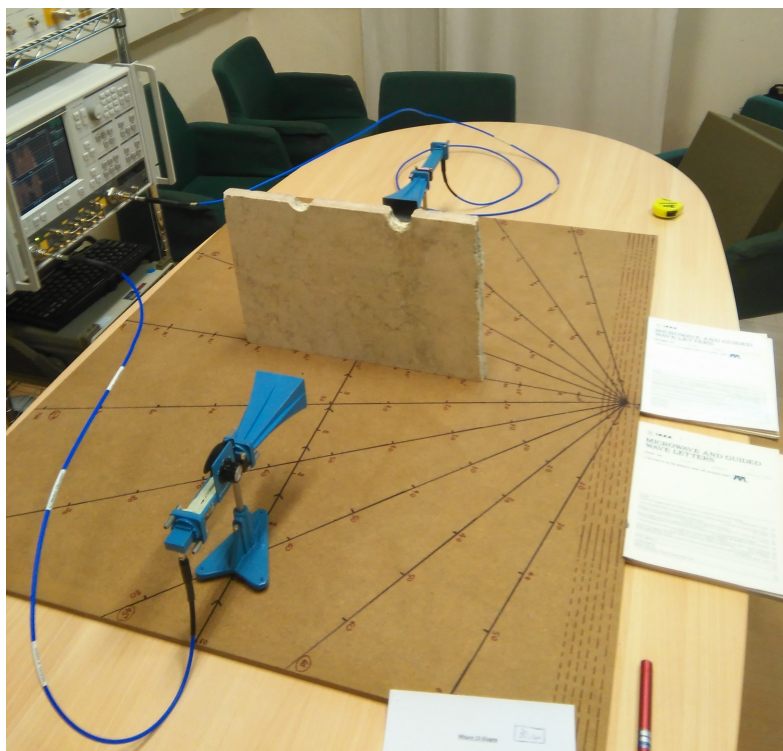
FIGURE 4.6: 0° Transmission upon the marble slab.
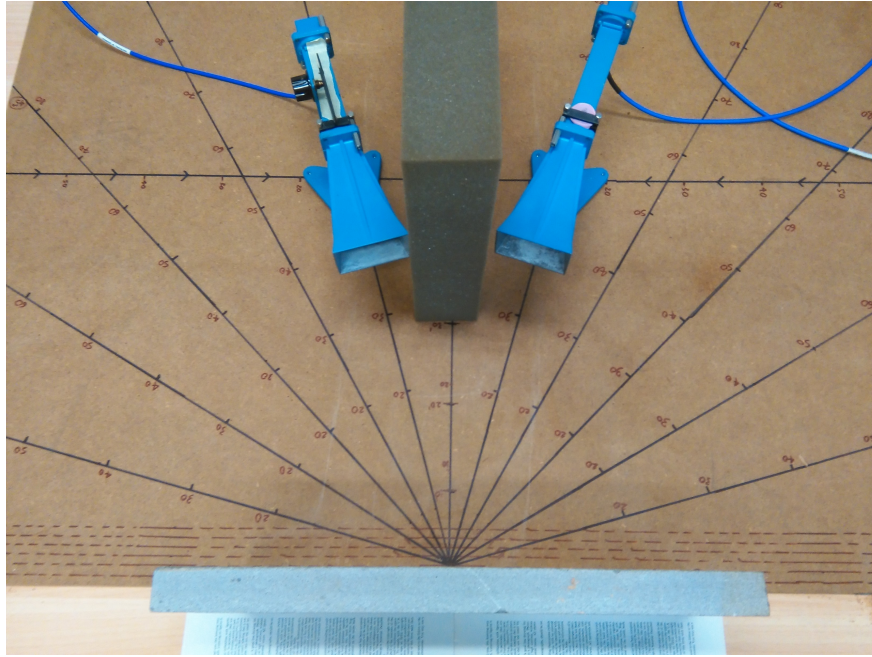
FIGURE 4.7: 15° Reflection upon the sandstone slab.
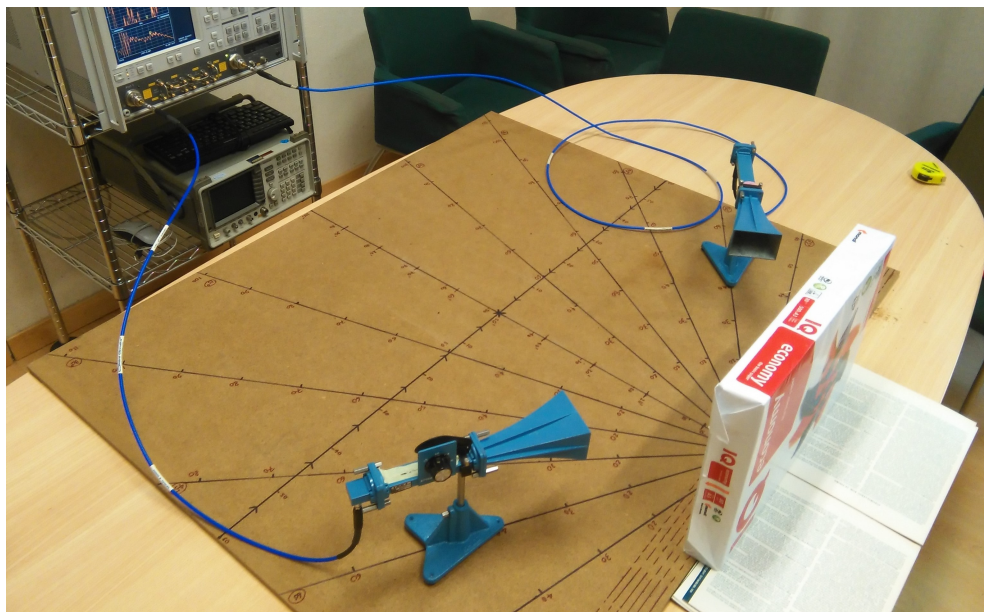
FIGURE 4.8: 60° Reflection upon the paper sheets block.

As in Fig.4.7, an absorber is used to block the direct path (cross-talk) between antennas during reflection measurements, which may corrupt results. Reflection measurements do not need to be calibrated because the goal is not to estimate the actual complex reflection coefficient, but only to extract the Δf of the slab resonance. Transmission measurements must be performed by comparing the frequency response with and without the MUT for the same setup. All measurements are performed easily in one single shot without the need of multiple measurements for different incidence/reception angles that would require rotating positioners. Of course room

reflections must be kept low enough to minimize their effects, i.e. spurious multi-path fading ripple, on the measurements. Measurements are reproducible with very small spread between different measurement sessions on the same sample.

Several MUT slabs have been tested: grey sandstone, yellow-Sahara marble, pine wood, paper stack, medium density chipboard. All slabs have smooth surfaces (at considered frequencies), a thickness from 2 to 4cm and dimensions of at least 60x40 cm, sufficient to minimize border effects. Measured and best-fit reflected/transmitted received powers (proportional to reflection and transmission coefficients modules) for the grey sandstone slab are shown in Fig.4.9. Antennas and noise have been carefully de-embedded from experimental data.
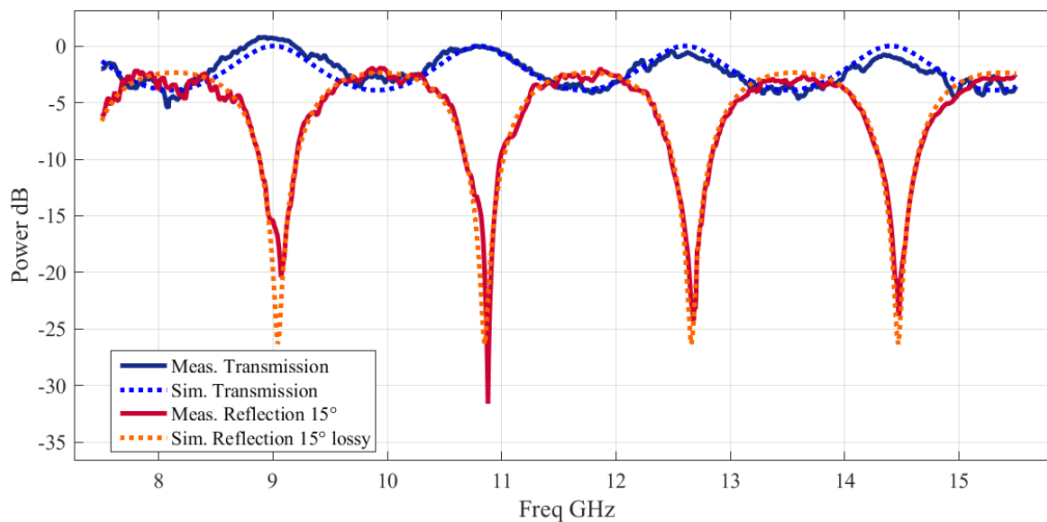
FIGURE 4.9: Perfect matching between measured and best-fit theoretical reflectivity (in red, with $\theta_i = 45°$) and trasmittivity (in blue) versus frequency for the grey sandstone slab.

Theory and measurements appear to agree very well. Resonant notches are very evident for $|\Gamma(f)|$ (see Eq.4.4), while the transmission coefficient is less bumpy. Other materials such as pine wood, probably due to the wood veins and nodes do not show a so regular behavior, but Δf extraction and transmission matching have still been possible.

While ϵ' is very stable over the considered bandwidth (Δf is constant over the whole bandwidth in Fig.4.9, ϵ'' is not as the measured transmittivity appears to be slowly decreasing with f. For this reason the bandwidth has been split in two and parameters estimation is performed separately for the two sub-bands, as shown in Table 4.1, where ϵ' and σ for different materials and for both sub-bands are reported. Results for $\theta_i = 15°$ and $\theta_i = 45°$ are almost the same (as they should) for all cases and therefore results are reported for both angles for sandstone, while only results for $\theta_i = 45°$ are shown otherwise.

M.U.T.	Refl. θ_i	7.5-11.5 GHz		11.5-15.5 GHz	
		ε_r	σ (S/m)	ε_r	σ(S/m)
Sandstone	15°	7.7	-	7.7	-
	45°	7.7	0.05	7.6	0.09
Marble	45°	6.9	0.15	6.9	0.15
Wood	45°	2.1 *(2.0)*	0.07 *(0.06)*	2.0 *(2.0)*	0.09 *(0.08)*
Chipboard	45°	2.6 *(2.58)*	0.11 *(0.13)*	2.6 *(2.58)*	0.15 *(0.16)*
Paper	45°	2.5	0.115	2.9	0.180

Table 4.1: estimated ϵ' and σ values. ITU-suggested values are reported in italic for reference.

Estimates derived using frequency-dependent formulas proposed by ITU [117], for the same materials and center-band frequencies are reported in Table 4.1 for reference: considering the great variability of construction material characteristics, even for the same kind of material, the agreement is surprisingly good. More generally, values reported in Table 4.1 are in good agreement with values reported in the literature for similar materials and frequencies (see Table 4.5 in the end of the chapter). Permittivity does not change between the two frequency bands considered, while conductivity appears to increase with frequency for all materials except for marble, in agreement with the frequency-dependent formula suggested by ITU.

4.2 Item level characterization of mm-wave indoor propagation

4.2.1 Introduction

The "item level" characterization is now extended to mmWaves ([118]) and to entire objects, including in the evaluation the scattering parameters (as touched upon in chapter (3)) in order to achieve a fine tuning of the indoor RT, also. In details, the e.m. scattering properties of several, different items (as listed in Table 4.2) have been investigated at 70GHz by means of measurements with Channel Sounder, in an anechoic chamber. The final goal is to assess whether and how such objects should be taken into account in the description of the propagating scenario in order to get reliable RT predictions at mmWaves (see chapter (5)). Moreover, the suitability of a single-lobe scattering model already adopted at lower frequency to describe also mm-Waves scattering patterns is assessed.

OUT	W × H × D (cm)	Short description
Brick wall	50 × 50 × 9	Made of hollow bricks and cement, with plaster on external surfaces
PC monitor	45 × 36.8 × 5.8	Squared monitor made of plastic, metal, and glass mix
Bookshelf	43.5 × 32 × 30	Box filled by hardcover books made of cardboard, paper, and small metallic rings
Music speaker	24 × 42 × 21.5	Wooden cabinet with inner speaker cone and ferromagnetic coil
Plant pot	27.3 Ø × 26	Ceramic circular empty pot
Wooden panel	56.5 × 30 × 1.3	Simple plain wood rectangle
Wooden cabinet	56.5 × 30 × 38.1	Heavy plywood locker
Absorber panel	61.5 × 61.5 × 11	Flat-sheet carbon loaded foam absorber

Table 4.2: Short description of the Object-Under-Test (OUT)

4.2.2 Experimental Setup and Measurement Description

In order to measure the scattering patterns of different common indoor items (see Table 4.2), an ad-hoc positioning arrangement has been developed and set up inside an anechoic chamber. Measurements have been conducted with a 70GHz dual-polarized ultra-wideband multichannel sounder (DP-UMCS), developed at TU Ilmenau, Mueller [119]. It consists of up/down-converters supported by an UWB CS based on a M-Sequence radar chip-set. A single clock generator (fc = 6.75GHz) was used, and the clock signal was distributed via cable to CS transmitter and receiver in order to minimize synchronization misalignment. The measurement system is sketched in Fig.4.10.
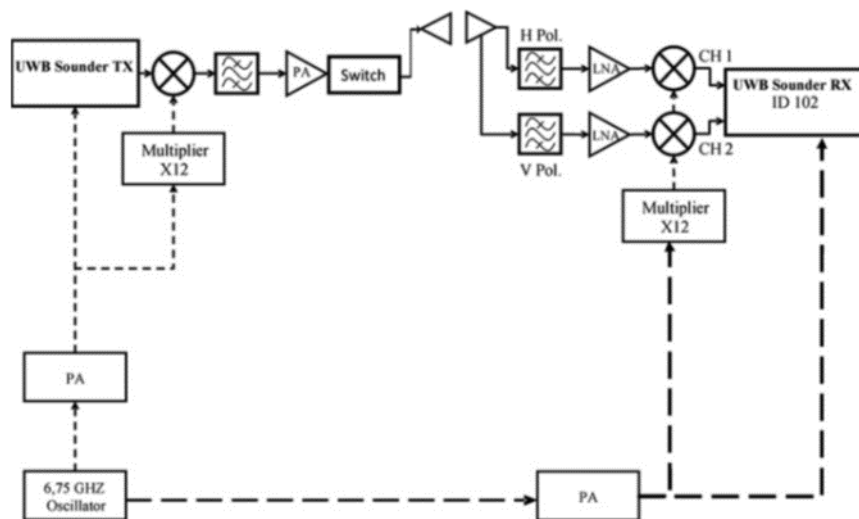
FIGURE 4.10: Channel Sounder schematic.

The baseband UWB stimulus signal is a periodic M-Sequence (spread spectrum signal), generated by 12-stage digital shift register. The impulse response duration is 606nsec and features a bandwidth of 6.75GHz. According to the sub-sampling frequency of fc/512, a scan rate of about 1600 complex impulse responses per second is achieved with a time resolution ~0.15 nsec. The frequency range covers the baseband (0 to 3.5GHz) and (3.5 to 10.5GHz). Up/down converters are used to reach the measurement band of 71-77GHz. A PA at the TX provides a 1-dB compression point of 30 dBm to overcome cables attenuation. In order to avoid saturation effects at the RX, the transmitting power was attenuated to nearly 0dBm. Low noise amplifiers (LNA) at the receiver stage feature a gain of 20dB. Conical horn antennas with approximately 20dBi gain and 15 °HPBW were used. Because the DP-UMCS RX

features two receiving channels, two orthogonal polarizations can be measured in parallel. Therefore, the system is capable to measure full polarimetric information.

Basically, each object under test (OUT in the following) was mounted on a rotating plate upon a solid positioner platform scanning all azimuthal angles with 5 step of resolution. The TX was located in a fixed position 2.2 meter apart from the OUT center, whereas the RX was attached at a distance of 0.4 meter on a metallic arm jointly united with the rotational block, thus keeping a constant orientation towards the OUT center, see Fig.4.11.
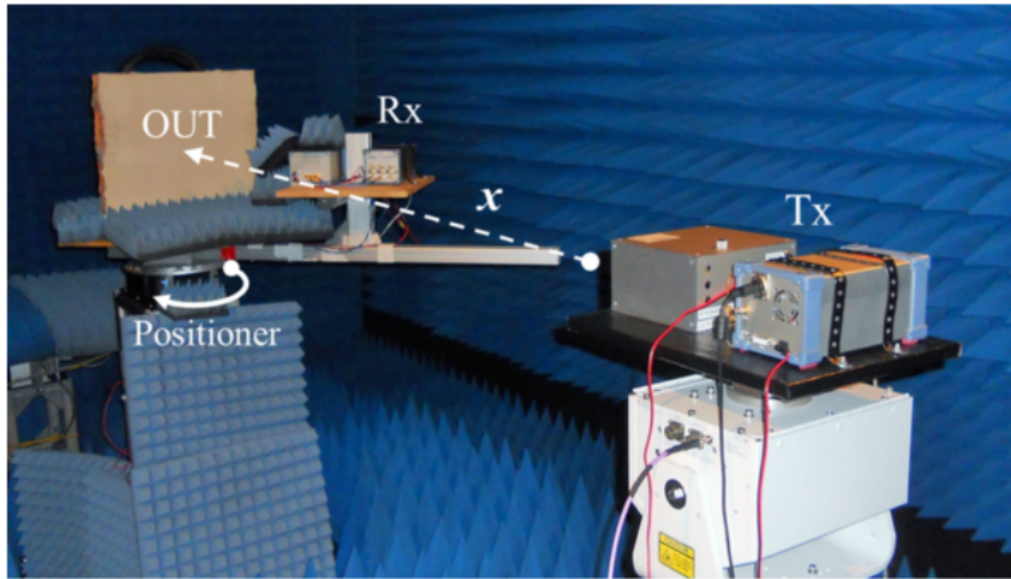
FIGURE 4.11: Experimental setup deployed in the anechoic chamber.

Both the metallic arm and the receiver module have been covered with absorbing panel, in order to shield as much as possible backscattering contributions not directly coming from the OUT. For each object, the measurements have been repeated with different tilt angles between the RX and the OUT (Fig.4.12), by manually turning the OUT of 0°, 30°, 45°, and 60°over the rotating table. According to the antenna HPBW value, the RX-OUT distance has been fixed in order to keep the main radiation footprint well included into the OUT surface, thus reducing possible border effects.
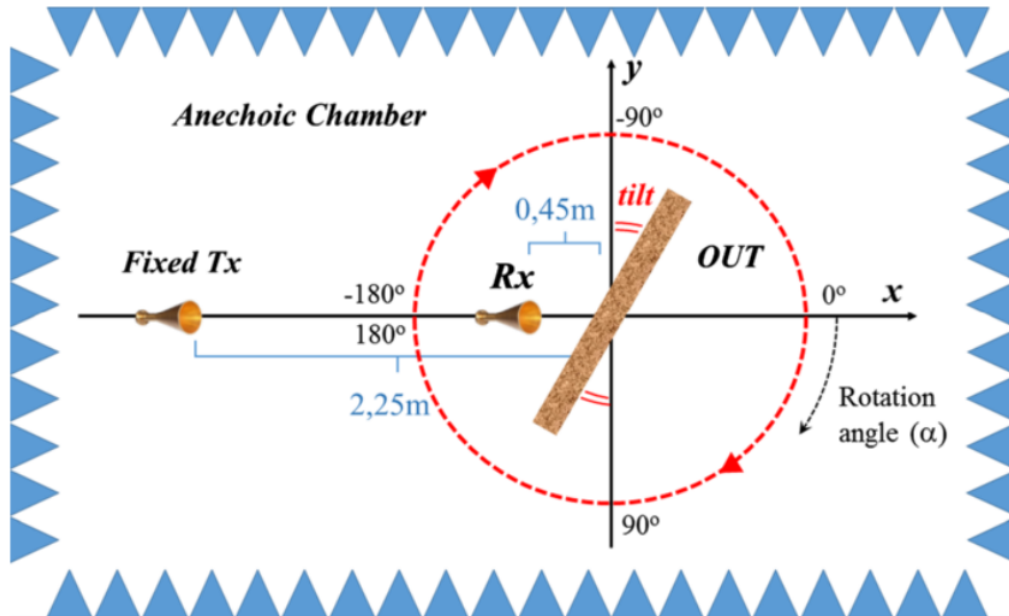
FIGURE 4.12: Explanation of the measurement rotational set-up.

4.2.3 Analysis of results

Table 4.2 describes the considered OUT in terms of geometrical dimensions and materials. The list includes a piece of brick wall as the fundamental item involved in almost all indoor and outdoor urban scenarios and a set of rather common objects, usually located in offices or residential places. The main properties of the electromagnetic scattering generated by the considered OUT when illuminated by a mmWaves radio signal are investigated in the following.

4.2.4 Analysis of measurement: Penetration Losses

A summary of the average measured penetration losses for the different objects is reported in Table 4.3.

OUT	Obstruction loss		XPD
	(dB)	(dB/cm)	(dB)
None (only antennas)	0	0	23
Brick wall	25.3	2.8	11.7
PC monitor	34.0	5.7	12.7
Bookshelf	30.0	1.0	7.5
Music speaker	18.2	0.85	9.4
Plant pot	16.0	/	10.6
Wooden panel	2.7	2.1	12.8
Wooden cabinet	35.3	0.9	10
Absorber panel	53.8	4.9	4.8

Table 4.3: measured obstruction loss and XPD values for different OUTs.

In agreement with literature, the results confirm that mmWaves undergo higher attenuation with respect to lower frequencies: the comparison between the values in Table 4.3 and the results shown in Pena [120] suggests that brick wall penetration loss may increase up to a factor 5 if the frequency is moved from 1 to 70GHz. The PC monitor, probably due to some inner metallic layers and/or components, produces the heaviest obstruction. However, almost all the OUT exhibit a specific attenuation at least equal to ~1 dB/cm.

4.2.5   Analysis of measurement: De-Polarization

In order to assess the item impact on signal polarization, the cross-polar discrimination (XPD) values have been extracted from the measured data and are reported in the last column of Table 4.3. The XPD is defined as the ratio between the received powers in co- and cross-polarized configurations, Degli-Esposti [88]. Without OUT, the XPD is solely determined by antenna cross-polarization isolation (XPI), that is often rather good within the antenna main radiation lobe (23dB), but it may strongly decrease outside. In order to avoid that the XPD evaluation is shadowed by the poor antenna XPI for some line of sight (LOS) RX locations, a proper time gating has been therefore applied to the impulsive responses to remove the LOS contribution from the co and cross-polarized received power values. The overall XPD has been evaluated for each item by averaging over all azimuth angles and over different OUT tilts.

The XPD for the brick wall is almost 11dB less than antenna discrimination level, meaning that the item presence introduces an evident de-polarization effect, increasing cross-pol components at RX side. This consideration can be extended to all the OUT, since XPD values are always much lower than the antenna XPI. It is worth noticing that the mean XPD values may provide an evaluation of the only overall depolarization effects due to the item presence, without any thorough insight into the corresponding physical reasons, which can be different for the different OUTs. This is for instance highlighted in Fig.4.13, where the XPD values are represented against the different antenna positions for the PC monitor and the wooden panel, assuming an OUT tilt equal to 45°.
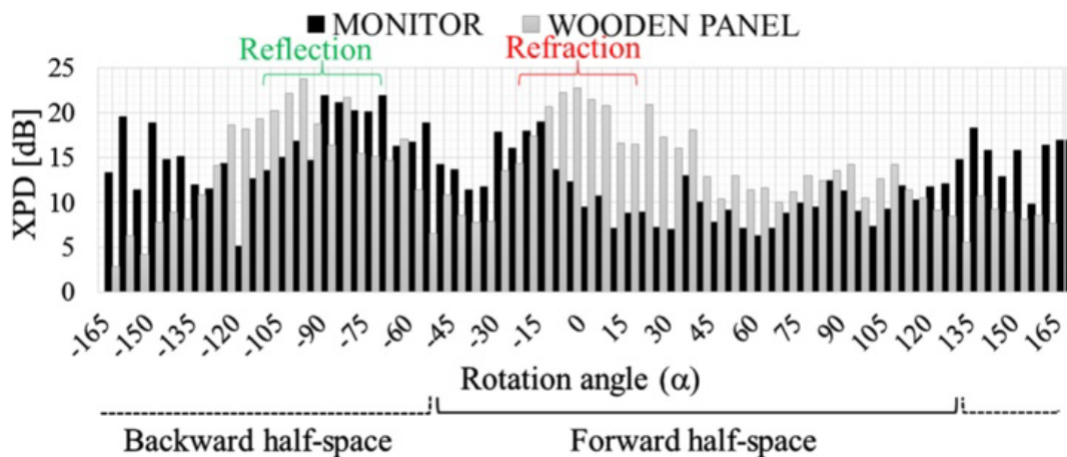
FIGURE 4.13: Cross-Polarization differences: monitor versus wooden panel with 45°of tilt angle.

The monitor XPD is clearly much lower over almost all the forward half-space (-45 °< α <135 °in Fig.4.13), where transmissions and forward scattering take place.

This might be due to the different inner composition of the two OUTs, and in particular, the electronic components inside the monitor with dimension comparable to the wavelength may produce some de-polarization effects much greater than those determined by the wood fibers of the panel.

The situation is basically reversed in the backward half-space ($\alpha > 135$ °and $\alpha < -45$ °in Fig.4.13), where reflection and backscattering occur; both the OUT have similar and quite high XPD (>15dB) around the directions of specular reflections (~-90 °), whereas far from it the wooden panel exhibits a much lower XPD with respect to the monitor. Apart from specular reflection, backscattering from the wooden panel is mainly caused by its surface roughness; due to its somehow random nature, some cross-polarization coupling can be expected. On the contrary, backscattering from the monitor seems weaker due to surface roughness (since the screen and the plastic on the rear side appear smoother than the wood surface) and rather determined by signal diffractions on several wedges present especially on the rear side. Since TX and RX are placed at the same height, the polarization can be expected unchanged after diffraction on the vertical edges, thus contributing to increase the XPD.

If the XPD values are now averaged over the whole angular range, the differences between the OUTs pointed out in the backward half-space are counterbalanced by those in the forward half-space and similar overall XPD are therefore achieved. As argued, this does not mean the PC monitor and the wooden panel affect the polarization of the propagating signal exactly in the same way. Differences between the tested items, not always fully characterized through the mean XPD values, are better highlighted in Fig.4.14, where the XPD cumulative distribution functions (CDF) are represented.
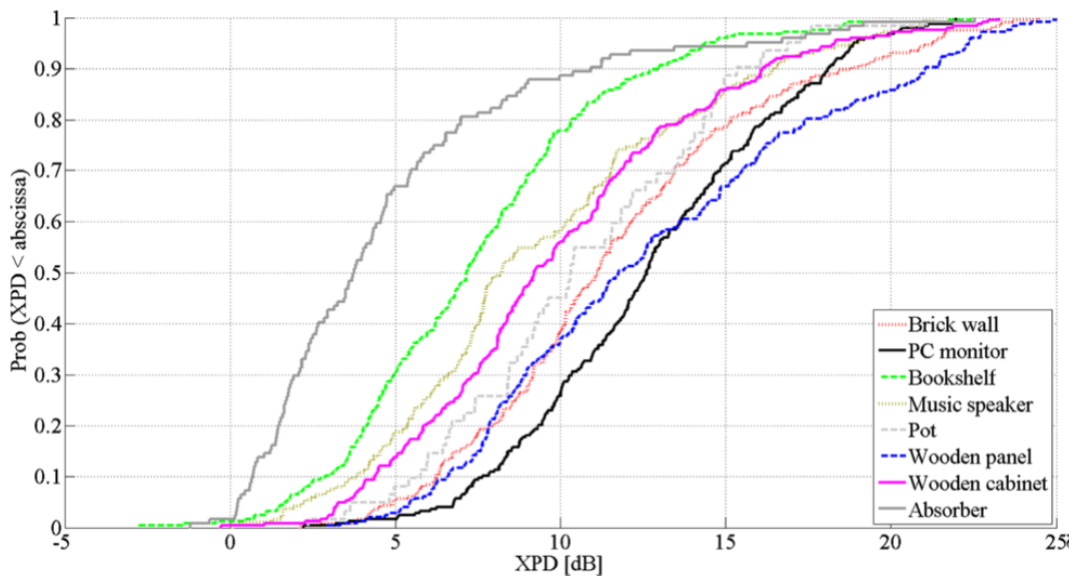
FIGURE 4.14: Comparison between XPD CDFs of the different items.

4.2.6 Analysis of measurement: 2D Scattering patterns

Moreover, the scattering patterns (similarly to RCS plots) have also been obtained for the different items from the measurement data, as shown in Fig.4.15 and Fig.4.16. LOS contributions have been again removed, in order to achieve a more reliable representation of the actual scattering patterns without the antennas influence. In

particular, the absolute received powers over the entire angular range [-180°, +175°] for the brick wall in different tilt angles configurations are shown in Fig.4.15: there are lobes around the reflection angles, around +120°for 30°tilt, +90°for 45°tilt, and +60°for 60°tilt, respectively.
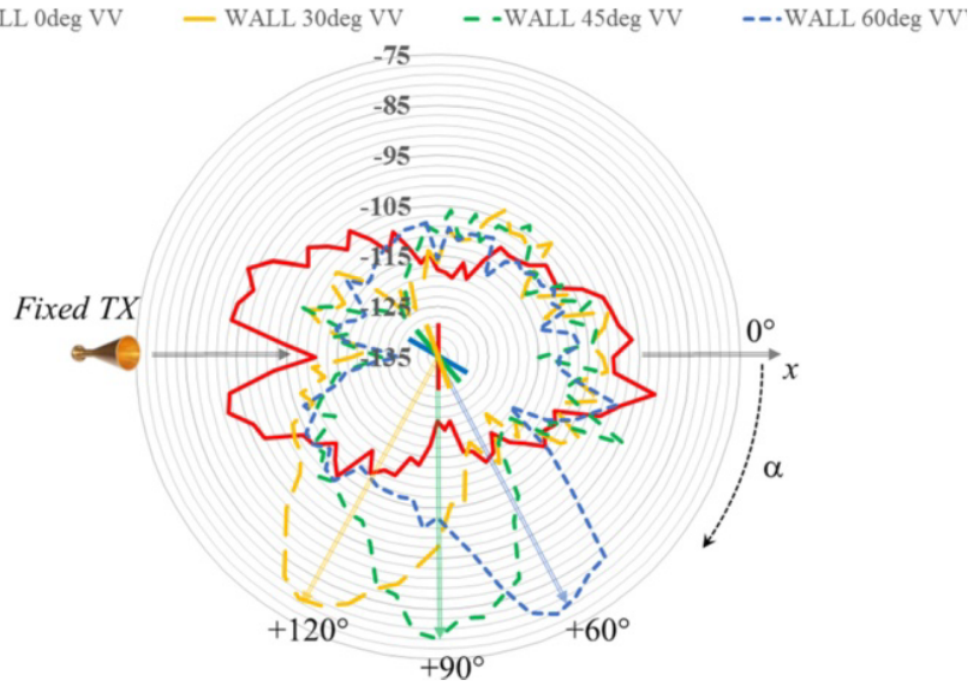
FIGURE 4.15: 360 °Wall scattering for different angles of tilt. Legend is on the top.

The main effect of backward diffuse scattering is seized in the angular width of the lobes, always equal nearly to 20°. Looking at the angles from 0°to 90°, evident transmissions lobes are clearly not present and forward scattering appears rather uniformly distributed in space. A possible explanation may refer to the volume unhomogeneities represented by the brick structure holes, which could contribute to scatter the energy as the radio wave penetrates the wall.

The scattering patterns of some OUT are compared in Fig.4.16.

It is evident that the wooden panel (green color in Fig.4.16) behaves rather differently from the other OUT, since it exhibits the narrower radiation lobe in the backward half-space and is the only item showing a clear scattering lobe also in the forward half-space. This seems rather consistent with its physical properties: despite a slight surface roughness and some inner unhomogeneities represented by the wood fibers, the wooden panel seems in fact the smoother and the more homogeneous among the considered OUT.
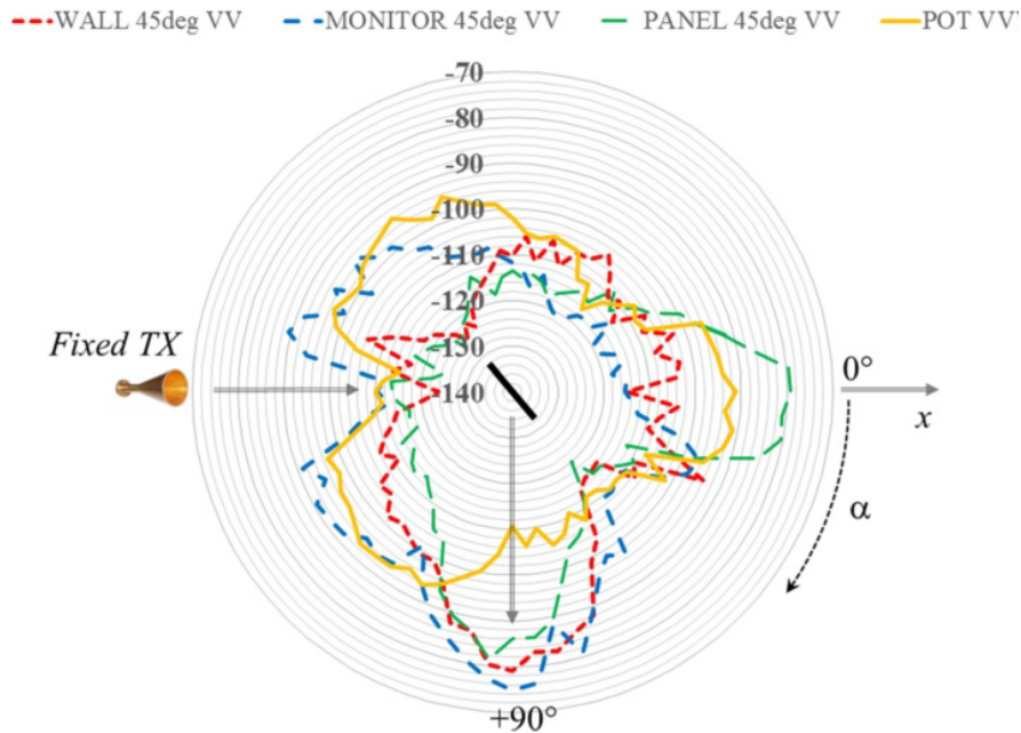
FIGURE 4.16: 360°scattering comparison among Wall, Monitor, Wooden Panel and Plant Pot with 45 °of tilt. Legend is on the top.

The monitor (blue color in Fig.4.16) shows an opposite behavior, with a radiated power rather widespread over the whole spatial domain. Of course, the overall amount of scattered power is much less in the forward half-space, due to the large obstruction loss. Such power spatial distribution is likely due to both the surface irregularities (especially on the rear side) and the internal volume unhomogeneities.

The brick wall (red color in Fig.4.16) behavior is in between the wooden panel and the monitor, may be more similar to the former in the backward half-space and on the contrary closer to the latter in the forward one. A widespread scattering pattern in space does not necessarily involve a major cross-polarization coupling produced by the item. In fact, the PC monitor and the wooden panel have rather different scattering patterns and similar mean XPD values at the same time.

Finally, the plant pot (yellow color in Fig.4.16) does not exhibit any flat surface offering no specular peaks but rather an almost omnidirectional scattering pattern. Depending on the type of material, the size and the shape of the OUT and the spatial distribution of the scattered power, together with the polarization properties of the scattered field, may therefore vary accordingly, becoming so item-dependent features.

4.2.7 RT evaluation

RT parameters tuning results

The analysis of the measurement data suggests that the backscattered field intensity decreases, on average, as the angular distance from specular reflection increases and furthermore, this behavior is shared by almost all the OUT. Therefore, the single-lobe scattering model validated at lower frequencies in several previous studies

([79]) seems still rather reliable also at mmWaves to account for item backscattering. With reference to forward scattering, the model performance seems poorer and more item-dependent.

Preliminary investigation in fact suggests that depending on the amount of inner unhomogeneities, the forward scattered power can be still mainly radiated around the direction of refraction or on the contrary almost uniformly distributed in space (Fig.4.16). Although the single lobe model may not represent in the latter case the best approximation, it is still adopted here devoted to tune the model parameters based on the experimental characterization.

Moreover, the depolarization parameter $\kappa_x pol$ of the DS model embedded into the RT tool has been related to the XPD measured values achieved for the different OUT through the following expression, Degli-Esposti [88]:

$$k_{\mathrm{xpol}} = \frac{1}{1 + 10^{\mathrm{XPD}/10}}$$

Eq. 4.6

It is worth noticing that DS is here intended as any signal contribution not tracked by "standard" RT tool basically because of the limited description of the items in the input database. In practice, since objects are described as made of flat and smooth slab elements, conventional RT models are limited to reflection and refraction from flat, smooth, and homogeneous interfaces, plus diffraction from the border. The ER model aims therefore at modeling everything else.

The XPD values to be included in Eq.4.6 have been therefore computed excluding the TX locations close to the reflection/refraction directions. The corresponding $\kappa_x pol$ values for the considered OUT are listed in the first column of Table 4.4.

OUT	k_{xpol}	ε_R	σ	S_R	a_R	S_T	a_T
Brick wall	0.13	4–8	0.2–0.4	0.2–0.4	2.6–5.4	0.4–0.9	2.3–5.1
PC monitor	0.07	8–16	0.5–1	0.5–0.8	2.1–4.9	0.6–0.9	2–4.6
Bookshelf	0.2	2–3	0.05–0.8	0.2–0.6	2.6–5.4	0.4–0.9	2.5–5.3
Music speaker	0.23	9–19	0.1–0.2	0.3–0.5	2.8–5.6	0.3–0.7	2.4–5.3
Plant pot	0.1	–	–	–	–	–	–
Wooden panel	0.14	2–4	0.1–0.5	0–0.25	2.7–5.5	0.1–0.3	2.6–5.5
Wooden cabinet	0.13	2–10	0.1–0.2	0.15–0.25	2.8–5.6	0.2–0.7	2.6–5.4
Absorber panel	0.28	2–8	0.4–1.2	0–0.2	2.5–5.4	0.2–0.8	2.6–5.4

Table 4.4: suggested values and ranges for the electromagnetic and scattering parameters achieved through the RT-based tuning procedure.

As for the mean XPD values in Table 4.3, a thorough comprehension of the achieved $\kappa_x pol$ values in Table 4.4 require a rather detailed analyses. If the PC monitor is for instance considered, the contribution of diffraction to the scattering pattern far from reflection and refraction directions may be rather important; since diffraction undergoes a limited cross-polarization coupling, this may contribute to explain why the monitor is associated with the lowest $\kappa_x pol$ value in Table 4.4.

Different OUTs, like the brick wall or the wooden panel, have a scattering pattern mainly determined by distributed surface roughness (at least in the backward half-space), and this may explain their corresponding larger $\kappa_x pol$ values. $\kappa_x pol$ estimates in Table are lower than the values presented in Vitucci [121], where $\kappa_x pol$ up to 0.5

has been found at 3.8GHz. Nevertheless, the analyses carried out in [121] are related to real office / urban environments where the propagating waves may undergo multiple interactions, whereas here multipath propagation is basically limited to a single bounce. Assuming that the wave depolarization on the average increases with the number of undergone interactions, the $\kappa_x pol$ values listed in Table 4.4 can therefore represent a lower bound in a very simple scenario, useful to distinguish contribution of a single object. These single contributions may be composed together to obtain the value of $\kappa_x pol$ in more complex scenarios, made of multiple items.

RT parameters tuning procedure

In order to tune also the remaining parameters (other columns of Table 4.4.) of the ER model, the measured received powers for the different rotation angles have been compared with the corresponding predictions provided by the RT tool. RT simulations have been repeated for different values of the scattering parameters (S_R, α_R, S_T, and α_T), and the root mean square error (RMSE) has been then computed over all the rotation angles for each RT run. Suitable values for the sweeping coefficients can be selected based on the RT simulations with the lower RMSE. Such approach has been also extended to the electromagnetic parameters of the OUT (ϵ_R and σ), in order to estimate their values for the OUT, not addressed so far (e.g. the monitor or the bookshelf) and to consolidate their evaluation for the most common objects (like the wall sample and the wooden panel).

Unfortunately, the narrowband RT results have turned out to be not so sensitive for the set-up used to the electromagnetic and scattering parameters to allow a clear identification of a single optimal value for each of them, since several coefficients combinations basically correspond to nearly the same RMSE value. Therefore, in order to find some kind of confidence interval for each coefficient, the better RT runs have been first selected, that is RT simulations corresponding to a RMSE at most 1dB lower with respect to the best one. Among them, the occurrence of each tested value for each RT parameter has been then computed, thus leading at the end to the identification of the ranges of values with higher probability.

The outcome of this procedure is represented in Fig.4.17 for the brick wall case and with reference to the only electromagnetic parameters tuning: the most accurate RT predictions correspond to a relative permittivity ranging between 4 and 8, whereas values around 0.3 should be assumed for the electrical conductivity.

The complete list of results achieved for all the considered RT parameters and for each OUT is reported in Table 4.4. With reference to the electromagnetic parameters, they of course represent effective values not clearly related to the physical properties of any specific material. This may for instance refer to the monitor and the speaker, which are indeed a compound of many very different materials.
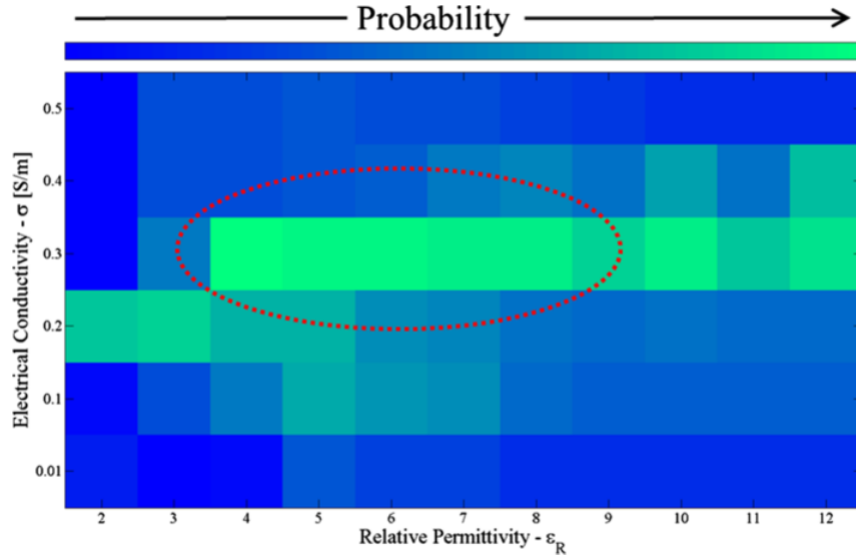
FIGURE 4.17: RT tuning - graphical representation of the outcome of
the RT parameters tuning procedure for the brick wall.

As far as the brick wall is concerned, values of ϵ_R and σ in Table 4.4 are not in full agreement with the existing experimental studies, where ϵ_R values at millimeter frequencies between 2.55, Lu [122], and 4.4 , Cuinas [123] have been found, and σ up to 1.4S/m has been proposed [122]. A general conclusion can be drawn from the overall different investigations: if compared to the values commonly adopted at Below-6GHz frequencies ($\epsilon_R \approx 5$, $\sigma \approx 0.01$ around 1GHz, Pena [120], Bertoni [35]), the permittivity value at mmWaves is basically the same, whereas the conductivity is increased by one/two order of magnitude, that is also in agreement with the already discussed increase of the obstruction loss experienced at mmWaves.

With regard to the wooden panel, the achieved ranges for ϵ_R and σ are fundamentally consistent with the experimental characterization carried out at 60GHz and described in Lu [122], Correia [124].

If the scattering parameters are now considered: since the wooden panel has turned out to be the poorer scatterer among the considered OUT, it is associated in table to both the lowest $S_{R/T}$ values and the highest $\alpha_{R/T}$. This actually corresponds to the lower amount of scattered power in the narrower range of spatial directions. On the contrary, the highest $S_{R/T}$ coefficients together with the lowest $\alpha_{R/T}$ values found for the PC monitor can be related with the mentioned degree of surface irregularities and inner unhomogeneities.

The wall sample shows scattering parameters quite similar to the wooden panel in the backward half-space. In particular, S_R ranges between 0.2 and 0.4, i.e, it is slightly larger than the value 0.2, found in [79], for a brick wall at 1.3GHz.

This seems suggesting that scattering might be richer at mmWaves with respect to lower frequencies but to an extent that could be smaller if compared to the expectations pointed out in several studies.

The achieved results suggest that items backscattering is basically determined by the only surface unevenness and not so much by the inner unhomogeneities. OUT like the wooden panel and the brick wall have somehow similar surface properties and share a similar backscattering behavior (i.e., similar S_R and α_R value), although their inner composition is quite different. The small penetration thickness experienced at mmWaves may explain why the scattering in the backward half-space is weakly affected by what is present beyond the item air-medium surface.

With reference to the forward half-space, the scattered field is always strongly attenuated due to the high obstruction loss, and a widespread spatial distribution of the scattered power can be noticed in presence of evident volume unhomogeneities.

mmWaves brick Wall Scattering Assessment

The overall effectiveness of the procedure carried out to tune the main RT parameters at mmWaves is finally shown in Fig.4.18, where the measured values of the scattered power from the brick wall with tilt = 30°(for different polarization arrangements) are compared with the outcomes of two RT simulations, carried out with the tuned parameters values and with the parameters values commonly adopted at Below-6GHz frequencies (i.e. UHF in figure), respectively.
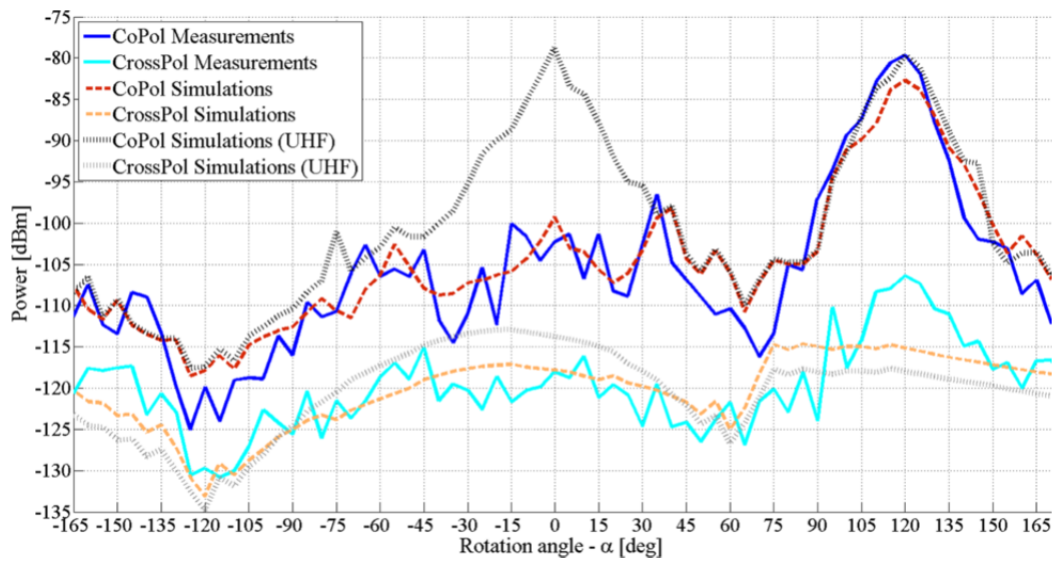
FIGURE 4.18: RT-measurement comparison in co- and cross-polarization - measurement vs simulation prediction in co- ad cross-pol. for the brick wall with a 30°tilt.

Clearly, simulations carried out with the tuned RT parameters fit the measured data rather well, with RMSE equal to 4 for the co- and cross-polarized cases. On the contrary, much poorer accuracy is achieved if the RT is run with the Below-6GHz parameters values ($\epsilon_R = 5$, $\sigma = 0.01$, $S_R = S_T = 0.2$, $\kappa_x pol = 0.05$), with RMSE increasing up to 10dB (co-pol.) and 6dB (cross-pol.).

With reference to the co-polarized case, the worse performance achieved with the UHF parameters is mainly due to the too low conductivity value, which corresponds to a weaker obstruction loss and therefore to a strong overestimate of the received power over the NLOS region (e.g. main peak around 0°in Fig.4.18). Minor changes are achieved in the backward half-space, since reflection is less sensitive to the conductivity value and therefore is approximately unchanged at the two frequencies. If the cross-polarized case is now considered, the received power is basically due only to diffuse scattering (because of the non-zero $\kappa_x pol$ value), since the coherent contributions carry a negligible power because of the polarization mismatch.

With reference to the NLOS OUT orientations, the difference between UHF and mmWaves is the result of some different effects: on one hand, the scattered power at mmWaves is reduced due to the lower amount of transmission, and, on the other

hand, the diffuse scattering at mmWaves is enhanced by the greater scattering coefficient S and the larger $\kappa_x pol$ value. Such effects partly counterbalance each other, and this explains the lower power reduction between the two frequency bands in the cross-polarized case with respect to the co-polarized one. An increase in the received power can be observed if the mmWaves case is compared to the UHF result in the backward half-space. Of course, this is due to the greater S value, for the same reflected power.

4.3   500MHz-400GHz e.m. parameters collection

Concluding the e.m. characterization of materials and objects, it is worth checking if the found results are in line with the literature. In this section is indeed presented a collection of e.m. parameters ϵ and σ, approximately covering a frequency span of 0.5GHz - 400GHz.

Unfortunately, due to the differentiation of possible common materials for indoor furnishing and outdoor spaces, there is generally a large dispersion of values for ϵ and σ, meaning that a range of (min - max) values should be taken into account to characterize a given material, as shown in the Table 4.5 below (in case of dots the relative data are missing). This aspect confirms the role of "effective" e.m. parameters associated to item or objects (as seen before for the PC monitor for example) within ray-based modelling, rather than e.m. values of pure materials, because most of the environment elements (e.g. indoor furnishing) are made of compound materials.

Table 4.5: collected values of ϵ_R (unit-less) and σ (S/m):
(Min ϵ_R - Max ϵ_R / Min σ - Max σ)

Material /	Below-6GHz 1 - 6GHz	mmWaves 6 - 100GHz	sub-mmWaves 100 - 400GHz
Concrete	(5.0 - 7.0/ 0.01 - 0.03)	(4.0 - 6.0/ 0.5 - 2.0)	(6.0 - 12.0/ 1.8)
Ceiling Board	(1.5/ 0.001 - 0.003)	(1.6/ 0.03 - 0.09)	(1.5/ 0.09 - 0.2)
Floor Board	(5.0 - 10.0/ 0.008 - 0.09)	(3.0 - 6.0/ 0.7 - 2.0)	(. . .)
Ground	(3.0 - 30.0/ 0.01 - 1.5)	(3.0 - 5.0/ 0.4 - 15.0)	(. . .)
Brick Wall	(3.0 - 5.0/ 0.01 - 0.07)	(2.0 - 4.0/ 0.04 - 1.0)	(2.2 - 3.0/ 2.0 - 4.8)
Plasterboard	(2.0 - 3.0/ 0.002 - 0.06)	(1.6 - 3.0/ 0.03 - 1.5)	(3.0 - 4.4/ 1.4 - 7.0)
Glass	(3.0 - 6.0/ 0.001 - 0.35)	(3.0 - 9.0/ 0.06 - 1.0)	(6.0 - 7.0/ 0.7 - 9.0)
Wood	(1.2 - 3.0/ 0.001 - 0.3)	(1.5 - 2.8/ 0.14 - 1.4)	(1.7 - 2.0/ 0.35 - 2.7)
Chipboard/Plywood	(2.5 - 3.2/ 0.01 - 0.07)	(1.6 - 4.5/ 0.1 - 2.0)	(2.3/ 0.6)
Plastics	(2.0 - 2.5/ . . .)	(2.0 - 3.0/ 0.005 - 1.1)	(2.3 - 3.0/ 0.9 - 1.3)
Water	(60.0 - 80.0/ 0.15 - 21.0)	(8.0 - 30.0/ 35.0 - 82.0)	(. . .)
Human Skin	(35.0 - 41.0/ 0.9 - 8.0)	(8.0 - 15.0/ 14.0 - 44.2)	(. . .)

All the previous data are mainly taken from the following recapped references:

- Wideband: ITU Rec. [125], [117], from 1GHz to 100GHz, Korolev [126] from 30GHz to 120GHz, Chahat [127] from 2 to 60GHz, Ferreira [128] from UHF to mmWaves;

- UHF (Below-6GHz): Rhode and Schwarz [100] at 2.45GHz, Mohtashami [129] at 2.45GHz, Navarro [130] at 600MHz, Yang [131] at 900 and 1800MHZ, Layer [132] at 5.2GHz, Jemai [133] at 2.45GHz, Cuinas [134] at 5.8GHz, NIST NLS Phase 2 research team [135] from 0.5 to 8GHz;

- cmWaves (6-30GHz): Feitor [136] at 18GHz, Ellison [137] at 23 and 36GHz, Saunders [138][139] at 17GHz;

- mmWaves (30-100GHz): Feitor [136] at 60GHz, Ellison [137] at 89GHz, Shokou [140] at 60GHz, Felbecker [141] at 60GHz, Lu [122] at 60GHz, Gurialiuc [142] at 60GHz, Ghaddar [143] at 60GHz, Pugliese [123] at 60GHz, Saunders [138] at 60GHz;

- sub-mmWaves (above 100GHz): T. Kuerner works as [144], [145], [146] , [75], [147], [148][149].

Table 4.5 confirms a general trend: increasing the frequency there occur minor changes in (ϵ) but a significant raising in (σ) (e.g. the σ of glass can start from 0.001 reaching up to 10.0), which implies proportionally higher penetration losses, as naturally expected.

This fact could be particularly noticeable regarding the reaction of the e.m. field with human body, usually investigated mainly for health and safety/exposure purposes, but not so vastly for wireless communications purposes. Of course, the human body is much more complicated than building walls, because of its non-homogeneous composition and high water content, so affecting the RF signals both in near and far field regions, considerably. An example of pure water complex permittivity is given in Fig.4.19, where both real and imaginary parts falls disruptively past 10GHz approximately. A complete description of the problem can be found in Zhadobov works as [150], [151] [152] and in the literature about Body Area Network, Pellegrini [153].
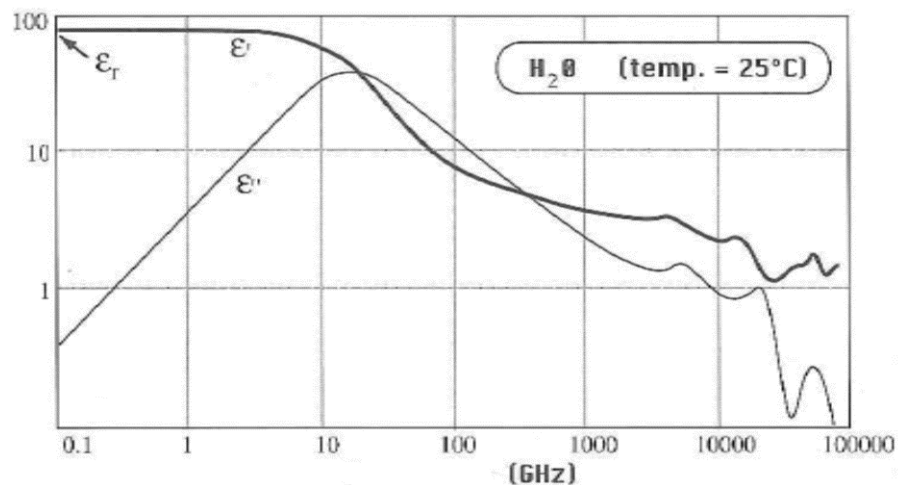
FIGURE 4.19: Behavior of the complex permittivity of pure water versus frequency.

Concluding, the presented interesting results are not definitive, because only partial information about the nature of materials has been possible to retrieve. Missing information as the water content (humidity), the surface and inner irregularities, polarization de-coupling or even measurements set-up issues, are likely to lead to uncertainties in ϵ and σ. These are the main reasons why results show so large range of values, especially for σ. Additional measurements are necessary to gather today enough data for deterministic channel modeling as RT for Below and Above-6GHz, systematically.

Chapter 5

Multidimensional mmWaves Radio Channel Characterization

5.1 Analysis of In-Room mmWaves Propagation: Directional Channel Measurements and Ray Tracing Simulations

5.1.1 Introduction

As seen before, due to the tiny wavelength, mmWaves wireless systems are expected to house large antenna arrays enabling the implementation of multi-antenna systems schemes. The effectiveness of such techniques depends on the multidimensional and wideband properties of the channel (e.g. space / time dispersion multipath correlation properties), and therefore the design of wireless systems operating in the mmWaves band will benefit from a thorough multipath propagation characterization, Martinez-Ingles [154] and [155]. After an item-level investigation on the e.m. behavior of different items, now it is time for a complete scenario analysis: in-room wireless propagation at around 70GHz is investigated by means of directional channel measurements using RT simulations as both an analysis tool and a reference propagation model to be assessed and calibrated.

Special attention has been devoted to the role played by diffuse scattering. For instance, Fan [156], the mmWaves radio channel seems dominated by specular interactions, with negligible scattering effects, and according to Haneda [157], at least 80% of the received power at 60-70GHz is shown to be carried by specular contributions. Whether diffuse scattering becomes stronger or weaker at mmWaves with respect to lower frequencies is still under debate, Haneda [158], and even conflicting analyses can be found in the literature.

5.1.2 Measurement Setup

MmWaves measurements ([159]) have been carried out in a small office located at the TU Ilmenau during daytime with no people around. The same environment will be exploited also in chapter (7) for Multi-User BF studies. The room, which has a size of nearly 20 square meter, is representative of most small-office environments and contains usual indoor furnishing objects like wooden desks, cabinets, a PC, etc. as sketched in Fig.5.1 and Fig5.2. Lateral and ceiling walls are made of slightly rough concrete, whereas the floor consists of a thin carpet on the gross concrete of the ground. Two thick windows surrounded by a wide metallic frame and a large heat radiator are present on the upper wall, whereas a heavy metallic door (kept close during the measurements) and a thin metallic blackboard are located on the opposite wall.

FIGURE 5.1: A corner of the small office with TX and RX units.
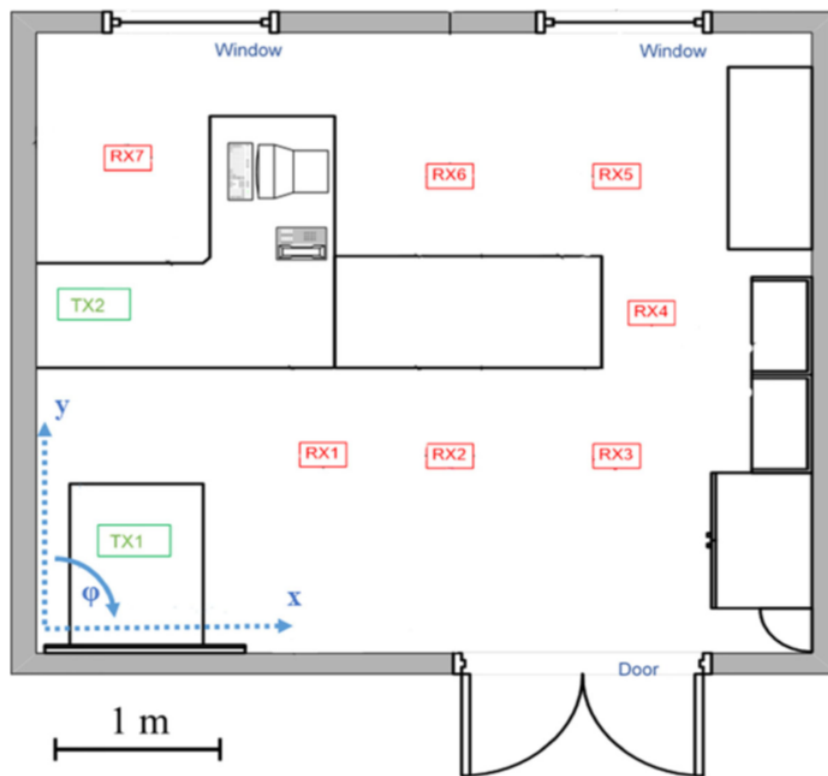
FIGURE 5.2: 2D map of the indoor office. TXs in green and RXs in red. Some details in blue. (Top view).

The measurement system is the same TU Ilmenau CS already described in the previous chapter for Item level characterization. In this small office the setup involves different transmitter (TX) and receiver (RX) positions as shown in Fig.5.2. The TX antenna is 2.45 m high, mounted on a stable plate on a 3D positioner. In

order to mechanically emulate a smart in-room access point: TXs can sweep both the elevation (El) and the azimuth (Az) planes in 15°steps, obtaining 13x13 spatial samples for TX2 (Fig.5.3) and 13x7 spatial samples for TX1 (Fig.5.1), respectively.
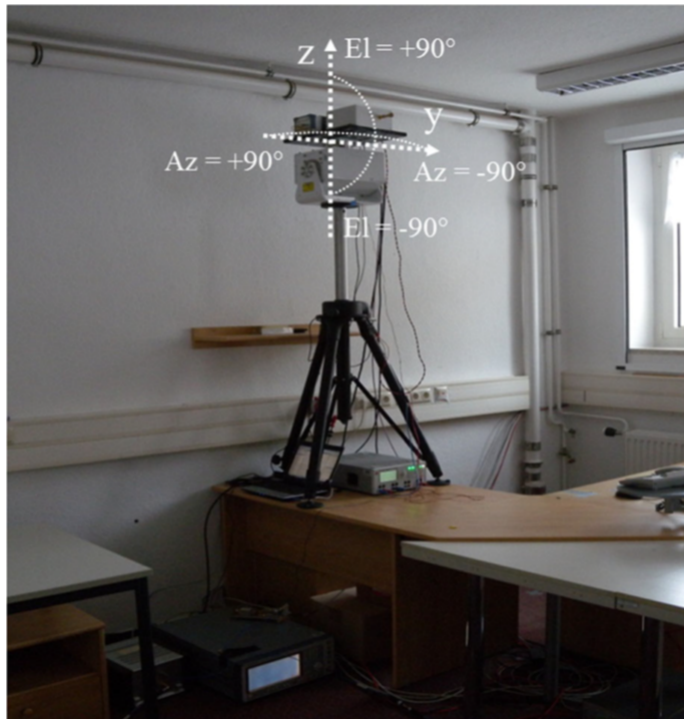

FIGURE 5.3: TX2 mounted on the rotational positioner. Angular co-ordinates are overlaid in white.
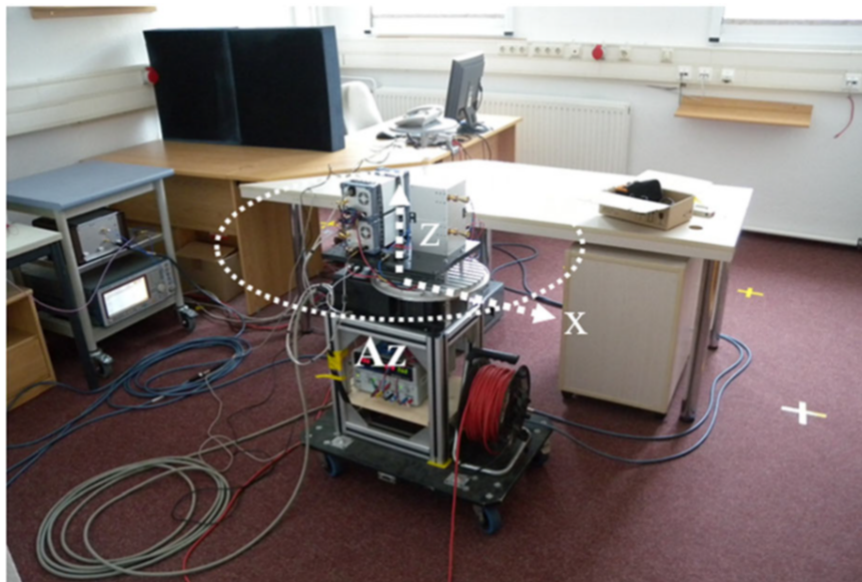
FIGURE 5.4: RX mounted on the rotational positioner at position 2 in the office. Angular coordinates are overlaid in white.

The RX equipment (Fig.5.4) is lightweight and mobile. In order to emulate different user positions, it has been moved over 7 positions inside the room (Fig.5.2).

The RX antenna is 0.9 m high over the ground and capable to scan only the azimuthal range from 0°to 360°in 15°steps at 0°elevation, corresponding to 24 different orientations. For every measurement position, the CS system response has been de-embedded in the frequency domain using back-to-back calibration and noise has been removed in the time domain using a threshold algorithm.

Cylindrical dual polarized horn antennas have been used at both the link ends, having a gain of 20dBi and a HPBW of about 15°, equal to the rotational step of the positioners, in order to limit the contribution of the same multipath components to different angular samples. Owing to these properties, the measurement setup is as much as possible representative of future mmWaves wireless system configurations, where the access-point is equipped with a large beamforming array, while the receiver can perform either an omnidirectional antenna if no pointing technique is implemented, or a directive beamforming antenna with a relatively limited pointing capability. To simulate occasional obstructions of the LOS, NLOS configurations have been realized in a couple of cases (TX1-RX7, TX2-RX4) through the introduction of an absorbing panel properly placed on the tables and close enough to the RXs.

5.1.3   Ray tracing Simulation

The setting of the main RT parameters is sketched in Table 5.1, corresponding to the well-known trade-off between computational effort and prediction accuracy. The RT geometrical input database consists of a vectorial 3D representation of the small office including the building frame (walls, ceiling and floor) and openings (door and windows-metallic frame included), the visible elements of the hydraulic and electric installations (heat radiator, ceiling lamps, external pipes and ducts), and the largest furnishings objects (tables, cabinets), as depicted by Fig.3.14.

Maximum number of interactions for each ray	6
Maximum number of reflections (R) for each ray	4
Maximum number of diffractions (D) for each ray	1
Maximum number of transmissions (T) for each ray	6
Combined reflection and diffraction (RD)	Included
Combined scattering and reflection (RS)	Included
Angular step for ray launching of scattering rays (elevation and azimuth)	5°

Table 5.1: Ray Tracing main simulation settings. See chapter (3) for details.

The electromagnetic parameters of the items, evaluated in the previous chapter, have been now used properly in the RT database to support reliable channel predictions at 70GHz. Especially, "effective" (ϵ,σ) are set for the PC monitor. The values reported in the Table 5.2 below are also partially gathered from the current literature for mmWaves bands.

Item	ε_R Value	σ Value	S_R Value	S_T Value
Wall	4.4	1.0	0.5	0
Ceiling	4.4	1.0	0.5	0
Floor	4.4	1.0	0.7	0
Table	2.8	0.15	0.2	0.3
Closet	2.8	0.15	0.2	0.3
Window	6.25	0.7	0	0
Cable Duct	2.25	0	0.2	0.2
PC	10	0.8	0.8	0.8
Monitor				
Ceiling Lamp	2.0	1e8	0.7	0

Table 5.2: e.m. material parameters for RT simulation at 70GHz.

5.1.4 Analysis of Results

In the following, CS measurements are analyzed and compared with RT simulations to determine radio channel characteristics and RT performance. RT predictions are known to be sensitive to the description of both the scenarios. The accuracy of RT simulation may therefore be limited by environment description errors. Geometrical description of the environment has been derived manually through visual inspection on-site.

Narrowband Analysis

For both RT simulations and measurements, the received power for each RX positions has been computed by adding up power contributions received from all TX and RX antenna orientations. At the RX side, this corresponds to representing the antenna as an omnidirectional antenna in the horizontal plane. The comparison between measured and RT-predicted power is shown in Fig.5.5 for both transmitter positions and confirms a good agreement for all RX positions, with a root mean squared error (RMSE) equal to 3dB and to 1dB for TX1 and TX2, respectively.
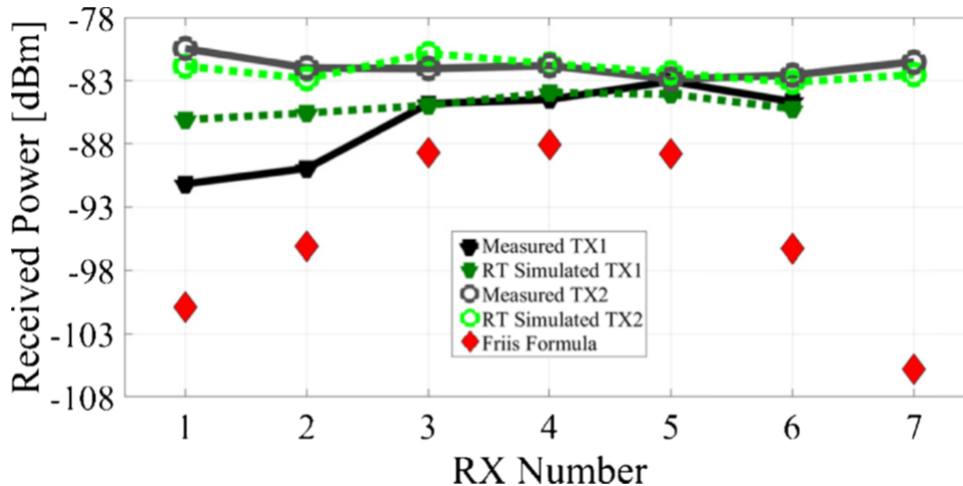

FIGURE 5.5: Comparison between measurements and different models prediction for the LOS situations related to the TX2 case.

The power contribution from the LOS path only (e.g. Friis Formula) is far below the actual received power, especially in RX positions closer to the TXs, where the LOS path has a high elevation angle and is thus attenuated by the low gain of

the RX antenna for that direction. Only including room multipath the agreement is satisfactory: this confirms that multipath plays a crucial role even in LOS conditions for the chosen setup, in terms of power. The RT narrowband prediction capability has been checked against measurements also in NLOS conditions, with an overall accuracy in essential agreement with the LOS cases (prediction error equal to 2dB and 3dB for TX1-RX7 and TX2-RX4, respectively).

Angular Dispersion

In order to investigate multipath spatial properties, power angle profiles (PAP) have been derived at the TX side, exploiting the wide angle of departure range both in elevation (-90°, + 90°) and azimuth (0°,90°for TX1, -90°,90°for TX2). The power value within each 'pixel' is computed by integrating every directional CIR (i.e. for given TX/RX pointing directions) and then summing up the 24 spatial power samples corresponding to the different pointings of the RX antenna. This analysis therefore refers to a TX-only beamforming scheme with an omnidirectional RX antenna. See chapter (7) also.

An example of the normalized (e.g. 0dB) measured and simulated PAPs are respectively shown in Figs.5.6 and 5.7 for the TX2-RX4 pair. The simulated PAP without diffuse scattering is also reported in Fig.5.8 for reference.

The measured PAP is quite well reproduced by the RT tool for elevations limited to the range (-60°, 15°), whereas a general underestimation of about 10dB is present when the TX antenna is pointing towards the ceiling or the floor. This disagreement for large elevation is a common trend for all the TX-RX pairs and may be attributed to several reasons:

- 1) the possible presence of unknown, metallic layers/grids underneath the ceiling/floor surface, which may affect back-scattering from those surfaces, Vitucci [160];

- 2) inaccuracies in the description of antenna radiation pattern, especially secondary lobes when the TX antenna is pointing away from the RX location;

- 3) scattering coefficients not fully optimized for the considered scenario, that can degrade prediction accuracy for large elevation angles, when diffuse scattering appears important.

The most important clusters marked as A-E in Fig.5.7 are better analyzed in Table 5.3, using RT as a tool to identify the major propagation mechanisms.

Cluster	Az	El	Mechanisms	Objects
A	−75°	−15°	Multiple reflection	Walls/windows
B	−45°	−15°	Single reflection	Walls/windows
C	0°	−30°	Direct LOS	–
D	60°	−15°	Single/double reflections	Walls/windows/door
E	−60°	−45°	Scattered rays	Windows frames/cable ducts/radiator

Table 5.3: analysis of the main detected cluster in TX2-RX4 case.
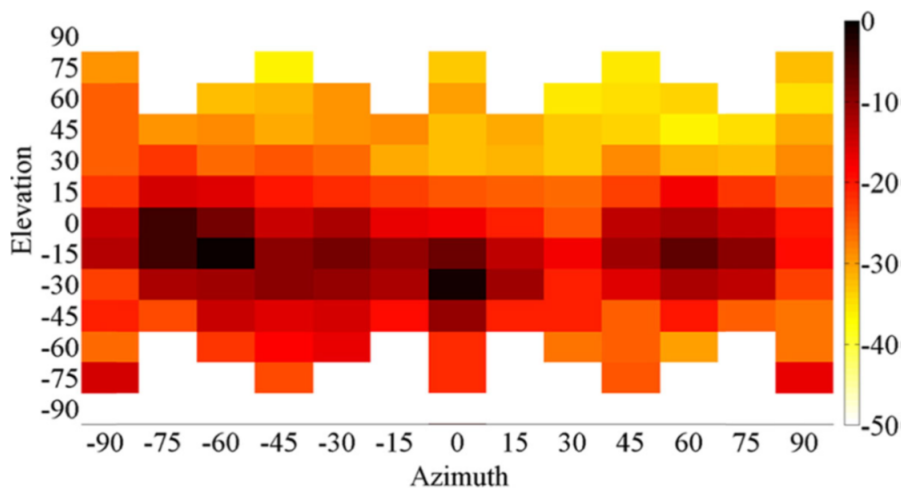
FIGURE 5.6: Measured PAP (TX2-RX4, LOS) in dB units.
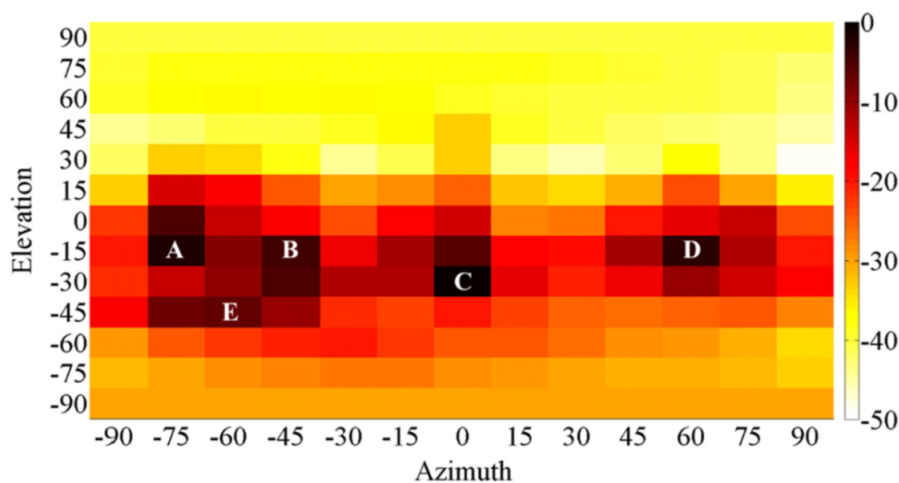
FIGURE 5.7: RT simulated PAP (TX2-RX4, LOS) in dB units; strongest clusters highlighted with labels (A-E), see also Table 5.3.
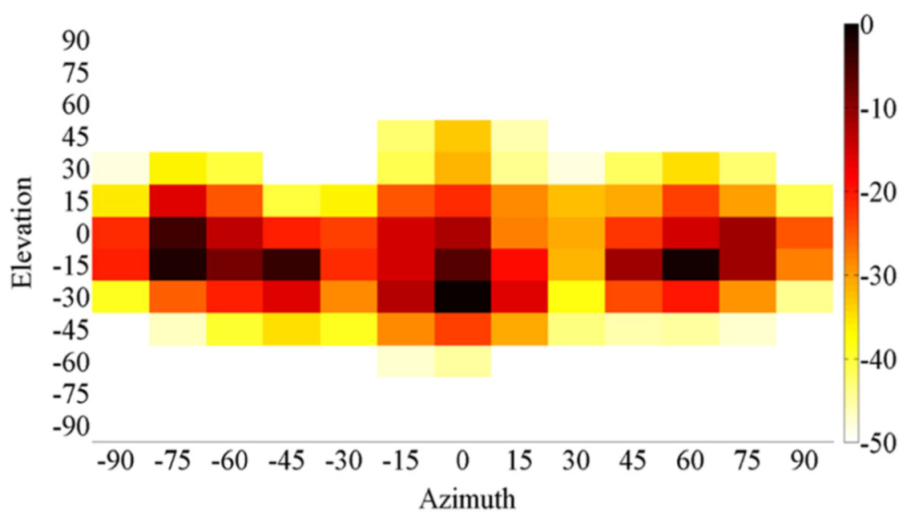
FIGURE 5.8: RT simulated PAP (TX2-RX4, LOS) in dB units without scattering.

At the same time, diffuse scattering is not negligible because simulation without diffuse scattering yields a much more empty pattern, especially outside the elevation range (-60°, 15°), and without the "halo" around the major specular contributions. This is true for all RX positions, suggesting that diffuse scattering is a minor but non-negligible mechanism, especially with regards to spatial channel spreading. Furthermore, the cluster analysis in Table 5.3 also suggests that the strongest multipath contributions (clusters A, B, D) are fundamentally produced by interactions of the radiated wave with the macro-structure of the office, consisting of the building carrying structure (walls, floor and ceiling) and the openings on the walls (windows, door). To a lesser extent, smaller items may also determine still powerful replicas of the transmitted signal, especially if they are made of metal (e.g., cluster E - windows frame, heat radiator).

The overall PAP prediction accuracy of RT is assessed in Tables 5.4 / 5.5 using the root mean square error (RMSE), and the weighted RMSE (named WRMSE), computed for each available PAP and averaged over all RX locations. WRMSE is a simple modified version of the common RMSE due to the independence between RMSE and the intensity of the PAP for each angle of departure.

TX1	RMSE		WRMSE	
RXs	With scat.	Without scat.	With scat.	Without scat.
1	12.9	21.7	4.6	5.7
2	11.3	22.2	4.4	6.5
3	7.2	19.0	2.1	5.4
4	8.4	21.4	2.5	3.9
5	10.8	22.3	4.1	5.0
6	8.7	18.3	2.5	3.4
7 NLOS	13.0	22.2	4.8	6.3
Average	10.3	21.0	3.6	5.2

Table 5.4: PAP errors TX1.

TX2	RMSE		WRMSE	
RXs	With scat.	Without scat.	With scat.	Without scat.
1	10.2	21.1	3.1	6.3
2	10.0	22.0	3.0	5.1
3	8.9	23.1	2.2	4.2
4 LOS	8.0	22.7	3.1	6.7
4 NLOS	7.9	22.6	2.0	4.1
5	8.1	22.3	1.9	3.5
6	10.5	23.4	3.2	5.7
7	9.7	20.3	3.1	5.6
Average	9.2	22.2	2.7	5.2

Table 5.5: PAP errors TX2.

In fact, two equal errors affecting a strong and a weak contribution impact on the RMSE exactly in the same way. Therefore, the RMSE has been also computed by weighting each error with a coefficient equal to the relative power of the corresponding pixel of the PAP plots above, similarly to what happens with the propagation delays for the evaluation of the RMS delay spread. Thus, the weighted RMSE in

tables represents a more meaningful performance metric. In fact, the WRMSE values slightly increase if scattering is excluded from the RT simulations, reflecting the relatively modest power contribution of scattering compared to specular contributions.

Temporal Dispersion

Temporal dispersion is a further issue to be considered for the design of the forthcoming multi-gigabit wireless networks, since frequency selectivity may in principle arise in case of very large data rates. In order to de-embed the antennas influence on the DS values, power delay profiles (PDPs) related to isotropic (TX) / omnidirectional (RX) patterns have been extracted from the available directional measurements. That is, an overall PDP has been derived for each TX-RX pair properly combining the CIR corresponding to the different antenna pointings, and the DS values have been then computed (Tables 5.6 / 5.7 for TX1 and TX2, respectively). This choice is motivated by the need to extract the properties of mmWaves channels, typically sounded with directive antennas, as fair as possible compared to Below-6GHz channel, where omni antennas are usually considered.

TX1	Meas. DS (nsec.)	Predicted DS (nsec.)		Relative DS Error %	
RXs		With scat.	Without scat.	With scat.	Without scat.
1	8.1	7.7	8.2	−5	+1
2	8.8	8.4	7.6	−5	−14
3	9.4	10.7	11.0	+14	+17
4	9.1	10.3	10.7	+13	+18
5	9.1	11.0	11.5	+21	+27
6	9.2	10.4	12.0	+13	+30
7 NLOS	7.2	6.9	7.4	−4.2	+2.8
Average	8.7	9.3	9.8	6.9	12.6

Table 5.6: DS errors TX1.

TX2	Meas. DS (nsec)	Predicted DS (nsec)		Relative DS Error %	
RXs		With scat.	Without scat.	With scat.	Without scat.
1	8.5	8.1	7.9	−5	−7
2	8.7	7.4	9.1	−15	+5
3	8.9	8.7	10.0	−2	+12
4 LOS	8.6	10.5	11.7	+22	+36
4 NLOS	8.9	9.2	9.7	+3	+9
5	9.2	8.6	10.4	−7	+13
6	8.9	8.1	8.7	−9	−2
7	7.4	10.1	9.3	+37	+26
Average	8.6	8.8	9.6	2.3	11.6

Table 5.7: DS errors TX2.

Tables above clearly show that scattering contributes to reduce the in-room delay spread in the indoor scenario tested. This result apparently conflicts with what found in previous studies carried out at lower frequencies in outdoor scenarios, Fuschini [86], Degli-Esposti [80], Mani [161], but it can be explained by the different role played by the scattering phenomenon in the different environments.

Diffuse scattering can dramatically increase the number of propagation paths due to the greater divergence of the wavefront with respect to reflection and diffraction. For the same reason however, scattered paths are generally weaker. Multiple-bounce scattered rays are usually negligible in practice, whereas single scattered ones can be important or not depending on the propagation conditions. In outdoor scenarios far objects (i.e. buildings) with direct visibility to both the TX and the RX are often present and a single scattering interaction may produce significant long-delayed echoes, thus increasing the DS value. In contrast, far scatterers cannot be present in a single room, where large delays (long traveled paths) must always correspond to a proportional number of undergone interactions. Therefore, single scattered contributions here have quite short delays, meaning that in room scattering effects mainly affect the "head" of the PDP, corresponding to a (limited) reduction of the delay spread.

This general analysis is corroborated by the DS assessment in Tables 5.6 and 5.7, where typical values of Delay Spread are around 8-9 nsec, given the measurement set-up of the study. Moreover, the extension of the RT prediction to diffuse scattering actually reduces the DS value in 12 case over 15, as shown also by Fig.5.9, where the simulated power delay profiles (PDPs) with and without scattering are shown for the TX2-RX4 case as a reference.

The highest peaks are shared by both the PDPs and correspond to the specular multipath components (i.e., reflections), whereas diffuse scattering clearly "fills the holes" between the specular contributions, since it has not to comply with strict geometrical constraints. Although the intensity of the diffused components undergo some fluctuations along the profile, the most delayed ones are clearly the weakest (at least 30dB lower than the highest peaks) and, therefore, can be neglected in practice. Conversely, the most powerful scattered contributions occur at quite short delay, and actually belong to the head of the PDP in line with the previous, general conclusion that in-room scattering can be expected to reduce the delay spread.
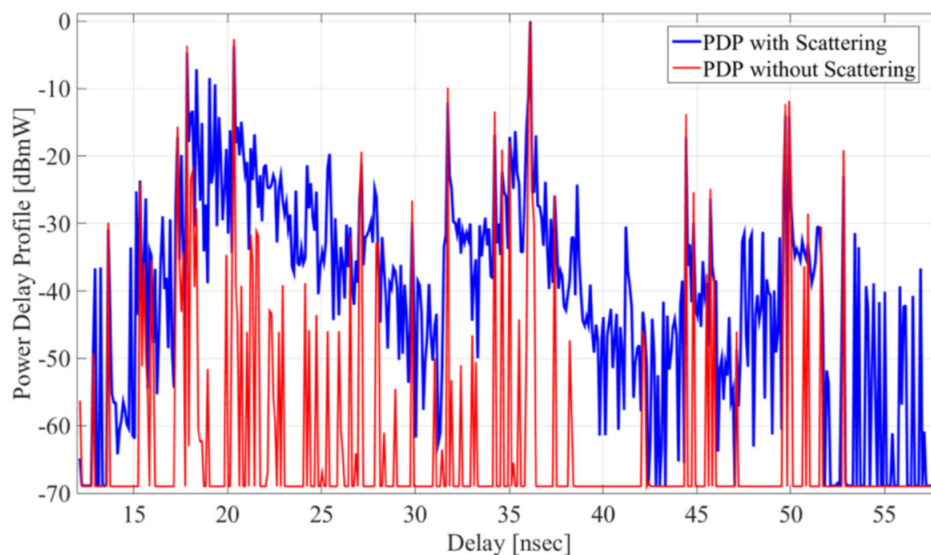
FIGURE 5.9: Predicted PDP with and without scattering (TX2-RX4, LOS).

In agreement with the previous considerations, taking into account only simulations, Fig.5.10 shows that DS slightly decreases for increasing values of the backward scattering coefficient (arbitrarily modified in the RT settings) of the office walls.

Furthermore, $S_R = 0.5$ (corresponding to a 25% of backscattered power) represents, overall, a realistic estimate for the considered scenario. This value is greater than the scattering coefficients values adopted in previous studies carried out at frequency Below-6GHz, Mani [84] and Fuschini [81]. In conclusion, diffuse scattering due to wall irregularities at 70GHz seems slightly stronger than at sub-6GHz frequencies in absolute terms, but it nevertheless represents a relatively minor interaction mechanism for in-room propagation.
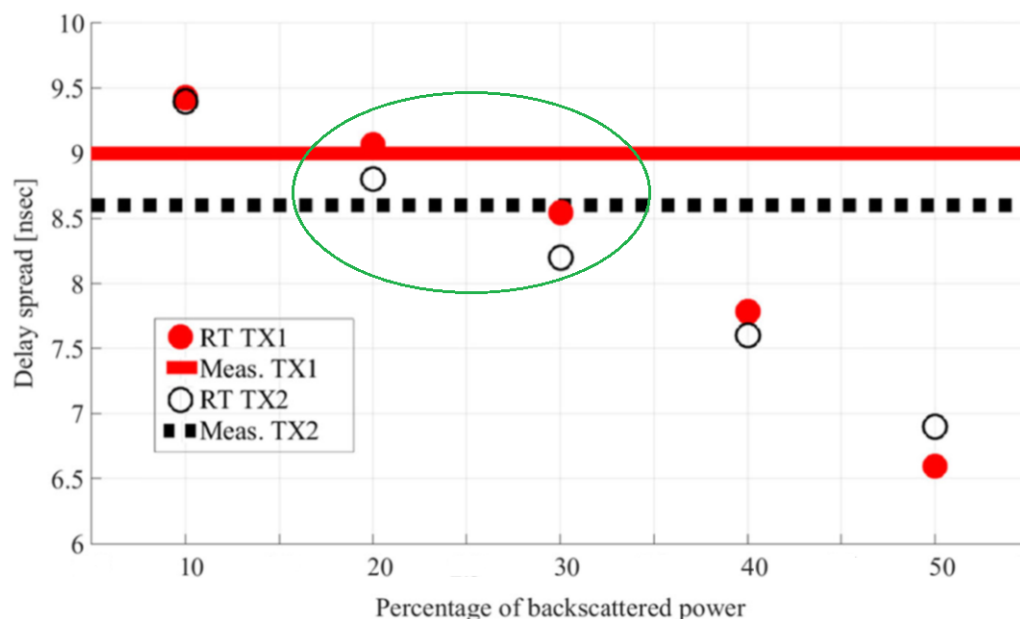
FIGURE 5.10: Delay spread values vs. percentage of backscatter power. The horizontal lines correspond to the measured values whereas the filled circles are the RT predictions for the two TX locations.

5.1.5 Analysis of Propagation Mechanisms

According to the previous analysis, in-room multipath propagation aspects are further investigated through RT simulations, as in Fig.5.11, where the contribution to the received power are separately computed through RT simulation for each interaction mechanism and for their combinations (e.g., (SR) corresponds to the power carried by rays experiencing both scattering (S) and reflection (R), no matter the order of the interactions).

The power values for the different mechanisms have been computed for each TX-RX pair (always with Omni RXs), and have been then 'averaged' over the RX locations in order to achieve a comprehensive evaluation for each TX. Absolute power values are reported on the vertical axis to allow direct comparison between the TXs, whereas the corresponding relative percentage values are shown alongside the stacked bars.

It is worth noticing that the percentages are related to the overall received power from the rays undergoing at least one bounce, i.e., excluding the direct path. In the following this is referred to as NLOS received power, since it represents the power that would be received if the LOS path were totally obstructed.
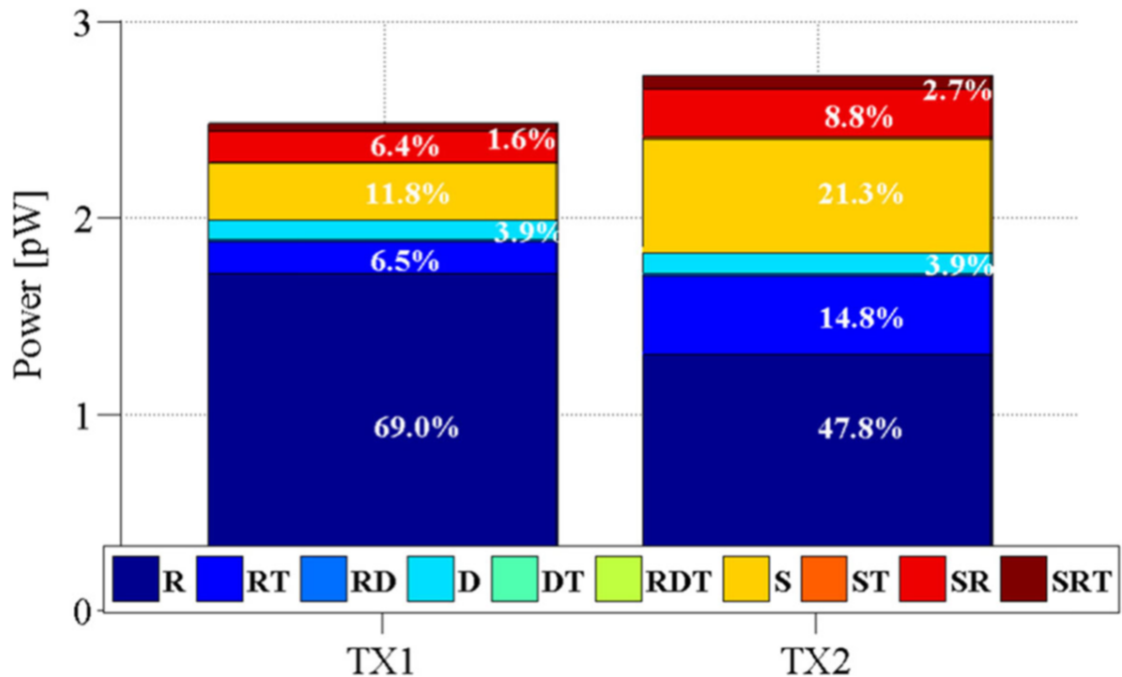
FIGURE 5.11: Contribution of the different propagation mechanisms
to the in-room received power: analysis based on RT simulation re-
sults.

Figure 5.11 clearly confirms that reflection represents the dominant propagation interaction, since it contributes to convey the majority of the NLOS received power ($\sim$ 80% and $\sim$ 70% for TX1 and TX2, respectively). Instead, diffuse scattering is responsible for an amount of NLOS power approximately ranging from 20% (TX1) to 30% (TX2).

Diffraction seems fundamentally negligible in the propagation process, in agreement with the conclusions drawn by Jacob [162]. Rays experiencing transmission only are not present due to configuration of the RX locations, being some of them in LOS condition with the TXs, and some others obstructed by the absorber, which is assumed non-penetrable due to the very high transmission loss. If combined with reflection or scattering, transmission contributes to nearly the 15% - 25% of the NLOS power, for TX1 and TX2, respectively. This higher than expected value is due to transmission through tables and cupboards which have a low thickness and are made of wood or fibreboard.

Looking at the absolute power values, the scattered power received from TX2 is twice as much than the one from TX1. This is probably due to TX2 position, which is able to illuminate through scattering three out of four lateral walls (top, bottom and right side in Fig.5.2), whereas TX1 only illuminates two of them (top and right side). At the same time, TX1 propagates to the RXs a much larger reflected power than TX2 (69% vs. $\sim$ 48%). It seems that moving the TX towards the room corner seems to reduce scattering with respect to reflection. This is probably due to the different inclination of the reflected paths to the RXs for TX1 and TX2.

Summarizing the results, it is worth noticing that the ratio between reflection (SMC) and diffuse scattering (DMC) is essentially in line with literature, where at least 80% of the received power has been attributed to specular interactions. However, the use of antennas placed at the same heights (e.g. only azimuth scanning) can contribute to explain the slightly larger relative amount of reflected power found in

Haneda [157], since in that case the stronger reflections are expected to occur in the horizontal plane. In the measurement setup here instead, since the reflected paths reach the RXs with higher elevation angles due to the difference in the antennas heights, and experiencing a lower gain of the receiving antenna. This all due to the lack of elevation scanning at RX, preventing from LOS alignment between TX and RX.

Moreover, this fact has a noticeable impact on the ranging of the dynamic range with which Channel Sounder results have been evaluated: since the strongest paths are not LOS, they do not have so a larger power values with respect to others multipath clusters (e.g. reflections). In fact, within the power "window" between the maximum power received and the noise floor level (e.g. dynamic range), all the propagation paths were visible. This explains how it is has been feasible to observe clearly DMC multipath, even though naturally weaker than SMC.

5.1.6 RT Sensitivity to the Environment Description

In addition to the environment database considered so far, which includes main walls and major pieces of furniture such as windows, tables and big metal pipes (named "Furnished" in the following), a more detailed representation of the small office ("Detailed" in the following) including minor pieces of furniture such as computer monitors, the blackboard, some shelves, has been considered to assess the corresponding impact on RT simulation results. Computer monitors and shelves have been modeled as dielectric slabs. The longer computation time required by the detailed representation of the environment does not pay off in terms of better performance, especially for DS prediction, as shown in Table 5.8.

		Furnished	Detailed
TX1	Received pow. RMSE [dB]	2.8	3.2
	PAP WRMSE [dB]	3.6	3.4
	Relative DS Error (%)	6.9	19.9
TX2	Received pow. RMSE [dB]	0.7	2
	PAP WRMSE [dB]	2.7	3.5
	Relative DS Error (%)	2.3	17.4
RT simulation time [min]		150	180

Table 5.8: comparison of RT prediction performance for different accuracy in the description of the environment.

A possible explanation to this surprising result can be found considering that the smaller objects were measured and inserted into the database with the same manual procedure used for bigger objects, and therefore errors in the shape and position of them are relatively greater compared to their smaller size. Besides, the material composition and the corresponding electromagnetic properties of small objects, such as computer monitors less studied than those of walls, tables, and doors.

Although with several differences in the considered approach, the preliminary analysis sketched here is in agreement with what found by Jarvelainen [163], where a looser point-cloud description of an indoor environment yields nearly the same prediction accuracy as a more detailed point-cloud representation.

In conclusion, a description of the environment extended to smaller items does not seem to guarantee better RT accuracy, especially if the geometrical description of such objects is not very precise and the scattering/electromagnetic properties of such small objects are largely unknown.

Chapter 6

Multi-antenna Systems

According to information theory, Beamforming is usually considered a special case of MIMO technique. Nevertheless, Beamforming herein is taken apart because: first, theoretically, it involves an antenna arrays approach unrelated (directly) to information theory and, then, practically, its realization has been historically dependent on analog circuits rather than digital signal processing (DSP). The theoretical basics of multi-antenna schemes are illustrated in the following to support advanced considerations of the next chapter (7), where BF applications in indoor scenario are investigated. Hardware and RF circuits aspects can be found in Appendix.

6.1 MIMO

6.1.1 A simple overview on MIMO

The origin of MIMO can be traced back to the late '70s, but the real research 'boost' on this revolutionary technology took place in the '90s as testified by the pioneering works of Foschini [164] [165], Alamouti [166], Tarokh [167], Gans [168], Telatar [169], Marzetta [170], Paulraj [171] and Calderbank [172].

After the initial theoretical phase, a significant effort in the research community has been dedicated to the development of effective multiple antennas communications, leading to advanced concepts as MU-MIMO (multiple users), Cooperative-MIMO (distributed collaborative antennas), Massive MIMO (very large antenna arrays, Marzetta [173]), and, of course, mm-Wave MIMO Above-6GHz.

Today MIMO is the most claimed technology for wireless applications, due to its revolutionary benefits (Goldsmith [174]) and noticeable complexity, too.
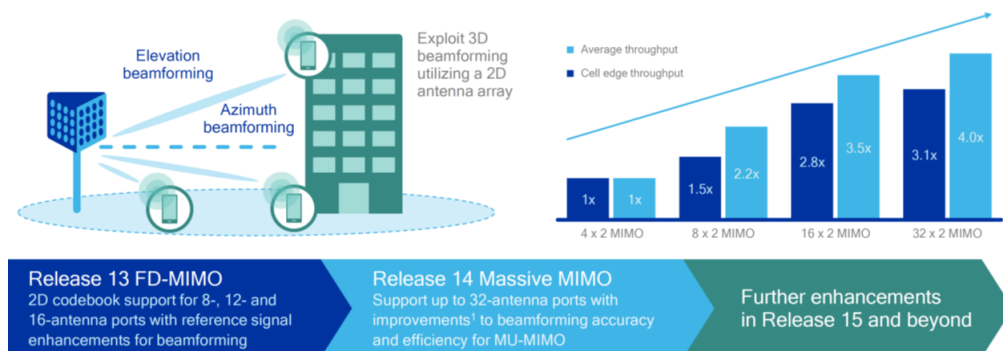

FIGURE 6.1: 3GPP insight about MIMO technology.

In practice, as reported in Fig.6.1 by 3GPP in Rel.13/14/15, the smart exploitation of the radio channel characteristics in terms of MIMO technology is the way to make the throughput take off, even though at expense of more or large RF equipment.

Physically, the pros of MIMO (e.g. boosting capacity and / or reducing errors) derive from the larger degree of freedom offered by the use of multiple antennas. Of course, there is a price to pay concerning the complexity of handling (at best) the joint transmission and reception of more signals at once, Mietzner [175].

6.1.2   Diversity

Before focusing on the modern MIMO pros and cons with respect to Above-6GHz, it is necessary to talk about Diversity: let's make an example with two antenna ports (properly located far away, e.g. $\lambda/2$) instead of one at RX side. If on the first antenna comes a sample (or symbol) corrupted by multipath, there is still a chance to obtain a good signal on the other one. Thanks to the distance between the antennas, the RX is actually capable to 'listen' to two radio channels, and then to increase the quality of the link, statistically speaking. It is worth paying attention on the fact that these advantages do not come only from the gathering of more power but from the diversification of received samples.

In fact, diversity can be considered the 'forefather' of MIMO since diversity combining techniques as Maximal Ratio combining (MCR) (Brennan [176], Lemieux [177] and Balaban [178]), are well-known algorithms designed to achieve the optimal SNR properly mixing the multiple signals available on the antennas. The guiding principles are to allocate power at TX or to acquire power at RX from where it is worth knowing the 'conditions' of the radio channel. The general case of MIMO, can be expressed with a notation as $N_T x N_R$ indicating that TX has N_T antennas elements and RX N_R, simply.

6.1.3   Channel State Information

A key point to master is the cost required for MIMO: any combining scheme can take advantage from information about the radio channel, i.e. the knowledge about the multipath that affects signals. This is named Channel State Information (CSI). In the example above, the CSI were the insight about the bad and good quality of reception onto the two different antennas. The RX cannot be aware of CSI a priori and cannot retrieve CSI "externally".

CSI depends only on the capabilities of terminals to sound the channel and estimate its nature. This is not a trivial task, because CSI can change in time and space. For example, in practice, CSI in LTE is estimated thanks to smart procedures as pilot/training symbols or subcarriers, continuously tracking the evolution of the time-variant radio channel, due to the mobility of terminals. In fact, in so-defined 'closed loop' set-up the RX can estimate the CSI and feed them back to TX. In case of high mobility of the users the risk to have out-of-date CSI at TX is not zero. Differently, in the so-defined 'open loop' set-up the CSI are estimated separately using uplink (UL) and downlink (DL) control signals of the network.

The impact of the quality of CSI estimation may lead to sub-optimal results with respect to initial MIMO theoretical results. So, this represents one of the technical limitation of MIMO technology, demonstrated by the trade-off between speed and overhead introduced by sharing the CSI among TX-RX.

6.1.4 MIMO Space-Time Codes

Examples of implementation of MIMO Diversity are the so called Space-Time codes, Gesbert [179], Oestges [180]. These codes exploit the additional spatial domain with respect to time and frequency, by managing the antenna array elements to increase the robustness of the signal, (similarly to usual channel coding Forward-Error-Correction (FEC) codes (e.g. Turbo, LDPC)), with the goal to reduce the errors in the wireless link. Actual codes are named Space-Time-Block-Codes (STBC) or Space-Frequency-Block-Code (SFBC) with OFDM (e.g. currently implemented in LTE and Wi-Fi to perform up to 8x8 MIMO links).

6.1.5 MIMO Spatial Multiplexing

Moving on, besides diversity, the real 'magic' of MIMO is Spatial Multiplexing, allowing the possibility to increase the data rate with two key factors: proportionally to the number of antennas and avoiding to spend extra radio resource as bandwidth or power. The radio channel multipath is not considered as an impairment but rather exploited to send and receive more samples at once, without time or frequency division multiple access techniques. Spatial Multiplexing MIMO communications can be imagined as parallel 'spatial' flows, called also streams or layers, of single-antenna data.

In order to understand the MIMO Spatial Multiplexing, it is important to explain what is the Rayleigh fading, being one of the fundamental assumption in literature: the magnitude of the overall received signal is assumed to vary according to Rayleigh distribution, due to the sum of 'infinite' number of independent paths (i.e. i.i.d.), with approximately equal amplitude and random phase. This is true for heavily built-up urban environments, as New York for example, or any strong NLOS scenario. Considering to have omnidirectional antennas, the Rayleigh fading is then used to model the multipath onto a given antenna element, Proakis [37]. This is true for LTE bands for example, but different for Above-6GHz bands with directive antennas.

Then, given a rich multipath which "creates" Rayleigh fading and given the CSI perfectly known at both ends, all the assumption to reach the optimal results of Spatial Multiplexing are satisfied. Usually, the MIMO channel is indicated by a matrix called H which contains essentially the raw nature of the channel as a set of complex numbers named channel gains/coefficients. CSI are nothing else than an estimated version of this matrix H, as anticipated. In Eq.6.1 the well-known formula for MIMO channel capacity is expressed, Foschini-Telatar [169]. Besides the presence of the matrix H as argument of the logarithm, as novelty with respect to well-known capacity Shannon formula, ρ states for SNR ratio, N_T for the number of TX antennas involved in MIMO and I_{N_R} is the identity matrix proportional to N_T.

$$C = E_{\mathrm{H}}\left\{ \log_2\left[\det\left(\mathbf{I}_{\mathrm{N_R}} + \frac{\rho}{N_{\mathrm{T}}} \mathbf{H}\mathbf{H}^{\mathrm{H}} \right) \right] \right\}$$

Eq.6.1

An important parameter to evaluate the characteristics of the MIMO is the rank of this matrix H: in case of optimal configuration a full-rank matrix H means the possibility to exploit all the multipath whereas in the worst case a matrix H with rank equal to one makes Spatial Multiplexing falls back to Beamforming. In the last

case if one path (e.g. LOS path) is dominant, the Rayleigh fading become Rician and the radio channel does not 'support' anymore the multiple streams. Antennas play a significant role in this context, filtering spatially the multipath contributions, confirming again the divergence of Above-6GHz systems.

In a nutshell, with a MIMO 4x4 we can achieve a MIMO Gain in the data rate up to a factor equal to 4, ideally. The lesson to learn is to avoid considering the MIMO Gain as an common result in the real MIMO communications, rather than an upper bound result. Since MIMO performance are dependent on the radio channel, so the MIMO Gain itself is a 'random' scenario-dependent improvement, roughly speaking. This why in Eq.6.1 the capacity formula includes an expectation operator E_H on the channel matrix H before the logarithm.

Practically, implementing Spatial Multiplexing is very demanding both for the costs of multiple RF chains and parallel signal processing. A straightforward way is the Singular Value Decomposition (SVD), where Eigenvalues of matrix H are extracted from CSI and directly used for combining samples in order to have parallel data streams, Paulraj [171].

6.1.6   Diversity and Multiplexing

It is possible to perform Diversity and Multiplexing at the same time, as reported by Tse [181]. The two 'faces' of MIMO are not exclusive and they can cooperate to enhance the reliability of the link with diversity, as well as FEC, and also to speed up the link data rate with Spatial Multiplexing, as well as high order MCS.

For example with 4x2, two TX antennas can host pre-coded samples for Spatial Multiplexing and the other TX antennas can work for diversity, complementary. The RX with 2 antennas will then decode the correct samples from two MIMO streams, with a lower BER with respect to 2x2 MIMO only. Examples are given by well-known STC or STFC codes, Bolcskei [182], called BLAST code, invented at Bell Labs, as reported by Foschini [165].

Finally, again similarly to MCS and FEC, MIMO can be naturally considered as a special feature of PHY layer, to efficiently cope with the unpredictable radio channel, meaning that the MIMO configuration is changed adaptively in time or in frequency according to the variability of the radio channel. For example with low SNR perhaps is better to use Diversity to save the BER and with high SNR is better to use Spatial Multiplexing to push the data rate. In LTE MIMO is implemented in several 'modes' which comprise: closed and open loop CSI, Beamforming, SVD Spatial Multiplexing, STFBC for Diversity. For example a default Codebook of matrices H is stored in memory to facilitate the CSI estimation.

6.1.7   Multi-User MIMO

Enlarging the Single-User (SU) MIMO solutions to the case of Multi-Users (MU) is very challenging because the RX terminals are physically separated far away and they cannot collaborate. Moreover, the complexity of the problem can really dramatically increase since each RX can itself have multiple antennas.

Anyway, let's imagine to have a sample for user 1 and a sample for user 2. Sending both signals onto the two TX (AP) antennas at the same time, users will receive both samples overlapped. Now, using the concept of Spatial Multiplexing scheme but picking sample 1 and 2 rather than two consecutive samples of the same data stream (i.e. Multi-User MIMO), the pre-coded sample 1 and sample 2, with their

proper CSI, are part of two parallel independent streams intended for two physically separated RX. In the end, the data rate is not doubled but two users are served at the same time, Spencer [183]. A well-known MU-MIMO technique is named Zero Forcing Beamforming (Yoo [184]) which is capable to pre-code signals such that each RX receives its sample and does not suffer from any mutual interference.

For example, in the IEEE 802.11ac up to 8 simultaneous streams are comprised in the standard. In fact, in Fig.6.2 a graphical representation of the ZF MU-MIMO is given for 3 users with different colors. The 3 2D qualitative antenna patterns are sketched with different colors, remarking the allocation of maxima and nulls points towards the users.
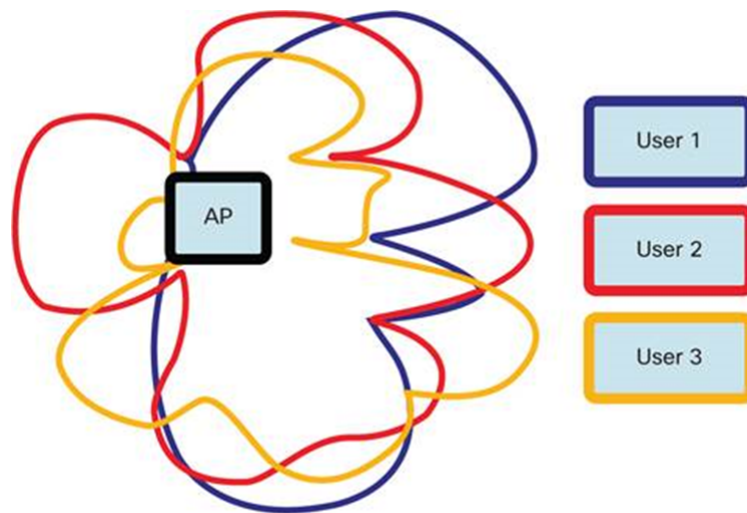
FIGURE 6.2: MU-MIMO Zero Forcing concept.

Besides the example in Fig.6.2 related to the downlink case, called in literature Broadcast channel problem (Caire [185]), on the other hand, there is also the uplink problem, named Multiple Access problem: the users send data all together to the TX, which is asked to 'decouple' the superposition of the received signals using Multi User Detection / Decoding, being aware of the different CSI. These MU-MIMO schemes are still under evaluation facing complexity and HW limitations.

6.1.8 Massive MIMO

As rule of thumb, the bigger the number of antennas the better the possible benefits of MIMO schemes. The concept of Massive MIMO is achieved using a larger number of elements in the antenna array, in theory, asymptotically towards infinite, Lu [186], He [187]. This novel idea is one of the most challenging issue in MIMO, very promising for new Base Station architectures for example, involving many problems about the huge complexity and the feasible implementation, as reported by Rusek [188] and Larsson [33]. Today only a few promising prototypes as proof-of-concept are available: the 128x12 massive MIMO by University of Bristol and 100 elements MIMO by Lund University.

A very noticeable effects of massive MIMO is the Channel Hardening: the H matrix of MIMO communication channel is a random variable which varies in amplitude and in phase due shadowing and fading. With massive MIMO the H part related to small-scale fading is reduced thanks to the large size of the array, so making the realizations of the matrix H closer to its expected value (e.g. H fluctuations

are small with respect to its average). With an independent Rayleigh fading channel, the variance of the ratio between H and its expected value reduces with the inverse of the number of antennas. Even though the CSI must be estimated for all the numerous antenna elements, the CSI values are now, approximately, scalar numbers. Then using a wise ratio between pilots data and useful data the radio channel can be considered less disperse, (that is why hardening) and easier to be treated. The performance of massive MIMO reach bps-per-Hz up to 50 with 100-200 antennas, in theory. Nevertheless, the implications of massive MIMO for future systems are still to be fully assessed, Swindlehurst [189], Mumtaz [190], especially from an HW point of view, as discussed in Appendix.

6.2   Beamforming

6.2.1   BF introduction

Differently from MIMO, Beamforming and Beamsteering are combining technique to pilot antenna radiating elements in order to change the shape and directionality of the overall antenna radiation pattern. Historically radar, aerospace and surveillance have been the first main applications (Godara [191]), where generally the goal is to scan the environment spatially with repeated sweeps to identify known or unknown targets. In the last decades multi-antenna BF are relatively new in wireless communications, especially Above-6GHz, as discussed in chapter (7). The principal properties of BF systems are: the antenna topology (e.g. linear, planar or volumetric), the single radiating element (e.g. isotropic, dipole, patch), the elements spacing distance (e.g. uniform or non uniform), the operating frequency (e.g. narrowband or wideband, with carrier or pulses) and, in the end, the different hardware.

6.2.2   BF architectures

An example of planar patch antenna array at 30GHz is given in Fig.6.3 with 64 elements on an area of 60mm x 60mm, (Samsung [18]), compared to a 3GHz standard patch antenna. It is clear the huge difference in the antenna design moving from 3 to 30GHz.
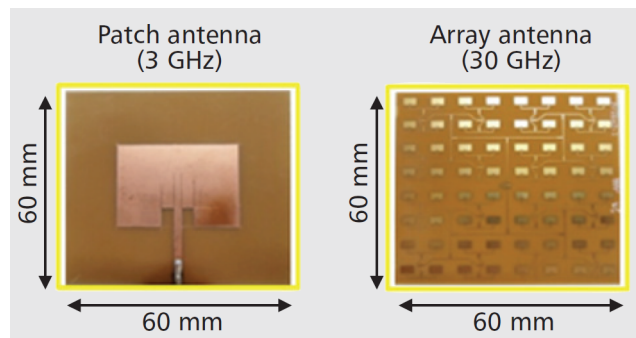
FIGURE 6.3: Comparison between 3 GHz antenna and 30GHz array
with same antenna area. (Samsung [18])

The BF circuits which control each port of the antenna array can be implemented at Intermediate Frequency (IF) or at Carrier Frequency (RF), (see Appendix). The goal is to create a desired pattern of constructive and destructive interference in the wavefront, typically in the far field, towards a given direction in the space. This

direction is called "look" direction indicated by a pair of coordinates as (θ,ϕ) and simply represents the spot where to focus the radiated energy (at TX side). From an hardware point of view, Fig.6.4 shows an example of Beamforming network with parallel RF modules (named also sub-array) linked together by data and control buses, to form the complete antenna array BF system.
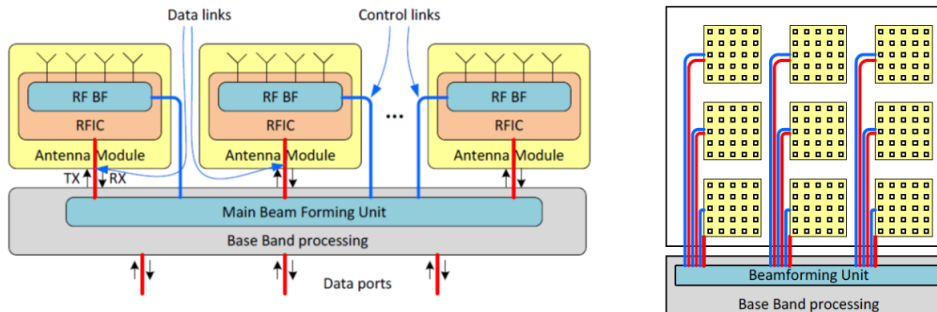
FIGURE 6.4: Beamforming processing unit with sub-arrays.

In details, the principle of BF is based on the computation and application of a set (i.e. vectors with linear arrays, matrices with planar arrays) of pre-calculated coefficient, called BF weights (or also Steering Vectors) which modify properly the phase (and eventually also the amplitude) of the signals flowing towards the antenna elements, in order to arbitrarily pilot the antenna pattern (at TX side). It is fundamental to remind that in order to properly work a Beamforming system needs to know the direction towards which or from which performing the beam-forming (e.g. look-direction).

6.2.3 BF processing

Considering now a real LOS scenario, where the total received e.m. field includes interference, noise and useful signals. The BF problem at RX side is generally an optimization problem on the SINR itself. This means practically 'synthesizing' with combining weights a pattern with maxima beams towards the transmitter and null beams towards interference sources, as reported by Van Trees [192], in order to boost the useful signals and filter out the unwanted signals, before the ADC sections and the digital elaboration. The same concept can be applied at TX side, equivalently to MU-MIMO as shown in Fig.6.2.

The following Fig.6.5 provides a scheme of adaptive BF scheme at RX side, where BF weights can be flexibly changed accordingly to the collected signals from the antennas (i.e. Induced Signals in Fig.6.5) and the achieved SINR (i.e. Array Output in Fig.6.5), thanks to the feedback loop.
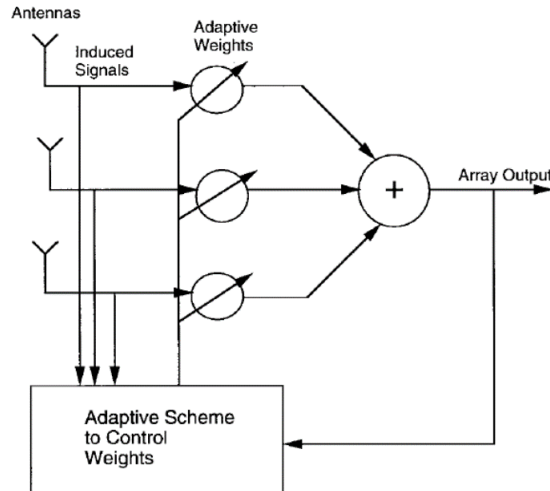
FIGURE 6.5: Adaptive BF receiving scheme.

6.2.4 Beamforming vs MIMO?

Nowadays one of the great challenge for Above-6GHz systems is represented by the question which multi-antenna technique is more suitable: MIMO or Beamforming?. It is still an open issue, but considering that Beamforming aims mainly at improving SINR, while MIMO is more flexible and can even increasing directly the data rate, then it is clear that they can play a complementary role, Sun [193]. However, considering short-range LOS links, in the end, the emerging trend today is to consider Beamforming as the key primary multiple-antenna technology, rather than the "classical" MIMO used for Below-6GHz, at least in the short-medium run. This motivates the focus on indoor BF in following chapter (7).

6.3 BF protocols and advanced issues

In order to implement efficient BF solutions, besides antennas and HW features (see Appendix), it is moreover essential to take into account BF procedures or algorithms: these signalling 'protocols' describe how TX/RX should use their BF capabilities searching for the best combination of directional beams in order to establish a robust communication. The BF procedure adopted for a given application depends on the radio channel characteristics, but especially, on the availability of knowledge about the locations of other terminals, as well as CSI for MIMO, as previously discussed. In a nutshell, this means that TX must know where to focus power and RX must know where to orient the antenna pattern to collect power. Of course this problem is still an open issue due to terminals mobility and demanding NLOS scenario applications, especially Above-6GHz.

To cope with this issue, at receiver side it is possible to implement classical AoA estimation methods (e.g. well-known algorithms like MVDR, MUSIC, ESPRIT, Godara [191]), which estimate the AoA by identifying the local maxima of the spectrum of the received signal. In addition, sub-space based methods, also termed as super-resolution methods, aim at separating the observation space in a signal subspace, containing only useful information, and its orthogonal complement, called noise subspace. This decomposition results in robust spectral analysis, and improves the

spectral resolution significantly, thus delivering high angular resolution of the arriving signal direction. However, these methods are characterized by high computational complexity.

On the other hand, since Global Navigation Satellite Systems (GNSS), (e.g. GPS, Galileo or Glonass), are not capable to provide localization in indoor or partially shaded places, there is a lack of a wide-spread technology for Indoor Positioning and Tracking. A lot of different technologies are available as Bluetooth (e.g. iBeacon), UWB, Radio-frequency identification (RFID), Wi-Fi, Geomagnetic Fingerprinting, Image Processing, Visible Light Communications (VLC), ultrasound waves and even infrared light, Zafari [194], Yassin [195], Brena [196]. Particularly within the IEEE 802.11, a new standard called Next Generation Positioning (NGP) or 802.11az could remarkably be a valid solution starting from 2019, [197]. Also, the ongoing development of 5G can integrate localization technologies, as recently outlined by Koivito [198].

For sake of generality, it is worth saying that Beam protocols are still an open problem also in the MAC layer because traditional protocols, as the well-known Carrier-sense multiple access (CSMA), typically fail to exploit the potential benefits of BF multi-antenna system, being designed originally to deal with omnidirectional antennas, as reported by Bazan [199].

6.3.1 Beam Search and Tracking

Beam Search means applying a BF protocol to guide TX/RX to find suitable beams combinations with none/partial/complete knowledge of the their positions. Beam Tracking is secondly necessary to make the terminals adaptively update their BF settings (e.g. Steering Vectors), Palacios [200].

In Fig.6.6 is shown an example of mmWaves radio access in 5G network, where BF procedures named Beam Sweeping (e.g. Search) and Beam Refinement (e.g. Tracking) are essential to set up a link between a Small cells and a UE, due to the directive antennas. Considering that the RR pool in the deployment comprises BF beams to be searched and allocated for every user, it becomes essential at network layer the usage of efficient and fast BF protocols to keep the complexity of BF management as low as possible.
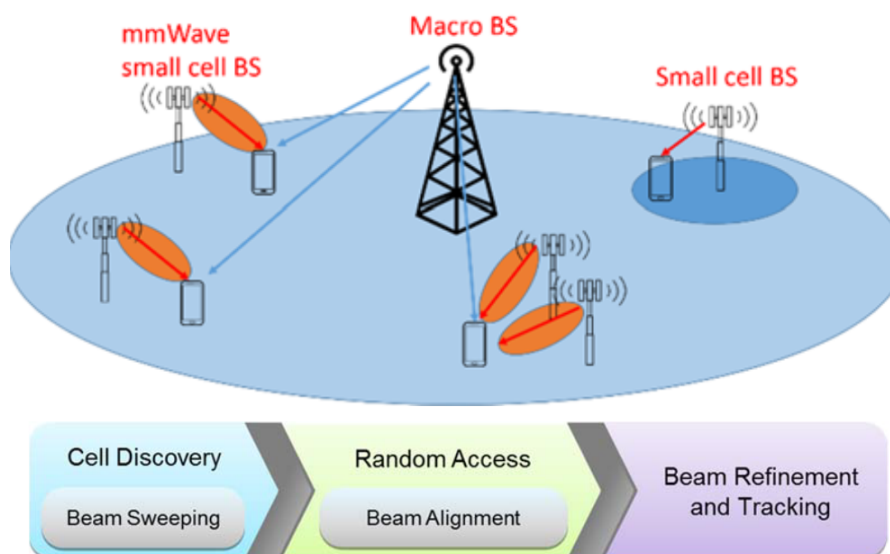

FIGURE 6.6: 5G deployment example with BF links.

Particularly in indoor scenario, the Beam Search is mostly assessed assuming no information about the devices locations, since no GNSS services are available. Within this framework, popular BF protocols adopted so far are named "blind" (Nitsche [201]), because TX/RX must perform an Exhaustive Search to test all the beams combinations, differently from MIMO schemes, where CSI data can be retrieved sounding the channel trading-off between overhead and accuracy. Of course, the price to pay is the time-consuming overhead introduced by this "trial-and-error" BF Search protocol.

Indoor millimeter wave standards as IEEE 802.15.3c and IEEE 802.11ad (Rappaport [15]) use a Codebook-based beam switching technique to speed up the link set-up. Fig.6.7 shows the 802.11ad BF terminology to explain how the spatial domain is "sectorized" for BF switching: Q-omni means quasi-omnidirectional pattern and HR Beam means High-Resolution Beams. In a nutshell, a set of orthogonal patterns, corresponding to a set of orthogonal BF weights, are collected in a Codebook and used efficiently to scan sequentially the communication space, Singh [202].
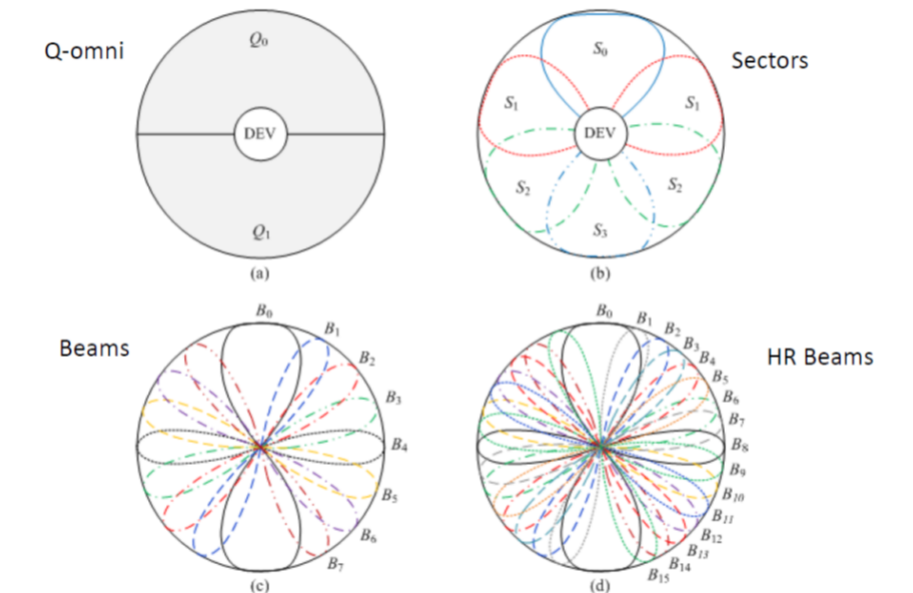
FIGURE 6.7: BF Switching beams terminology.

For example, the IEEE 802.11ad specifies a BF search protocol in three phases (Fig.6.8):

- Sector Level Sweep (SLS): the SLS phase is a coarse procedure where the transmit and receive antennas use quasi-omnidirectional patterns to select the best transmit and optionally receive antenna sector.

- Beam Refinement Phase (BRP): once the best sector pair is identified, the beam refinement phase trains the transmit and receive antenna arrays to select a beam pattern pair with finer beamwidths.

- Beam Tracking (BT): the optional beam tracking phase is employed during data transmission to adjust for channel changes.
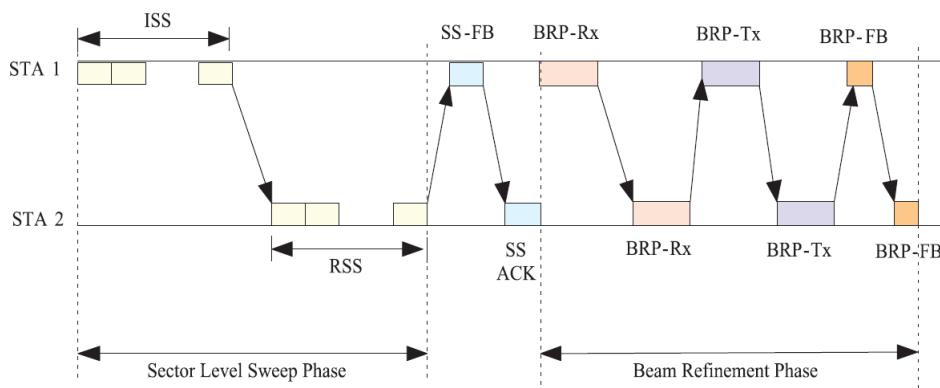
FIGURE 6.8: 802.11ad BF protocol.

The training packets are transmitted using the low power low rate MCS (e.g. control PHY mode) ensuring reliable communication required to establish the initial link. However, the set-up is not free from well-known Hidden or Exposed Node problem, [199]. The station (STA) that trigger the BF training is called the initiator, and the recipient is the responder. The SLS involves initiator sector sweep (ISS), responder sector sweep (RSS), sector sweep feedback (SS-FB), and sector sweep acknowledgment (SS-ACK). During SLS phase, the transmitter sends training packets from pre-defined sectors. The receiving antenna remains in an omnidirectional mode and after measuring the signal strength (e.g. SNR) across all sectors, it provides the sector sweep feedback to the transmitter, indicating the sector with maximum received signal strength. BRP iteratively trains the transmitter and receiver sides to refine the beams found during the SLS. BRP includes setup, the optional multiple sector ID (MID) detection (Prasad [203]) and beam combining (BC) sub-phases. A set of fine (high resolution) pairs with fair link qualities, inside and within the proximity of the best sector identified during the SLS phase, are tested during the BRP. The MID sub-phase could be optionally incorporated to perform receive side training. The BC sub-phase is used to limit the number of refined beams to be tested during BRP with an objective to reduce delay. After completion of the SLS and BRP phases, the best refined beam pair is used for transmission. However, this link is susceptible to variations in channel conditions. The BT phase uses training sequences which are appended to payload data packets for channel estimation, to adjust for channel variations in the aftermath of SLS phase and BRP.

So, the whole multi-stage procedure of BF Search and Tracking should be run on demand or pro-actively depending on the possible propagation scenario and network topology, aiming at the minimum computational effort (e.g. overhead) due to the stringent time constraints in setting up multi-Gbps communication links. As reported by Kutty [204], considering antennas with 64 elements, 4 sectors and 128 beams, the number of steps involved in the 802.11ad protocol is equal to 561 only, with respect to 16384 steps needed for the entire "brute-force" exhaustive search. It is worth reminding that Beam Search protocols can be too slow when beams are very narrow, and might fail to promptly react upon fast channel changes, e.g. due to abrupt human blockage or terminal movement. Regardless the specific implementation, codebook-BF switching protocols can be expected to perform well in static condition, where it should run just once at radio link set up. On the contrary, some doubts may arise about its effectiveness in a time variant channel or when many users are served by the same BS or AP, requesting access to the channel randomly in time. For instance, in large and crowded scenarios where moving people or other

moving objects may suddenly block paths, thus triggering a new Beam Search. In presence of frequent and unpredictable blocking occurrence, the tracking algorithm should be run over and over again, to the detriment of the overall system performance.

Chapter 7

mmWaves Beamforming

7.1 A Study on mmWaves Multi-User indoor Beamforming based on Measurements and Ray Tracing

7.1.1 Introduction

Time variant or multi-user scenarios still represent open issues concerning adaptive BF strategies, Kountouris [205], Jun [206], Hu [207]. In fact, existing BF protocols are likely to be impractical when a large number of (mobile) users must be taken into account. Further investigations on multi-user BF (MU-BF) seem therefore still necessary before international standardization bodies and institutions come up with robust and well-performing MU-BF algorithms. From a wireless propagation perspective, this entails the need for a deeper insight into the directional characteristics of the mmWaves channel, especially for MU-BF performance.

Such problems are addressed here through 3D directional channel measurement carried out in a small office environment in the 70 GHz band and Ray Tracing (RT) simulations. In particular, measured and simulated SINR distributions are computed and compared for different number of active users (N_{AU}) and for three BF strategies, ranging from a basic solution where the antennas are simply oriented along the transmitter (TX) - receiver (RX) direction, to a cooperative policy where an exhaustive search for the best SINR determines antennas steering. Both BF at TX side-only and joint bi-directional BF (i.e. applied to TX and RX) are considered.

Finally, "RT-assisted MU-BF" is also explored as a way to use RT prediction not only to assess benefits and drawbacks of different BF strategies, but also to contribute to drive the beam-searching process therefore speeding-up the time-consuming CSI estimation procedure.

For the sake of generality and simplicity, specific antenna-array topologies are not considered. Rather, the directive antenna pattern of the circular horn antenna used for the measurements is chosen as the reference pattern, and its main lobe is simply, pointed toward different directions to simulate different beam-steering solutions, without changing the radiation pattern. Since antennas HPBW is equal to 15°, it approximately corresponds to a broad-side array of few hundreds of isotropic elements, but of course the effect of side lobes (e.g. Beam Squint) and of polarization degradation of real arrays is not considered.

7.1.2 Concept and scope of the work

Multiuser indoor beamforming is investigated through a double-track, simulated / experimental approach following the general scheme sketched in Fig.7.1. The directional properties of propagation at 70GHz have been first explored by means of measurements carried out with the channel sounder (CS) already described in chapter

(5) and then with 3D RT predictions. The measured / simulated Power Angle Profiles (PAP) provided by the directional channel estimation are exploited to perform MU-BF system-level simulations based on multiple user-positions in the considered office scenario where beam steering is enforced using three different strategies: Radial, Best-S and Best-SINR schemes, as described later on. The considered BF strategies are compared for different number of users in terms of overall SINR statistical distributions.

In the measurement track (on the left in Figure) the beam-steering decision algorithm makes use of the measured channel PAP for the beam-searching phase and the SINR performance statistics are also derived from the measured channel. In the simulation track (on the right in Figure) the beam-steering decision algorithm makes use of a RT-simulated channel PAP, and the SINR statistics are also derived from the RT-simulated channel. By comparing the measurement- and the simulation-track performance, RT can be regarded as a suitable propagation model for BF system simulation (BF simulation validation). This is different from assessing RT as a propagation prediction tool (e.g. propagation validation). Furthermore, a mixed solution is also considered (box at the bottom, center of Figure), where beam steering is driven - at least partly - by the RT prediction but the SINRs performance statistics are computed using the measured PAPs, since the measured data are the closest information with respect to reality. This case corresponds to studying a so-called RT-assisted BF technique, where the system partly or totally skips the beam-searching phase and relies on embedded RT-prediction to find the optimum beam steering solution for each users location configuration.
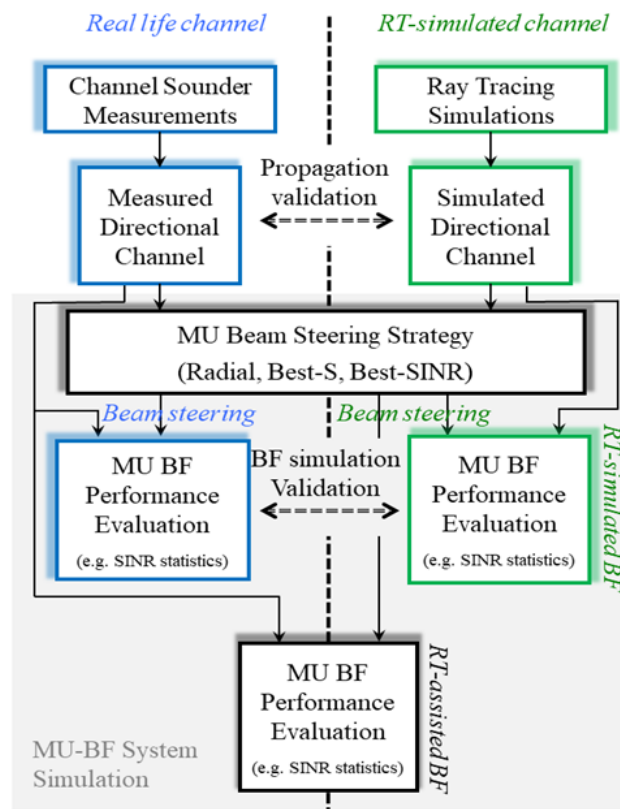

FIGURE 7.1: Logical block scheme describing the adopted methodology for the analysis and assessment of MU-BF capabilities.

7.1.3 mmWaves Channel measurement

The measurement scenario is the same scenario already seen in chapter (5) with
small changes: 6 receiver (RX) and 2 transmitter (TX) positions are included, and
now, as sketched in Fig.7.2, respectively, TX1 sweeps along [-75°, 75°] of elevation
and [-15°, 75°] of azimuth, TX2 sweeps along [-75°, 75°] of elevation and [-75°, 75°]
of azimuth (AOD) and RX sweeps along [0°, 360°] of azimuth (AOA), with 15°of res-
olution. CS measured data are stored as complex Channel Impulse Response (CIR)
and collected for every RX over a discrete predefined set of BF directions. Although
the angle step has been chosen exactly equal to the antennas HPBW (15°) to avoid
overlapping, the BF beams cannot be considered orthogonal. Finally, measured data
are collected for every pair of TX/RX pointing directions. The 6 different RX posi-
tions have been measured one by one sequentially using a wheeled mobile cabinet
supporting the CS RX unit and all the data have been gathered to create the multi
user data set.
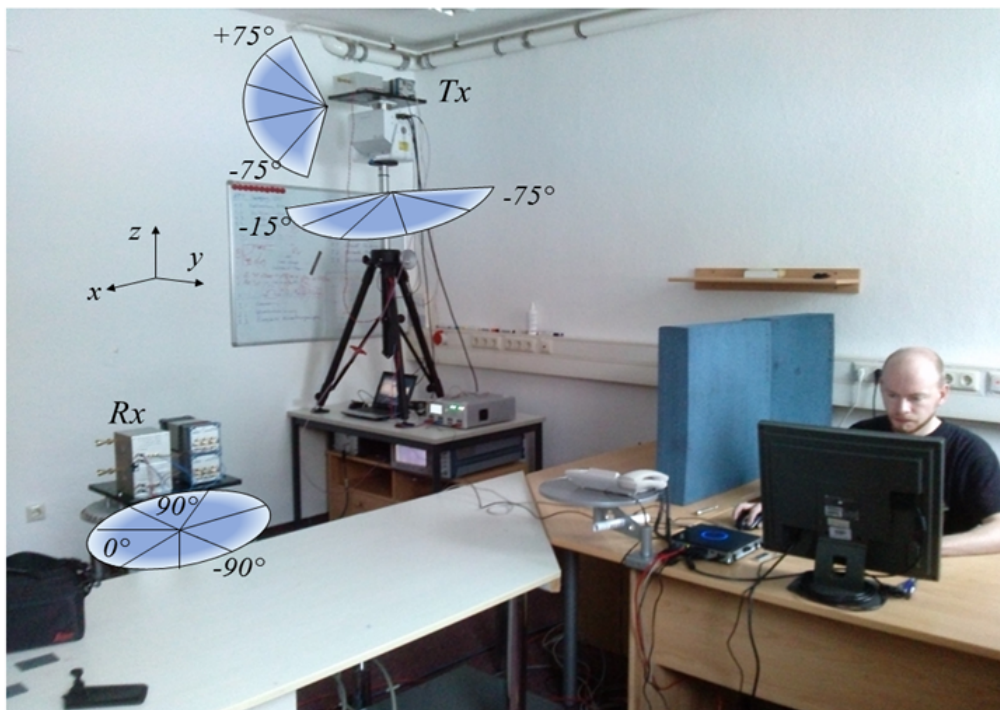
FIGURE 7.2: Picture of the room with overlaid measurement set-up
for Tx1 and Rx1.

According to the set-up, the number of possible BF choices is given by the dis-
crete set of pointing directions, equal to 11x11 AOD for TX2 and 11x5 AOD for TX1,
and 24 AOA for any RX. We focus mostly on results with synthetized omnidirec-
tional RX, i.e. the power received over the 24 RX angular slots is summed up to form
an omnidirectional azimuthal diagram. In practice, this means that BF is performed
only at TX side, and it is named "mono-directional BF" (or "mono-BF") in the fol-
lowing. This is a reasonable assumption considering the capabilities of today access
points, with respect to those of mobile or tablet devices. In case the RX antenna di-
rectivity has also to be considered, the beam search procedure must be performed
over both the TX and the RX, at the same time. This case is named "bidirectional-
BF" (or "bi-BF") in the following. Practically speaking, the BF with mono-BF is less
expensive, faster and easier to implement with respect to the bi-BF.

7.1.4   BF System simulation

System-level simulations take into account exhaustively all the possible configurations of the N_{AU} active users (AU) in the small-office environment, i.e. a sequence of different "drops" is considered. Each drop considers a different arrangement of the N_{AU} RXs over n possible locations, where n=6. The overall number of combination of course amounts to the binomial coefficient n over N_{AU}. After that, the best set of beam orientations (i.e. the best BF solution) is then selected according to different criteria as described in the following section.

7.1.5   SDMA BF Schemes

For each RX location drop, a Beam Search is performed all over the angular discrete set to achieve the best BF solution, i.e. the best set of N_{AU} beams, according to 3 different techniques:

- Radial BF method: a non-cooperative solution where the antennas radiation lobes are simply steered towards the TX-RX direction for each active link. This scheme is clearly very simple but requires an indoor localization technology. Clearly, Beam Search is actually not necessary in this case, since the antennas steering just depends on their positions, without any need for the spatial scanning.

- Best-S BF method: the beam search is based on the received power (S) level, regardless of interference. Practically, a feasible solution can exploit an uplink channel state information (CSI) feedback to inform the TX about the received power from all AU. An "oracle-based" solution is considered for the sake of simplicity for all the MU-BF simulations, meaning that the CSI is assumed known on the base of measurements or RT simulations.

- Best-SINR BF method: is an interference-aware, cooperative beam-search solution based on the ratio between received power (S) and interference levels (I). In this case, the price to pay is a more challenging CSI estimation, which may lead to large overhead or time consuming signaling. An "oracle-based" solution is considered also here for the sake of simplicity.

In summary, in the simulations an exhaustive beams optimization is repeated for all possible RX location drops and all the possible beam orientations, in order to identify the best set of the N_{AU} beams for each of the proposed techniques.

7.1.6   Beam Search Optimization

In a MU scenario, a high aggregate throughput represents a major goal for an effective BF technique. At the same time, unbalanced SINR distributions should be also avoided, in view of a "fairness principle" that should be granted to the active users. For example, a BF solution generating similar SINR levels should be preferred to another with the same average SINR but different (unbalanced) SINR levels for the different users. Therefore, the best BF solution should be selected so that the SINR values experimented by the different N_{AU} users are as high as possible, and also as balanced as possible. In order to accomplish this target, the Beam Search Optimization method proposed here aims at finding the BF solution - i.e. the best set of N_{AU} beam steering directions, indicated with $\overline{\psi}$ which maximizes the metric ρ_ψ , as

defined below. In fact, referring to the mono-BF case for the sake of simplicity, this concept can be expressed in formulas as:

$$\overline{\psi} = \arg\left\{ \max_{\psi \in \Psi} \left(\rho_\psi \right) \right\}$$

$$\rho_\psi = \left\langle SINR \right\rangle_\psi - \left(\sigma_{SINR} \right)_\psi$$

Eq. 7.1.

where the best BF solution $\overline{\psi}$ is selected among the set Ψ which is the collection of all the possible N_{AU}-ples of beam steering angles: for example, considering the TX2 location of the measurements with mono-BF, the searching domain Ψ is formed by the $(11x11)^{N_{AU}}$ possible cases, and the best solution $\overline{\psi}$ is selected among them so that the parameter ρ_ψ is maximized. In Eq.7.2, average SINR and SINR standard deviation are computed as:

$$\begin{cases} \left\langle SINR \right\rangle_\psi = \sum_{i=1}^{N_{AU}} \dfrac{SINR_\psi\big|_i}{N_{AU}} \\ \left(\sigma_{SINR} \right)_\psi = \sqrt{\sum_{i=1}^{N_{AU}} \dfrac{\left(SINR_\psi\big|_i - \left\langle SINR \right\rangle_\psi \right)^2}{N_{AU}}} \end{cases}$$

Eq. 7.2.

where $SINR_\psi$ is defined as the ratio between the useful signal (S) and the interference from the signals steered towards the remaining N_{AU} -1 users (plus noise), for the considered solution. This procedure is repeated for each RX drop. The same optimization equations hold for Best-S method, simply substituting the SINR values with the S values. Due to memory limitations, a maximum of 4 AU has been considered for the mono-BF case, and of 2 AU for the bi-BF case.

7.1.7 Case Study

In order to investigate the performances of beam Search Optimization schemes (Best-S, Best-SINR and RAD) for SDMA, a preliminary case study has been done, respectively for 2 (RX5 and RX6), 3 (RX3, RX5 and RX6) and 4 AU (RX2, RX3, RX5 and RX6), with omnidirectional radiation pattern at the RX side. For the case study is considered the TX2 located over the table in the middle of the office, as this position exhibits a wider angle allowing a higher degree of freedom in beam steering. The receivers taken into account for the case study are placed symmetrically with respect to the table in front of TX2.

In Fig.7.3, results of the BF procedure are graphically shown for the Best-SINR and Best-S schemes respectively, for N_{AU}=3, while in Fig.7.4 results are reported for N_{AU}=4. In Table 7.1 the corresponding values of SINR and AOD for each receiver are reported for the case of two, three and four AU.

In case of 3 AU Best-SINR scheme schedules RX6 and RX3 along LOS paths and RX5 towards a single-bounce reflection on the wall. This choice avoids possible

interference from RX3 onto RX6, steering the beams in directions that are as independent as possible, at the same time keeping both SINR levels above 6 dB (Table 7.1). On the other hand, neglecting the interference (Best-S scheme) results in very poor SINR at RX6 equal to -0.8 dB (Table 7.1), due to the negative contribution from RX3 NLOS path coming from the windows wall, when considering the strongest path (Best-S). By comparing the figures, it is clear that the strongest path for RX3 is not the LOS path, but the NLOS single bounce path. This behavior can be explained highlighting that TX2 and RX3, as all the considered receivers, are not at the same height: receivers are at lower height than the transmitter. Due to this link configuration the shape of the radiation diagram in the vertical plane, strongly affect the value of the received power.
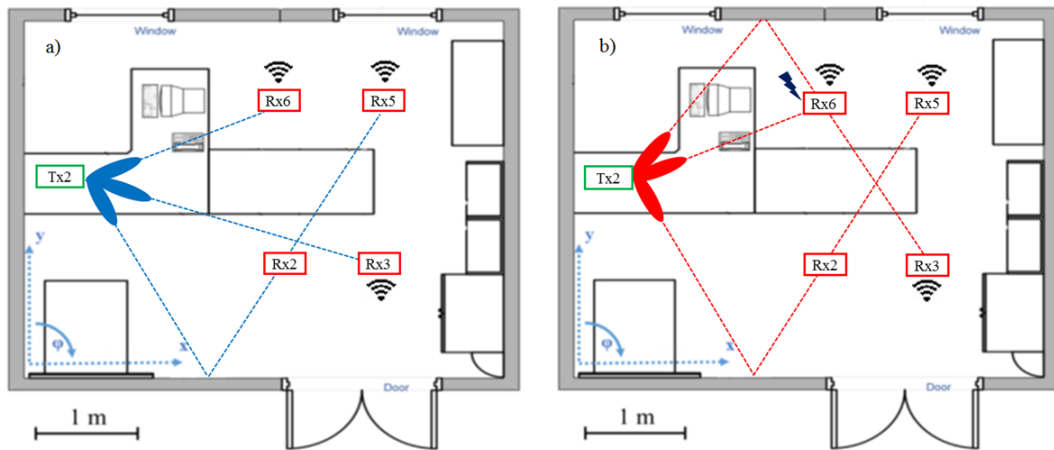
FIGURE 7.3: Rx6, Rx5 and Rx3 (3 AU) served by TX2 according to
Best-SINR (blue) and Best-S (red) BF method with mono-BF.
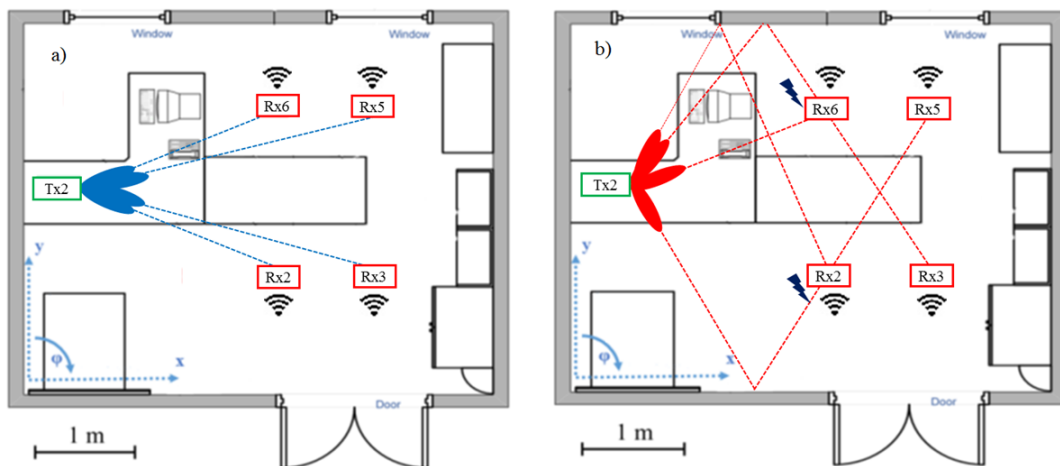
FIGURE 7.4: Rx6, Rx5, Rx3 and Rx2 (4 AU) served by TX2 according
to Best-SINR (blue) and Best-S (red) BF method with mono-BF.

When N_{AU}=4, the Best-SINR scheme (Fig.7.4) converges to adopt an SDMA solution equal to the RAD path for every receiver, so dividing efficiently the users in four distinct sectors, taking advantage of the room size. Conversely, Best-S scheme reaches a different configuration where both RX6 and RX2 are currently interfered

by the signals directed towards RX3 and RX5, respectively. Rx6 obtains a SINR level of -2.6 dB and RX2 of -1.3 dB. In this configuration, although the room multipath offers feasible NLOS chances for SDMA, the lack of control on interference may cause a significant drop in SINR performance, highlighting that indoor multipath plays a key role in the fundamental understanding of the BF procedure, especially when multiple users are involved.

N_{AU}	Rx id	SINR [dB]			AOD (az,el) [deg]		
		Best-SINR	Best-S	RAD	Best-SINR	Best-S	RAD
2	5	8.4	6.8	6.8	(60, -30)	(-15, -30)	(-15, -30)
	6	7.5	4.1	4.1	(-15, -45)	(-15, -45)	(-15, -45)
3	5	7.2	7.0	5.9	(60, -30)	(60, -30)	(-15, -30)
	6	6.3	-0.8	4.8	(-15, -45)	(-15, -45)	(-15, -45)
	3	6.8	4.4	6.7	(15, -30)	(-60, -30)	(15, -30)
4	5	6.7	4.8	6.7	(-15, -30)	(60, -30)	(-15, -30)
	6	5.2	-2.4	5.2	(-15, -45)	(-15, -45)	(-15, -45)
	3	8.1	3.9	8.1	(15, -30)	(-60, -30)	(15, -30)
	2	4.9	-1.3	4.9	(15, -45)	(-75, -30)	(15, -45)

Table 7.1: SINR and AOD values of the case study.

7.1.8 Results

After performing BF simulations based on double-directional channel measurements, all results were collected and SINR statistics (mean and standard deviation) over different RX positions realizations for different BF methods, as reported in Table 7.2. Best-SINR and RAD show the highest mean SINR, whereas Best-S has worse performance. Going from N_{AU}=2 to N_{AU}=4 with Omni RX, the mean SINR decreases by nearly 7dB due to higher interference. TX2 results are generally better because TX1, being the corner of the room, has half the field of view (FOV) over the environment than TX2 and therefore less headroom for BF to achieve a good space division. An interesting result is the lower standard deviation achieved by the optimized BF schemes (Best-S and Best-SINR) compared to the RAD, because the former schemes are designed to achieve fairness too. In particular, the standard deviation of Best-SINR is up to 5dB lower than RAD standard deviation for mono-directional-BF (mono-BF) and bidirectional-BF (bi-BF), respectively. Furthermore, including the realistic SINR data into Shannon channel-capacity formula on average 3 bps/Hz, 4 bps/Hz and 6 bps/Hz for N_{AU}=4, 3 and 2, respectively, are achieved by only using best-SINR mono-BF SDMA, without other division or coding schemes.

N_{AU}	BF Scheme		Avg. SINR		Std. Dev. of SINR	
			Tx1	Tx2	Tx1	Tx2
2	Best-SINR	Mono- BF	11	13	4	3
	-	Bi- BF	31	33	7	8
	Best-S	Mono- BF	5	8	6	5
	-	Bi- BF	16	17	11	10
	RAD	Mono- BF	10	14	6	7
	-	Bi- BF	24	27	12	13
3	Best-SINR		6	9	2	3
	Best-S		4	3	4	4
	RAD		5	10	6	7
4	Best-SINR		3	8	2	2
	Best-S		1	2	4	3
	RAD		4	7	6	4

Table 7.2: SINR statistics.

Fig.7.5 shows the Cumulative Distribution Functions of the SINR over all RX locations drops for the best-SINR case and Tx2. Solid curves are for 3AU SDMA and dashed lines for 4 AU SDMA. The RAD CDFs can achieve a SINR of 18dB and 24dB outperforming best-SINR but in a limited set of cases, due to the absence of control on SINR fairness. Therefore, especially for LOS and small environment, a complex beam search algorithm could be a waste of resources and accurate localization information might be enough to achieve good results.
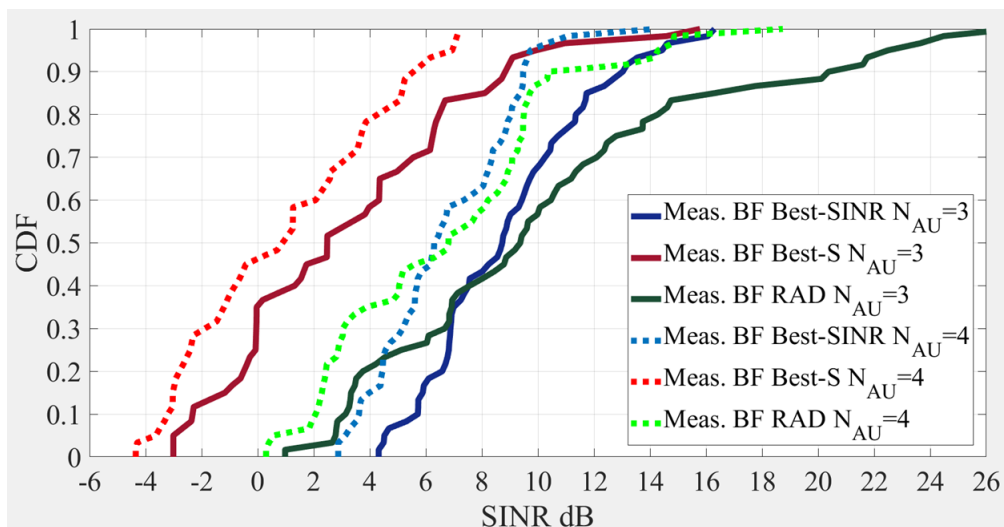

FIGURE 7.5: Comparison of SINR CDFs for different beamforming schemes (TX2, mono-BF).

In Fig. 7.6, the comparison of mono-BF and bi-BF SINR CDFs is shown for TX2 with 2AUs. Bi-BF attains a SINR gain of about 15dB with respect to mono-BF thanks

to the combined space-selectivity of the directive beams at both TX and RX. Basically, by performing BF at both link-ends, best-SINR can benefit from a huge number of degrees of freedom ($(11x11x24)^2$ beam-steering combinations) to achieve low-interference links. Of course, further investigations are necessary to confirm this conclusion for different scenarios such as large, crowded or dynamic environments.
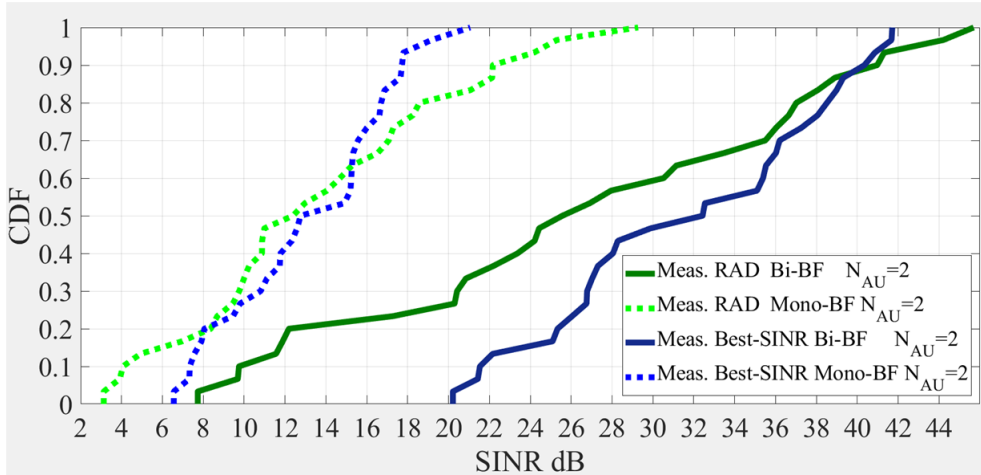

FIGURE 7.6: Comparison of mono-directional and bi-directional beamforming SINR CDFs (TX2).

7.1.9   BF performance based on channel Ray Tracing simulation

Beamforming simulations have been consistently repeated based on the RT-simulated double-directional channel. Results are shown in Fig.7.7 where the RT-based SINR CDFs (dotted lines) are shown to match quite well the measurement-based SINR CDFs (solid lines) for 2, 3 and even 4 AU.

As shown in Table 7.3, the root-mean-square-error (RMSE) of the RT-based BF simulations SINR with respect to measurement-based BF simulations is about 3dB. By increasing the number of AUs the RMSE raises slightly by 1-2dB. Regardless of the considered BF scheme, the RMSE is always kept below 5dB and this confirms that RT represents a valid multidimensional radio channel model and therefore a reliable tool to test advanced beamforming or MIMO schemes that exploit multidimensional propagation characteristics.

However, by computing AOD pointing errors between measurement-based and RT-based BF directions for the reference Best-SINR, mono-BF technique, we found a mean error of about 20°and a maximum standard deviation of 30°in Azimuth e 50°in Elevation, due to two reasons: the first is that the considered environment, even though in LOS, is a challenging scenario for SDMA technique, and therefore, even small deviations in the simulated directional channel can cause big changes in terms of SINR and also optimal steering direction; the second reason is that while the problem is well conditioned in terms of useful signal S (i.e. the S value for the optimum pointing found by RT-based BF is close to that found with measurement-based BF) this is not true for the interference I. Probably, the interference is highly dependent on secondary, multiple-bounce paths and secondary antenna pattern lobes which

are not accurately described in RT simulation. In particular, the RT antenna is described using 3D pattern reconstruction from 2D radiation patterns, and secondary off-axis lobes are subject to interpolation errors. Consequently the significant interference error directly generates a significant SINR errors, indeed. By computing RT-measurements errors separately for received power (S) and interference (I) at optimum pointing, we found a mean error of 2dB and a standard deviation of 2dB for the S but a mean error of 6dB and a standard deviation of 10dB for the I.
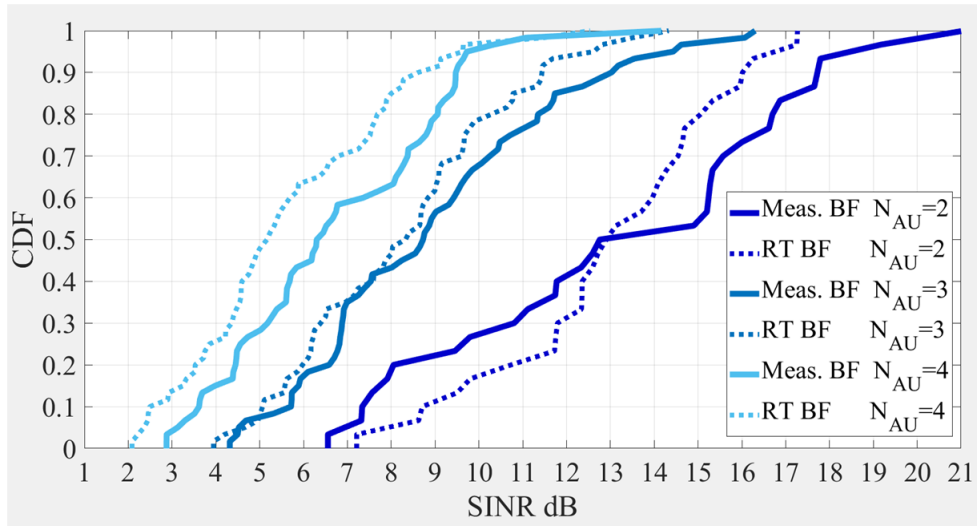
FIGURE 7.7: SINR CDF Comparison between measurements and simulations with 2AU, 3AU and 4AU with TX2 Mono-BF, Best-SINR method.

N_{AU}	BF Scheme		RMSE SINR Error	
			Tx1	Tx2
2	Best-SINR	Mono- BF	2	3
	-	Bi- BF	3	2
	Best-S	Mono- BF	2	3
	-	Bi- BF	3	3
	RAD	Mono- BF	2	2
	-	Bi- BF	4	2
3	Best-SINR		2	2
	Best-S		3	4
	RAD		3	4
4	Best-SINR		3	3
	Best-S		5	4
	RAD		3	4

Table 7.3: BF based on RT-simulation channel versus BF based on CS-measured channel: overall SINR RMSE.

Furthermore, to comprehend the complexity of the problem, it is worth noticing that SINR results (e.g. power values) are not strictly correlated to AOD results (e.g. angular values) due to the variability introduced by the multipath, meaning that an equivalent SINR level can be found using two completely different beam orientations since the number of beam-steering combinations is exponential with the number of users. This an interesting general fact not to be underrated in network optimization with BF-based radio access.

7.1.10 RT-driven and RT-assisted BF

The next step is represented by the concept of RT-driven / assisted BF, where RT is used for radio channel prediction to replace or assist the beam searching phase. Note that real-time RT prediction on today computing platforms in limited indoor environments can be performed probably faster than physical beam-search technique based on channel sounding and feed-back loop, also because only major, single- or double-bounce paths can be considered. Moreover, RT prediction can even be carried out off-line by dividing the environment into pixels, pre-computing double-directional channel information for ever couple of pixels representing possible terminal locations and storing the result into a look-up table. It is worth mentioning that RT-driven / assisted BF requires the knowledge of the TX/RX position to perform RT predictions within the system. The concept is evaluated for the Best-SINR mono-BF case, performing the following steps for each RX location drop:

the Best-SINR BF method is run based on the measured channel in order to identify within the set of all possible BF solutions Ψ, the optimum solution $\overline{\psi}$, i.e. the set of N_{AU} beams that achieve the best global performance metric ρ_ψ from equations 7.1 - 7.2 based on the measured channel:

$$\overline{\psi} = \left(\psi_1, \psi_2, ..., \psi_{N_{AU}}\right)$$

Eq.7.3

then, the parameter ρ is computed based on the RT-predicted channel for all possible beam-steering solutions (i.e. sets of N_{AU} beams chosen over the discrete angular set), and the ρ values are then sorted in descending order. The first solution in the "ranking" list is therefore the Best SINR BF solution based on RT, named $\overline{\phi}$, i.e. the solution that achieve the best ρ_ϕ based on the simulated channel.

$$\overline{\phi} = \left(\phi_1 ...... \phi_{N_{AU}}\right)$$

Eq. 7.4

RT-driven BF

Beamforming is assumed here to rely completely on RT to figure out the BF solution for each RX locations drop. To evaluate this technique, we compute ρ as performance metric, using the measured channel instead of the RT-simulated channel, named $\rho_\phi^{(M)}$: the subscript and the superscript indicate that the BF solution is found

using RT but the performance metric is evaluated using the measured channel, respectively. Then we compute the error as it follows:

$$E_\rho = \rho_\phi^{(M)} - \rho_\psi$$

Eq. 7.5

Such error indicates how much worse the RT-driven BF solution is with respect to the BF solutions that could be derived from the real (measured) channel. Looking at Table 7.4 (first two columns), unfortunately results are not very good, with a 50th percentile error of about 6dB and a 90th percentile equal or greater than 9dB in terms of ρ. Therefore by using RT to directly pilot BF it is possible to suffer from an average SINR degradation of about 6dB with respect to an exhaustive BF search based on the real channel, at least in a challenging small-indoor environment such as the one considered.

RT-assisted BF

This technique instead is based on two stages: first, RT is used to restrict the beam-searching angular set to a limited domain and then the actual beam-searching is performed over the restricted angular domain on the base of the measured channel. If the restricted angular domain contains the $\overline{\psi}$ solution then there is no performance degradation with respect to the exhaustive search, but beam-searching time is drastically reduced. During the first stage, for each RX drop, a BF solution subset is extracted from the RT-derived ranking list described before, by selecting all solutions with a ρ within a margin of 3dB of degradation with respect to ρ_ϕ. Then, Best SINR beam-searching is run over this restricted set of solutions based on the measured channel to single out the best one. Error statistics are derived in the same way as for RT-driven BF.

Results shown in Table 7.4 (last two columns) show that by doing so the error E_ρ is more than halved, with an error of about 3dB with respect to the exhaustive search, approximately. Moreover, considering that the restricted ranking list found during the first stage always includes less than 100 BF solutions, the overall search domain for the second stage is reduced by a factor of at least 150 and 17700 for N_{AU}=2 and N_{AU}=3, respectively, with a proportional dramatic reduction of beam-searching time. Even though this is a limited case of study, this solution is very promising.

All considered it can be concluded that, while double-direction RT prediction is not accurate enough to directly pilot beam-steering in a small indoor environment, it can still be an effective tool to help the BF algorithm to find the an effective solution in a short time.

N_{AU}	Tx	RT-driven BF		RT-assisted BF	
		50th percentile Eρ	90th percentile Eρ	50th percentile Eρ	90th percentile Eρ
2	Tx1	6 dB	14 dB	4 dB	6 dB
	Tx2	4 dB	9 dB	3 dB	5 dB
3	Tx1	6 dB	14 dB	3 dB	6 dB
	Tx2	6 dB	14 dB	4 dB	6 dB

Table 7.4: RT- driven / -assisted BF Error E_ρ statistics.

7.2 Ray-Tracing-Based mm-Wave Multi-Beam Beamforming Assessment

7.2.1 Introduction

Considering the reliability of good results provided by the Ray Tracing tool in chapter (4) for detailed Item-Level e.m. characterization and scattering tuning, in chapter (5) for double directional multi-dimensional radio channel evaluation and now for BF applications in indoor environment, a further study on advanced BF schemes is proposed in the following through only RT simulations.

Ray Tracing (RT) simulator is used to investigate RT-assisted BF techniques at 60GHz in terms of power-interference-ratio, (e.g. SINR distribution), in a reference indoor environment (7x10x3 meter), where different communications are assumed to be divided through space-division only (i.e. SDMA), [208], [209]. In particular, a novel Multi-Beam BF (MBF) technique is proposed where BF is simultaneously performed on the strongest paths in order to exploit the intrinsic space diversity of the multipath channel and improve robustness versus abrupt channel changes, as human blockage (HB).

7.2.2 Simulation scenario and set-up

The simulation environment is represented in Figure 7.8. It is an ideal indoor scenario, with a long corridor and two offices, furnished with wooden desks and metal cupboards (i.e. metallic cabinets). Internal walls which separate the offices are made of thin-plasterboard so that the signal can propagate into the offices, but the metal cupboards randomly placed against the walls create strong NLOS conditions in several spots, shadowing some areas. The AP (TX) is mounted on the ceiling in the corridor, whereas 24 RX locations per office are deployed on a grid, to sample the tested space regularly.

The transmitting antenna at AP is a 12x12 planar array of patch radiators with 20dB of Gain, transmitting an overall Equivalent Isotropically Radiated Power (EIRP) of 40dBm, compliant with the power limit fixed by the current international regulations as ETSI [210] and CEPT [211]. Omnidirectional antennas are considered at the RX, for sake of simplicity, letting only the TX to be able to perform BF.

In order to investigate the statistical properties of the Carrier to Interference plus Noise Ratio (CINR), one user RX per office has been considered, and an other RX interferer has been moved over all the remaining locations, as in Fig.7.9. Multiple realizations of the whole process are taken into account according to a static, snapshot

simulation approach. For sake of simplicity the CINR values have been obtained assuming the AWGN noise floor fixed to -100 dBm/Hz and considering only the power of the carrier at 60GHz. Simulations are carried out at only single-frequency 60GHz with no bandwidth.
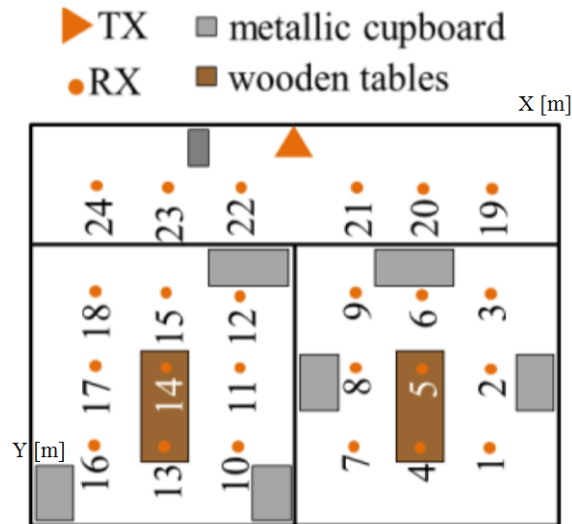

FIGURE 7.8: 2D map of the considered scenario for BF assessment.
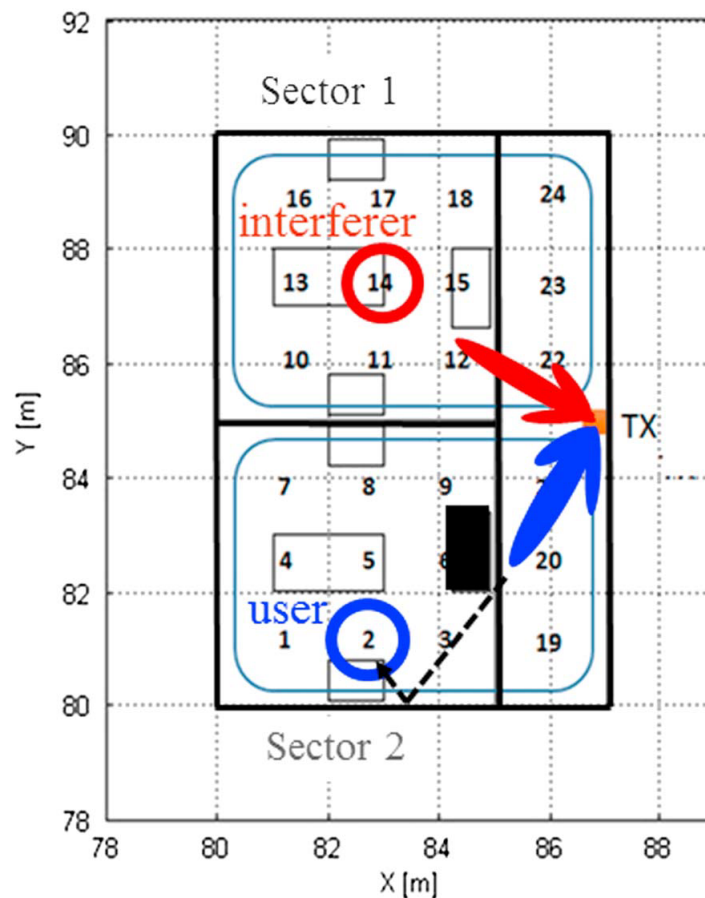

FIGURE 7.9: Graphical representation of user RX2 and interferer RX14.

7.2.3 Different BF Strategies

Three major BF solutions have been investigated, as well as in the previous study. The case of RX6 has been taken as example:

- Radial BF: assuming perfect indoor localization available for each (TX, RX) pair, a radiation pattern with a single beam steered towards the AOD of radial direction TX-RX (irrespective of the presence of possible obstruction) is considered at the TX array. In the following Fig.7.10 all the power directed to RX6 is wasted on the metal cabinet.
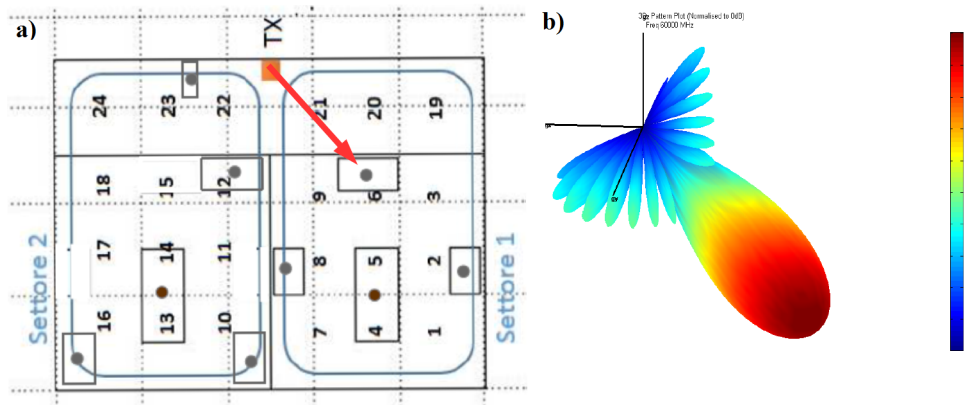
FIGURE 7.10: Radial BF for RX6: a) 2D map, the red arrow indicates the BF pointing; b) normalized radiation pattern at TX.

- Single BF: the strongest paths are determined through RT simulation (e.g. RT-assisted BF) with isotropic antenna and then the TX main beam is steered toward the AOD of the path yielding the best CINR value at the user. In Fig.7.11 about NLOS RX6, with respect to the radial method, a single-order reflection (see Fig.7.13) off the bottom wall is exploited to overcome the cabinet obstruction.
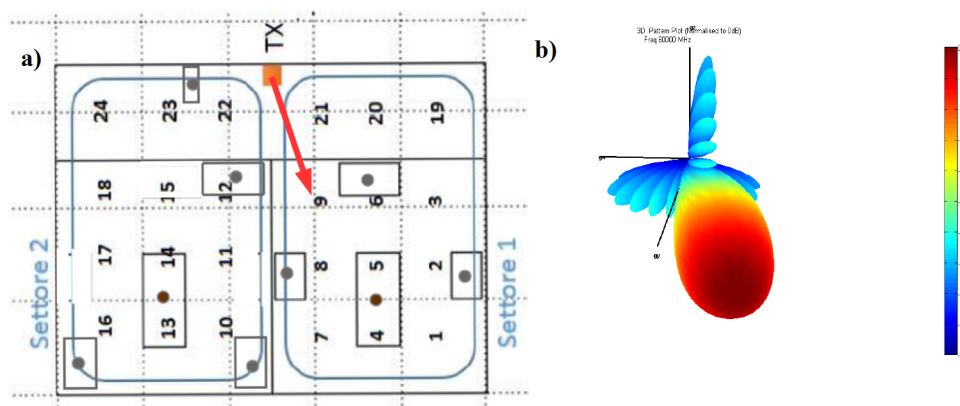

FIGURE 7.11: Single BF for RX6: a) 2D map, the red arrow indicates the BF pointing; b) normalized radiation pattern at TX.

- Multi BF: the TX, as well as in SBF, retrieves the channel information from RT simulations, as starting point, but in this case chooses (according to a predetermined number called Beams Order (BO)) a set of best directions, where

the propagation conditions are favorable. The result is an overall pattern with multiple beams that point to different directions, covering more angles and creating more paths for the signal, in order to achieve indeed Spatial Diversity. This method is for Single-User BF only. In case of rays stopped along the primary path by a walking person, all the other rays, that follow different propagation routes, could sustain the link quality avoiding dramatic power drops and reducing the whole outage probability. See Fig.7.12 for RX6 with BO=4 and Fig.7.13 with BO=2, as examples.
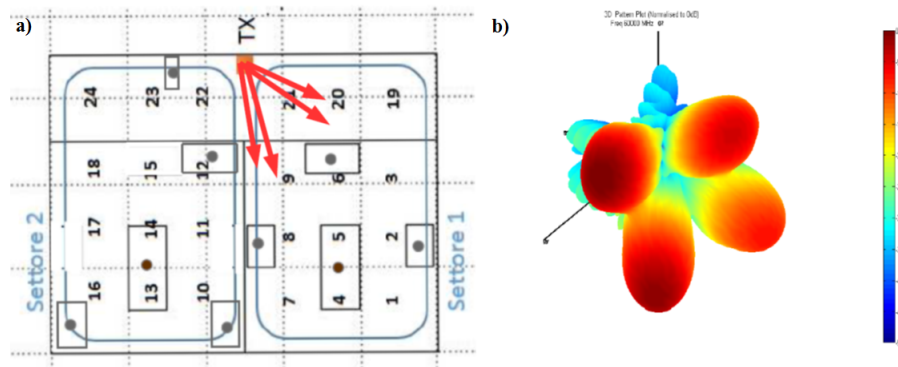
FIGURE 7.12: Multi BF for RX6: a) 2D map, the red arrow indicates the 4 directions of BF; b) normalized radiation pattern at TX with 4 beams combined.
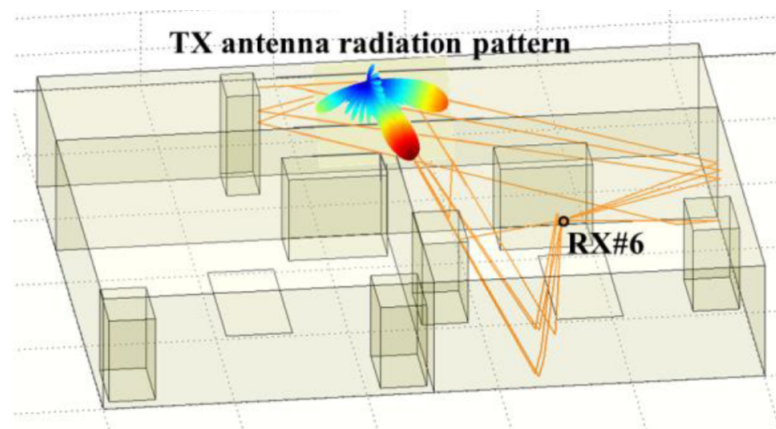
FIGURE 7.13: Example of Multi-beam BF with 2 beams. The radiation lobes are steered towards the directions of departure of the two strongest paths.

7.2.4   Multi-Beam Beamforming

In addition to traditional steering techniques (SBF), in multi-beam solutions (MBF) the availability of multiple beams opens more degrees of freedom in the BF procedure because each beam can be weighted with respect to the others, balancing the power allocation in the end, Sun [212]. As shown in the following, the total radiation pattern (F_{tot}) derives from a linear combination of single radiation pattern (F_j), Balanis[51]:

$$F_{tot} = \sum_{j=1}^{BO} \left(p_j \cdot F_j \right).$$

Eq. 7.6

Each radiation pattern can be combined numerically by a scalar weight called p_j balancing in a non-uniform way the power distributed on the considered beams. A graphical example of a 2 beams merged together with weights p1 and p2 is given in Fig.7.14.
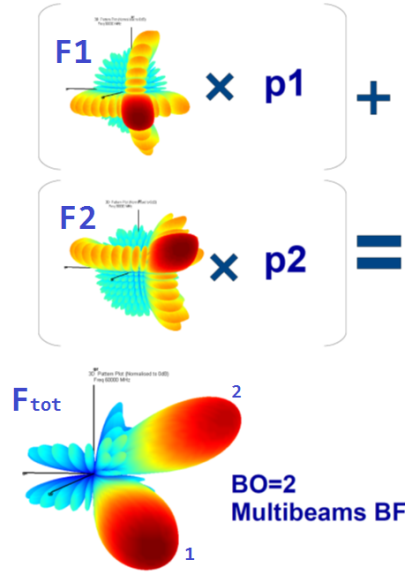
FIGURE 7.14: Example of linear beams combining with BO=2. The partial and total antenna radiation patterns are plotted with normalized amplitude in dBi.

Similarly to MRC scheme for RX diversity, the choice of the weights at TX side can be carried out allocating power where it is worth, according to the radio channel conditions (predicted by the RT here). This is performed according to Eq.7.7: the weight p_j is computed taken into account the received power, collected from all the rays outcoming from the j-th beam, and the total amount of power emitted by the TX. In this manner, the weight p is meant to be proportional to the channel gains experienced by the rays which travel along the paths related to the BO MBF beams. In the context of multi-beam BF, it is worth reminding that all of this is possible thanks to RT tool which enables the CSI estimation of the indoor radio channel.

$$p_j = \sqrt{\frac{Power_j}{Power_{total}}}.$$

Eq. 7.7

The trade-off of this simple beams weighting scheme is essentially given by the amount of spatial diversity versus the level of CINR received at RX side. For example if all the weights p are unitary we obtain BO beams with no amplitude difference (i.e. Equal Gain Combining) and so achieving the maximum diversity in the spatial

domain. Otherwise we can make some of the beams "stronger or weaker" with respect to the others, till reaching the extreme case where the MBF degenerates into the SBF and so no diversity is involved.

Moreover, Multi-BF scheme is also suitable for 'a priori' Equalization processing, as outlined by Dupleich [213]: after RT simulation, TX selects the BO best AODs and focus the power towards these directions. Usually, at RX the rays come from different AOAs and with different delays too. The exploited multipath by means of Multibeams BF is indeed not completely under control because there is no constructive sum at receiver of signal replicas (i.e. the CINR is not maximized multi-dimensionally). Therefore, a re-alignment procedure in time and phase (i.e. pre-equalization, at TX side) is proposed, as explained in Fig.7.15.
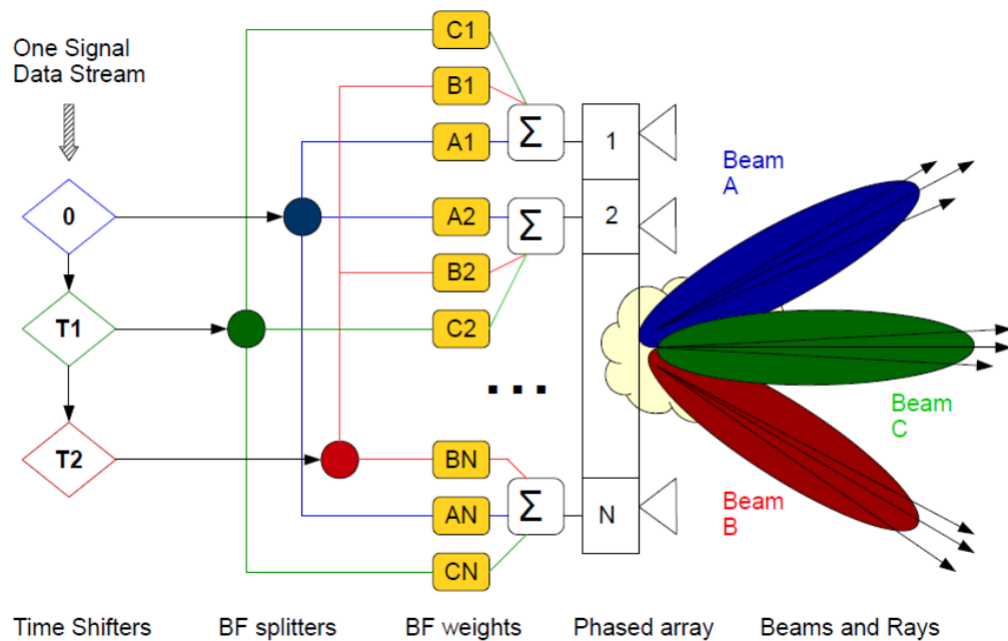
FIGURE 7.15: Qualitative schematic of MBF with pre-Equalization.

TX shall manage the signal in time sending different delayed versions of it into the BF blocks such that all the rays with AOD inside the considered beams could arrive at the same time at RX side. For example with BO equal to 3, (Fig.7.15), the TX orders the beams in terms of delays: the first beam, called A, that is related to the slowest rays -and of course to the longest paths- the second intermediate one, that is C, and in the end, the third one, called B, related to the fastest rays. Setting a precise clock and calculating the differences among the three beams rays delays the TX sends the signal in postponed instants. This technique is a complete space-time processing strictly based deterministic RT predictions with a huge level of complexity. For sake of completeness, nevertheless, it is possible to think about a more complete equalization that could take into account even the polarization where the polarization of the field emitted through the different beams can be similarly a priori modified in order to provide a strong polarization matching at the RX.

7.2.5   Results

In Fig.7.16 the mean value of the CINR, computed for each of the 24 locations is reported for the three BF techniques.
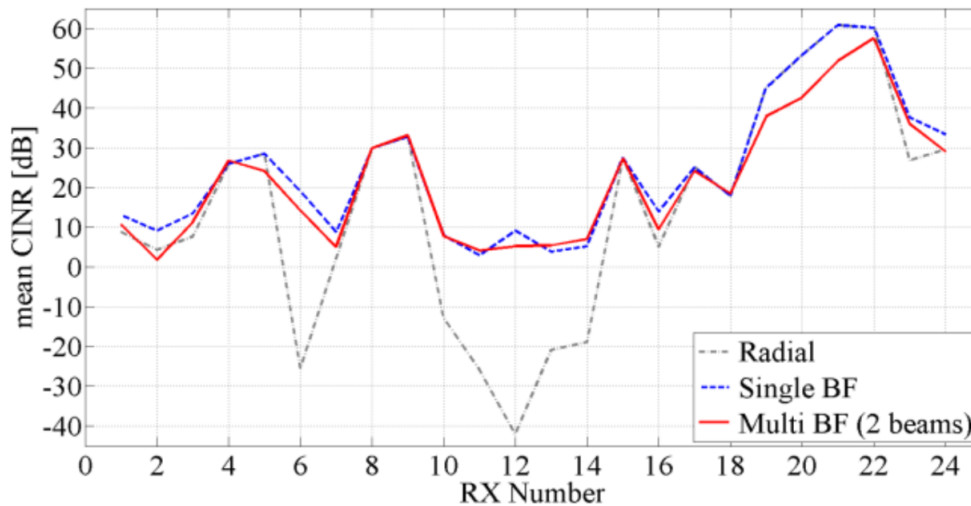
FIGURE 7.16: CINR values for different RX locations and BF solutions.

In fig.7.16, the performance are strongly location-dependent, since multipath is strictly related to the position of the receiver in the specific environment (e.g. RX6 and RX12 suffer from strong-NLOS conditions). The radial BF strategy of course poorly performs for NLOS receivers, while the single BF is the best solution in most cases, comparably to MBF with 2beams.

This fact can be explained by observing results in Fig.7.17, where the cumulative distribution (CDF), (collecting all simulations over the RX positions), of the power intensity differences between the 1st (strongest) path and the 2nd, 3rd, 4th and 5th paths, respectively, are plotted.
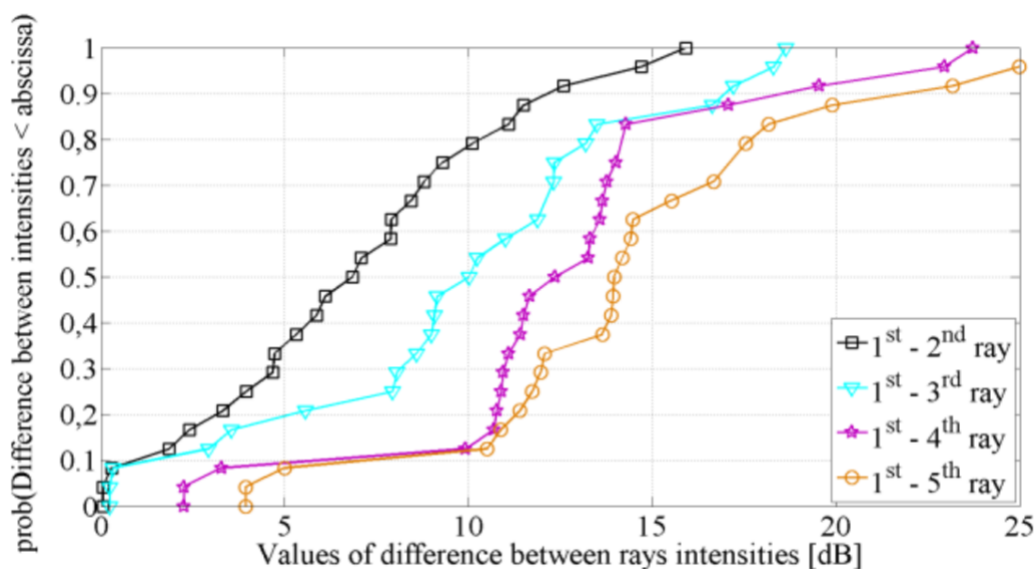
FIGURE 7.17: CDFs of the difference between the rays intensity.

For 80% of the rays the power gap, with respect to the 1st ray power level, is about 10dB for the second ray, 12.5dB for the third, 14dB for the fourth one and even 17.5dB for the fifth. In the considered environment there is always a dominant path towards which all the available power for transmission can be directed. This is in line with usual propagation considerations in indoor scenario for lower frequencies

where beyond a few strongest paths all the others are likely to be 10 or 20dB lower. This consideration is valid in general for all office-like environments with plasterboard walls.

Said that, performance of multi-BF may downgrade in particular if the power is uniformly distributed over all beams. This behavior is due to the fast reduction of the ray intensity with the increasing order of rays (Fig.7.17), therefore the radiated power in the direction of the 3rd and of the 4th ray is basically wasted in most cases. In order to limit power waste toward "useless directions", a non-uniform distribution of power can be implemented, according to MRC, as defined before.

In Fig.7.18, a preliminary implementation of the MBF pre-Equalization (Fig.7.15) is demonstrated. In details, the average values of CINR are reported corresponding to an allocated power for each beam proportional to the associated path gain (in accordance with the MRC algorithm). Results show the slight improvement of the MRC solution with respect to the uniform power distribution (red and green bar chart, left and right in Fig.7.18).
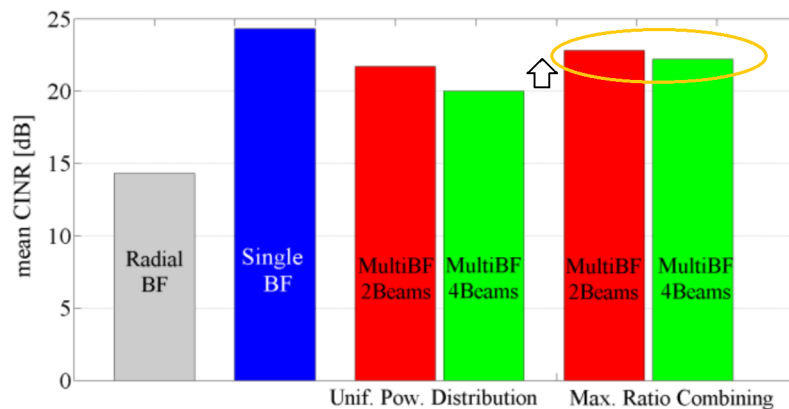
FIGURE 7.18: Mean CINR values for the considered BF solutions and for different power allocation across the lobes in MBF.

Simulations shown so far are all in static conditions, i.e. no mobility inside the propagation environment is taken into account. Nevertheless, people may move indoor, and therefore temporary partial/total obstruction of the rays may occur. In order to estimate the robustness of the considered BF solution to unexpected blockage, an additional loss of 30dB (representative of full human blockage) has been added on the main radiation lobe. See chapter (2), section 2.3, Fig. 2.6.

The mean CINR value decreases for all the solutions, but the reduction is about 6dB less severe for MBF with respect to SBF. Of course this is due to the intrinsic spatial diversity gain of the multi-BF schemes. Moreover, the more uniform the power distribution among the beams, the larger the diversity gain and the stronger system robustness to blockage impairment. In particular the reduction of the mean CINR for a two-beam multi BF case with uniform distribution of power is equal to 12dB, while it is equal to 16dB for the MRC power distribution.

In conclusion there is a trade-off between performance in static conditions, which would benefit from uneven power distribution among beams, and the capability to cope with sudden unpredictable link obstruction, which would require a more uniform power distribution. The simple, radial solution is more insensitive to possible, dynamic obstruction of the radial path than single BF. This can be explained considering that the additional human blockage loss is a real impairment only when the

radial path is in LOS conditions, otherwise the latter extra attenuation is not significant.

7.2.6 Preliminary Evaluation of Polarimetric Beamforming

Similarly, the same RT-BF system simulator has now been used to investigate the performance of polarimetric BF schemes in terms of CINR in an indoor multi-user environment, with a slight larger environment. The same office above (Fig.7.8-7.9) has been replicated and stacked horizontally on the same floor of the ideal building. Each office hosts a transmitter (TX) that can communicate with receivers placed in several pre-fixed locations (green and red dots), i.e. it represents a cell of an indoor cellular layout, as depicted Figure 7.19.
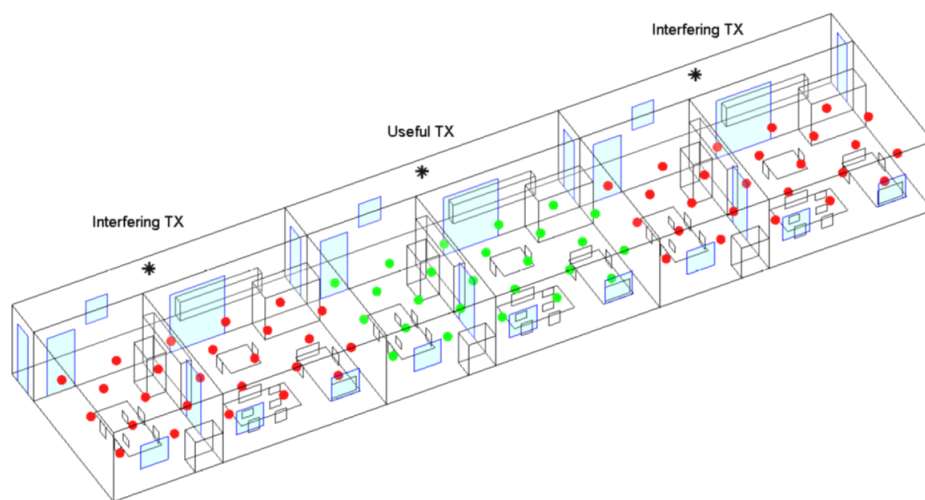
FIGURE 7.19: The 3 offices simulated scenario. Green dots are users RXs, red dots are interferer RXs.

The same RR (e.g. SDMA beams) are assumed to be re-used within all the cells, that is each cell is affected by the interference coming from the adjacent ones (i.e. 1 user RX and 2 RX interferers). The central office has been considered as the "useful" cell, and the adjacent ones act as interfering cell. In order to investigate the statistical properties of the CINR, 24 pairs of receivers have been randomly generated inside the two interfering cells for each RX in the central office in a Monte Carlo simulation, as well as before.

Now, the main focus has been drawn onto the polarization characteristics of the BF links, considering only vertically-polarized TX antenna array and simulating the received CINR both with perfect polarization matching (using the same concept of 'a priori' equalization explained, Fig. 7.15) and with random / uncontrolled polarization case at the receiver ("unmatched" case). The CDF of the CINR has been then computed for the different BF solutions in the matched / unmatched cases based on the set of CINR values collected for each receiving location in the central office and for the different, random positioning of the receivers in the adjacent cells. The overall CDFs are shown in Fig.7.20 for the single and radial BF solution (solid and dashed lines respectively) and for "matched" and "unmatched" polarization cases (black and grey lines respectively).
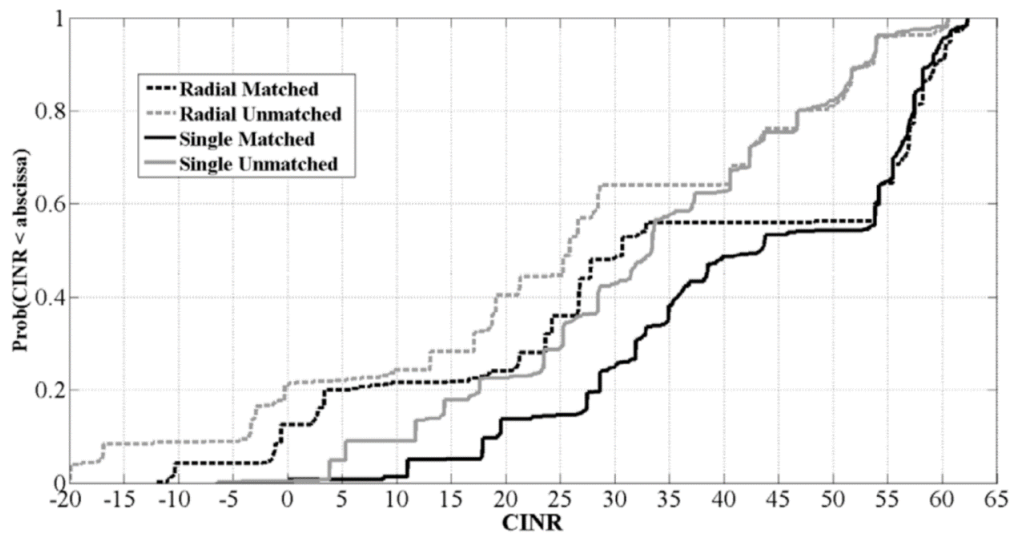
FIGURE 7.20: CDF of the mean CINR in the polarization matched and unmatched cases, with radial and single BF schemes.

In presence of a prevailing received multipath contribution from the radial direction (LOS), the Single and the Radial BF solutions are of course coincident, leading to unreal CINR values up to 60dB. On the contrary, if the radial direction is heavily obstructed the CINR value may result very low (e.g. negative) with non-negligible probability. Summarizing, Fig.7.20 shows that the Single BF approach exhibits a greater robustness in the NLOS cases, due to the capability of radiating the transmitted power in a more effective way. In terms of mean CINR value, the improvement (e.g. right shift, roughly speaking) provided by the Single BF solution is equal to about 8dB in both the matched and the unmatched cases.
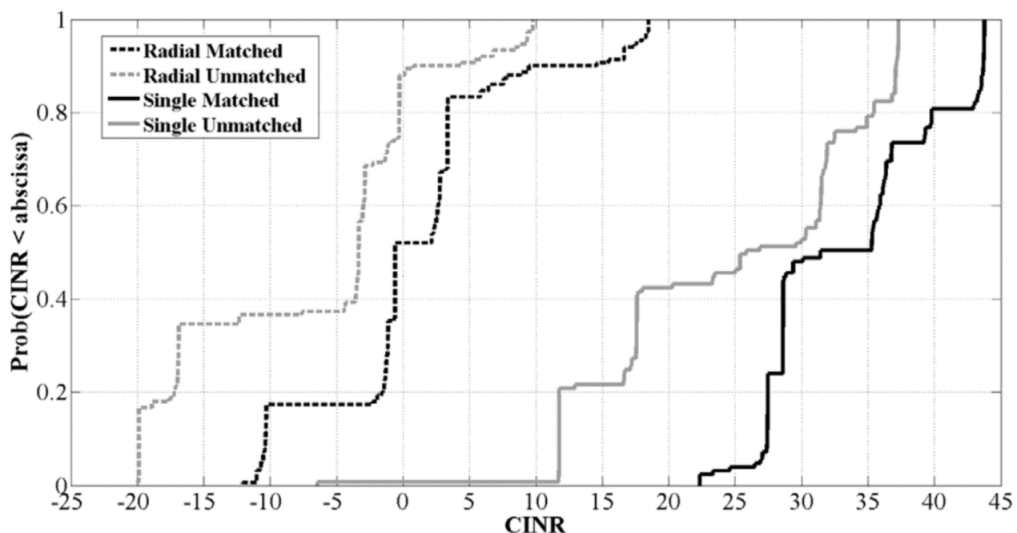
FIGURE 7.21: CDF of the mean CINR for the NLOS receiving locations for the different polarization and BF cases.

This trend is further highlighted in Fig.7.21, where the CDFs have been limited to the NLOS situations (e.g. RX6), only. It is evident that when the receivers are in

NLOS condition a huge gain up to 30dB is obtained by steering the beam towards the direction of the strongest path (Single BF) with respect to the radial BF case.

As far as the polarization issues are concerned, the capability of equalization may clearly improve the system performance, keeping the CINR values always above 10dB and achieving an increase of the mean CINR value equal to about 9dB, in both the Radial and the Single BF cases.

7.2.7 Ray Tracing Assisted Beamforming

The BF strategies introduced before clearly assume a thorough knowledge of the directional characteristics of the radio channel, as well as the awareness of the position of the devices. This might open up new prospects, where ray-based radio channel models such as RT could support the radio devices in the BF process, piloting the "decision-making" (totally or partially) thanks to reliable deterministic predictions. It's worth noticing that RT-based BF could naturally cope with fast and sudden channel changes (e.g. abrupt human blockage), because once the stronger paths have been tracked by the RT engine, their information could be easily stored and remotely read, so that the beam(s) could be quickly re-arranged if needed, as already outlined. Moreover, RT-assisted BF could be even faster than standard BF solutions, provided that the paths tracking time in the RT tool is lower than (or at least comparable to) the average time interval necessary to complete the exhaustive search BF standard protocols. In order to perform a preliminary comparison, the computation time required by RT simulations (same environment of Fig.7.19) are shown in the following Table 7.5.

Interactions	Computation time (ms)
1 refl., 0 transm.	12
1 refl., 1 transm.	16
2 refl., 0 transm.	220
2 refl., 1 transm.	225

Table 7.5: RT simulation CPU time.

The above SW computation time (< 250 msec) refers to a standard laptop with no special feature. However a drastic reduction up to two orders of magnitude in CPU time can be achieved by properly parallelizing the algorithm and exploiting GPUs. On the other hand, in Roh [18], a mmWaves BF prototype for 5G wireless systems exhibits a beam searching time estimated equal to 45msec, where, nevertheless, the beam scanning range has been limited to 60°in the horizontal plane and the HPBW is equal to about 10°for each radiation pattern. Therefore, it can be argued that in case of a full 3D scanning carried out with very narrow pencil-beams (i.e. HPBW of few degrees) the beamforming time could rise up to some hundreds of msec, as well as RT-based BF times shown here. Although further investigations are necessary, this preliminary assessment might suggest that real time, RT-assisted BF is a promising technique that deserves consideration.

Final Conclusion

The features of incoming wireless systems beyond LTE, as 5G, have been outlined in line with the International Telecommunication Union specifications (Ch1), motivating the need to satisfy the raising demand of data rate and ubiquitous connectivity by exploring new frequencies Above-6GHz, named cmWaves and mmWaves. These new bands are currently under debate, opening new challenges for the wireless community. Novel propagation and channel modelling issues together with massive multi-antenna systems design are today indeed under investigations for Above-6GHz bands, as confirmed by many international research projects (Ch2).

In particular, ray-based radio channel models, as Ray Tracing, are drawing attention with respect to stochastic models, due to their qualities as frequency-agility, scenario-independence and spatial analysis predisposition. A Ray Tracing simulation tool designed at University of Bologna has been explained in details and then used to assess the radio channel properties Above-6GHz (Ch3).

Initially, two novel measurements methods for the electromagnetic characterizations of construction material and common items have been described (Ch4), in order to provide cm/mmWaves inputs data for the Ray Tracing tool. This item-level characterization has been conducted firstly, exploiting the principle of Fabry-Perot Resonance in wide-band measurement with Vector Network Analyzer around 7-15GHz (Fig.4.8) and secondly, by using a 70GHz Channel Sounder with rotational units in anechoic chamber, in collaboration with TU Ilmenau (Fig.4.11).

The first method only requires a simple fixed measurement setup without any complicated calibration routine. It allows the independent determination of the real and imaginary part of the complex permittivity without any post-processing optimization routine. Results of complex permittivity values around 7-15GHz have been achieved for different material as Sandstone, Marble, Wood, Chipboard, Paper, in agreement with the literature values, (Table 4.1). Theoretical formulation of the Fabry-Perot resonance has shown good matching with measurement data for most of the tested dielectrics (Fig.4.9).

The second method takes into account also the scattering and polarization properties of different tested objects (made of compound materials) as brick wall, monitor, pot, bookshelf, music speaker, wooden panel, wooden cabinet, in order to calibrate the Ray Tracing tool at mmWaves. Item-level results (Tables 4.3-4.4) have shown quite heavy obstruction losses with a specific attenuation approximately ranging from 1 to 6dB/cm. For example penetration losses due to radio wave propagation through a brick wall may be five times the corresponding value at 1GHz. Moreover, surface roughness as well as inner unhomogeneities seems to foster cross-polarization coupling, whereas on the contrary is reduced in presence of sharp, structural protrusions and/or indentations on the item surface. With reference to the scattering patterns (Fig.4.16), a backscattering lobe around the direction of specular reflection can be identified for most of the considered items, with an angular amplitude mainly determined by the degree of surface irregularities. On the contrary, a forward scattering lobe cannot be always spotted out, since the power is often uniformly widespread in the forward half-space.

Thanks to the knowledge of both the electromagnetic characteristics of different items and the main parameters of the single-lobe diffuse scattering model, multi-dimensional simulations of in-room 70-GHz propagation (Fig.5.1) have been performed using double directional Channel Sounder measurement, as radio channel reference (Ch5). In particular, good Ray Tracing predictions have been achieved, with a total received power Root Mean Squared Error (RMSE) lower than 2dB, a power angle profile Weighted-RMSE of about 3dB (Fig.5.6) and a RMS Delay Spread percentage error of about 5% (Fig.5.9). Reflections contribute with more than 70% of the NLOS received power, whereas diffuse scattering combined with other inter-actions contributes with about $20 - 30\%$ of the NLOS power. Reflection seems to be the dominant propagation mechanism, whereas scattering is not negligible and seems even slightly greater than at frequencies Below-6GHz, in the tested scenario (Fig.5.11). Most of the strong multipath contributions come from the macro-structure of the office, even though other interactions with smaller furnishings elements or structural details are important, especially if made of metal.

Moving on, multi-antenna Systems, as MIMO and BF has been taken into consideration for Above-6GHz frequencies assessment, focusing overall on Beamforming Switching and Beam Search issues (Ch6). Modern hardware architecture, for sake of completeness, are illustrated in Appendix, also.

Then, (Ch7), the Ray Tracing has been used to investigate advanced BF techniques in terms of Signal-to-Noise-and-Interference-Ratio (SINR) in indoor multi-user environment, where different communications are assumed to be divided through space-division only.

Firstly, the impact of interference in Multi-User Beamforming network is assessed using the same scenario and set-up of previous multidimensional mmWaves radio channel characterization (Ch5). Three different Beamforming schemes, named "Radial", "Best-S" and "Best-SINR" are proposed and tested. Multi-User Beamforming solutions, as Best-S, which do not take into account interference may fail to provide a good throughput to all the users. Instead, Best-SINR method overcomes all the other achieving the best trade-off between data rate and fairness among the users (Fig. 7.5). A noticeable 15dB of gain in SINR is obtained in case of joint Beamforming, where also the receiver terminal is capable to scan the spatial domain (Fig. 7.6). Ray Tracing Multi-User Beamforming simulations results are checked against Measurements Multi-User Beamforming results, achieving good matching SINR distribution (Fig. 7.7) and small predictions RMSE (Table 7.3). These exciting results have led to the implementation of the novel concept of RT-assisted Beamforming, where Ray-Tracing assists the Beamforming algorthims to speed up the Beam Search and Tracking procedure, indicating the directions where to allocate the beams for the communications. On average, a gap of 6dB of error has been found between RT-assisted Beamforming and Measurements-based Beamforming, with promising insights for future developments.

Secondly, further investigations on Beamforming have been performed at 60GHz to tackle the issues related to the lack of LOS in indoor scenario. Several diversity schemes, as the novel Multi-Beam BF (Fig.7.12-13), have been tested to provide valid solutions to cope with disruptive NLOS events. Multi-Beam Beamforming performs indeed almost as well as Single-Beam Beamforming, adding a diversity gain of up to 10dB in case of human blockage on the dominant path.

Appendix A

the Electronics Corner

Previous insights about multiple antennas techniques, as MIMO or Beamforming, for Above-6GHz applications are described herein with a practical perspective in terms of electronics, because Hardware (HW) still plays a very important key role in today wireless communications, as outlined in chapters (2) and (6). For example, increasing the number of antenna elements (e.g. massive MIMO) and also increasing the frequency/bandwidth (e.g. Above-6GHz) result in new challenges for radio terminals architectures, requiring the design of multiple RF chains at higher bands trading-off between power efficiency, linearity and costs, Pozar [214].

Moreover, it is worth reminding that flaws in the antennas and RF circuits can influence directly not only measurements or Over-The-Air (OTA) tests, but the channel model predictions also, even though the propagation does not change at all: antenna elements coupling can create correlation among MIMO streams, spurious emissions due to the saturation of power amplifier (PA) may impact on the interference, or impedance coupling in the RF front-end can impair the BF network. These are important points to be taken into account for reliable LLS simulation or on-field measurement.

A.1 Above-6GHz Hw challenges

Now the question is: is the actual state-of-the-art electronics ready to fully support the implementation of multiple-antenna cm/mmWaves devices? The whole picture is still not clear but it can be captured only broadening the focus from the propagation and communication point of view, to assess practically the feasibility of cm/mmWaves system.

New Hw challenges are indeed listed in the following:

- carrier frequency raised up 100x, from 1 GHz up to 100 GHz.

- bandwidth larger than 100 MHz, up to 2 GHz.

- data rate from hundreds of Mbps to tens of Gbps.

- parallel RF chains from 2 up to 32. (even more with Carrier Aggregation).

- more energy efficiency, less power consumption.

- advanced (parallel) digital processing for DSP and multiple RF chains.

A.2 Above-6GHz Hw issues

The above challenges pone several issues for good HW design, due to the novel use of Above-6GHz bands, as reported by Rappaport in [215] and [15]. Many problems are still open, [22].

- Power: power consumption is likely to be the most important parameter being cause of significant constraint scaling up the number of RF chains. Concerning watts in communications it is necessary at the User Equipment (e.g. UE) side, to save battery and even more at the Base Transceiver Station (e.g. eNB) to reduce electricity bills cost for TLC network operators, Auer [216]. Especially PA using multi-carrier modulation as OFDM could come across linearity problems, expressed in terms of Peak-to-Average Power Ratio (PAPR) or Power-Added-Efficiency (PAE), for example, Dunsmore [217]. Besides improving the kind of modulation, techniques as Envelope Tracking o Digital-Pre-Distorsion can be used to mitigate this problem. Moreover, power means heat to be dissipated, also. The design of circuits with multiple RF chains require noticeable integration of thermal and power dissipation models for the entire RF front-end.

- Non-linearity: all RF electronics is based on non-linearity to convert and mix signals. Let's think about oscillators that from DC power create RF signal. The negative drawback is that non-linearity corrupt the useful information changing the phase and amplitude (and even the spectrum) of any waveform, proportionally to the level of power involved in the elaboration. When a circuital block is over-driven with too much power, it occurs the spreading of the power outside the bandwidth, generating the well-known Intermodulation Distortion (IMD), as main consequence of non-linearity. Once again, the power represent the main concern for HW design.

- Antenna Design: due to compact size of antenna array the RF design could face problems of unbalanced Impedance matching and even elements Coupling. Considering massive MIMO hundreds of elements are assumed to be packed in the same array. This could lead to the trade-off between antenna area and isolation among elements.

- ADC: Analog-to-Digital-Converters (ADC) are fundamental to achieve good data-rate with high SNR. Due to the fast Gbps data rate envisioned for future wireless systems at cm/mmWaves, ADC design face a wide trade-off that involves resolution (bit/sample), dynamic range, sampling rate (sample/sec), power consumption (watt/sample), I/Q Balance, Bowick [218]. Moreover, parallel RF chains need bank of parallel ADC limiting the overall energy efficiency of the device, in the end.

- Manufacturing technology: in the past, the well-known Moore law ruled the progress of transistor allowing an incredible progress of ICT. However, even though today nano-electronics allows chipset with transistor scaled down up to ∼10nm, things are changing as testified by the new motto "More-than-Moore", as described by Arden [219] (i.e. International Technology Roadmap for Semiconductors (ITRS) roadmapping). Besides miniaturization, indeed, the key word has become diversification, looking for alternatives to Silicon. Regarding cm/mmWaves, in our case, two "families" are competing for RF circuits: RF Complementary metal oxide semiconductor (CMOS or Si-Ge), which

is mature technology but with some flaws to handle high frequency, versus the compounds of the group III-V as gallium-arsenide (GaAs), gallium-nitride (GaN), and indium-phosphide (InP), which is more expensive but offers good properties in terms of power and frequency. Fig.A.1.
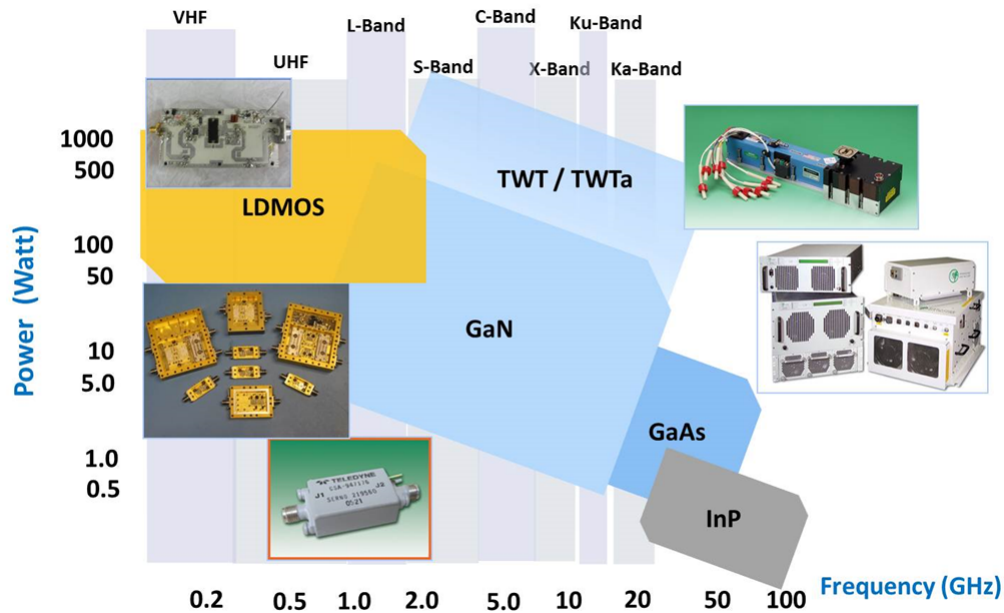

FIGURE A.1: Different technologies versus power and frequency up to 100GHz.

- Noise: complementary to non-linearity distortion, noise limits the lower bound of the power scale. Assessing the feasible receiving sensitivity of devices, generally different sources of noise should be considered, e.g. AWGN, Shot noise, Flicker noise, Burst or G-N noise, dependently on technology and frequency. This variety of causes make the noise influence proportional to the bandwidth and the frequency, of course non-linearly. All of this ends up in penalizing the Above-6GHz architectures to be more noisy.

- Up and Down Conversion: up / down mixers and frequencies multipliers / dividers are necessary to reach cm/mmWaves, starting from relatively low-frequency tones, as usual. Unfortunately, at Above-6GHz, the higher noise floor add further Jitter ad Isolation issues to the design of Oscillators (VCO and OSC) which are more sensitive to phase noise problems, Razavi [220].

In the following a fast outline of the actual proposed HW architectures for Above-6GHz systems is presented. In literature it is remarkable the pioneering work done by Samsung concerning the practical feasibility of mmWaves in [17], the design of mmWaves antennas in [19] and the related role of BF in [18].

A.3 Above-6GHz Hw solutions

A.3.1 Analog architecture

Analog architecture comprises mainly analog Beamforming, which allows the arbitrary shaping of the radiation pattern of an antenna array thanks to a BF network.

As documented by Romanofsky, [221], the Beamforming blocks are indeed Transmission and Reception, i.e. "T/R" modules. Commonly Phase Shifters enable to modify arbitrarily the phase of the signal along the RF path, via external 'n' bits digital commands. Of course, more bits allow finer angle resolution in the phase shifting. For example, with 5 bits, a phase shifter has a set of 32 different phases with about 11°of resolution on each RF path.

Fig.A.2 and Fig.A.3 show Analog BF at RX side with TR modules implementing BF before the IF section.
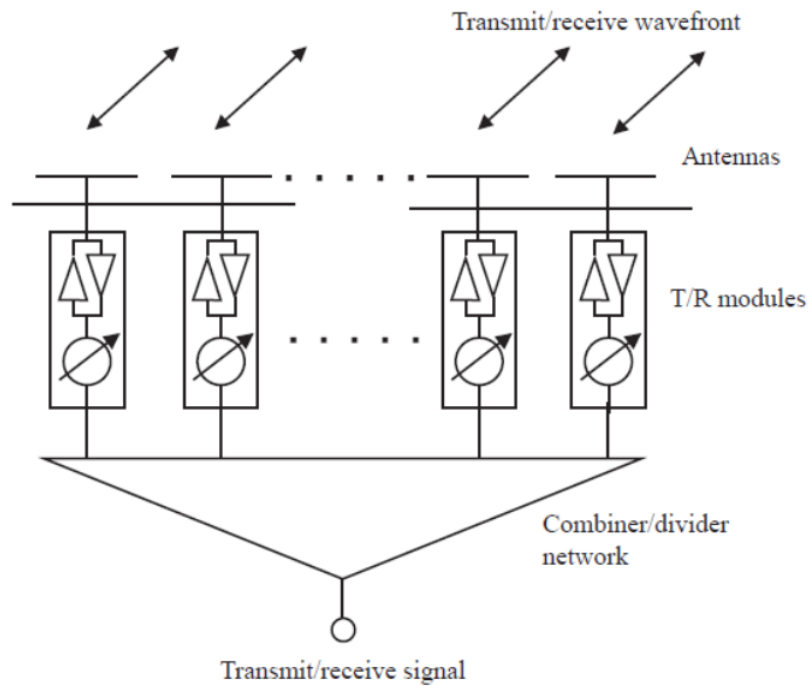

FIGURE A.2: Example of T/R module.
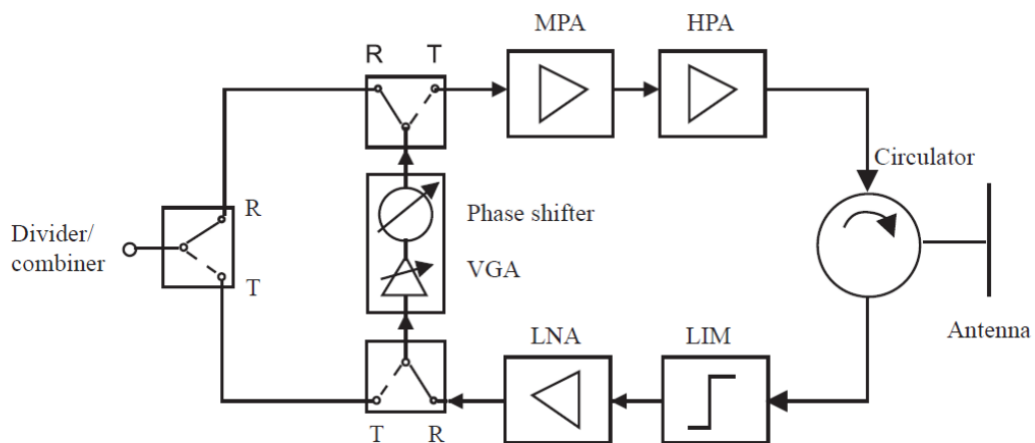
FIGURE A.3: A shematic of T/R module inside for BF.

Fig.A.4 shows Analog BF at RX side implementing BF at IF after the first down-mixing section.
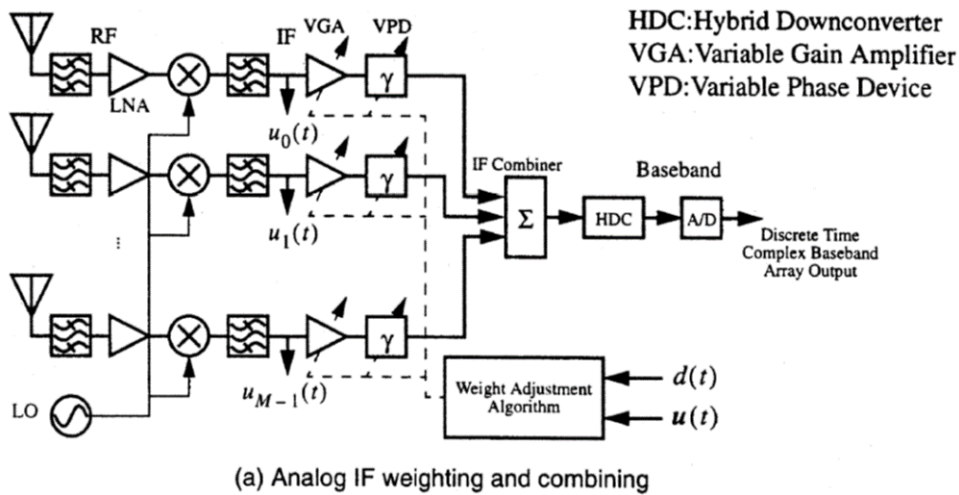
FIGURE A.4: Analog IF BF scheme at receiving side.

Finally, it is worth reminding the analog BF architectures may deal with two main problems: 1- the control on sidelobes using analog BF architectures is not flawless, especially with large bandwidth signals or high power levels, because the behavior of phase shifters may vary along frequency or non linearly with power. So, it may occur that a non-negligible amount of power is emitted out of the main beam, towards different directions with respect to the look direction, however. This effect can be managed choosing carefully the phase, (and even the amplitude) of the Steering Vectors (e.g. combining weights) in the BF network. For example implementing the BF synthesis with Dolph-Chebyshev weights it is possible to fix the gain ratio between the main beam and sidelobes of the radiation pattern. 2- BF is limited by a the trade-off between the gain of the antenna array and its Field of View (FOV), which is the angular range where it is possible to steer the antenna. In fact, pointing towards angles which are out of the FOV, off-boresight (i.e. grazing the array plane) the overall gain will decrease, and the HPBW enlarged. This is the phenomenon called Beam Squint, which limits the spatial scan of any BF device.

A.3.2 Digital architecture

On the contrary, the digital architecture is combined with MIMO techniques and is usually located before the ADC section, exploiting the flexibility of DSP, as in Fig.A.5 and Fig.A.6, to combine the data digitally. Modern solutions implementing MIMO (e.g. STBC or Spatial Multiplexing) are based on a design which, for example, comprises a block at TX side (e.g. named pre-coder in the Fig.A.5) and a block at Rx side (e.g. named combiner in the Fig.A.5), in accordance with SVD, (see chapter (6)). Practically, the handling of different MIMO streams can be simply implemented by using fast matrices products onto the digital samples/symbols as in Fig.A.5.
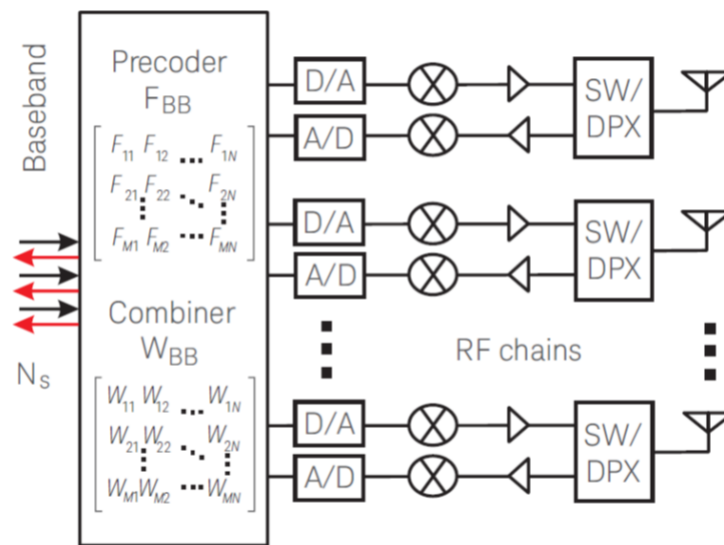
FIGURE A.5: Digital MIMO architecture from Keysight ®.

In fact, differently from analog schemes previously described, these digital schemes naturally deal with samples/symbols in the baseband, relying upon the ability of A/D Converters to "translate" correctly the combined digital samples into analog signals (and viceversa at RX). This advantage leads to huge flexibility in terms of processing and numerical errors.
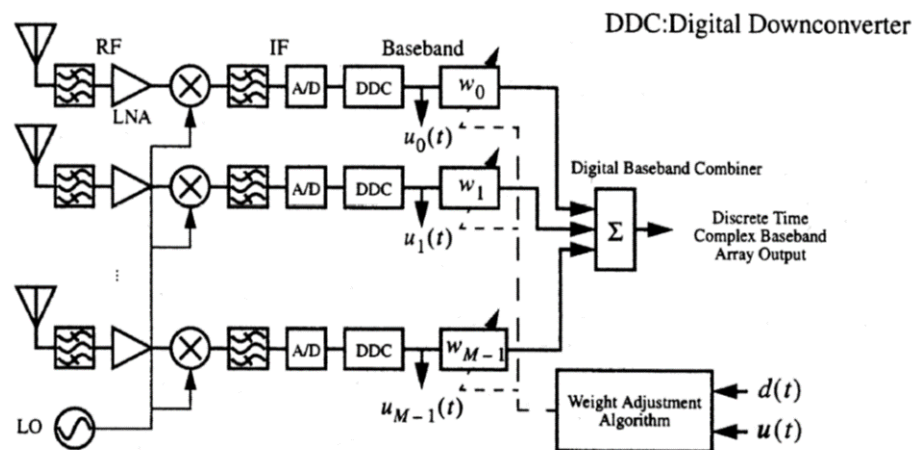
(b) Digital complex baseband weighting and combining

FIGURE A.6: Digital baseband BF scheme at receiving side.

A.3.3   Hybrid architecture

As illustrated by Dupleich [213] and Samsung [17], [19], [18], a novel Hybrid architecture is currently the trend for future multiple antennas architectures, because both the pros of the two aforementioned different approaches are gained in a complementary way. This is shown by Fig.A.7, depicting a general purpose hybrid architecture with multiple RF chains, where at TX side there are: a pre-coder block (e.g. (F_{BB}) matrix, Fig.A.7), the D/A conversion and then the analog BF combining(F_{RF}). At RX

side, instead: analog BF combining (W_{RF}), A/D conversion and then a combining block (e.g. (W_{BB}), Fig.A.7).
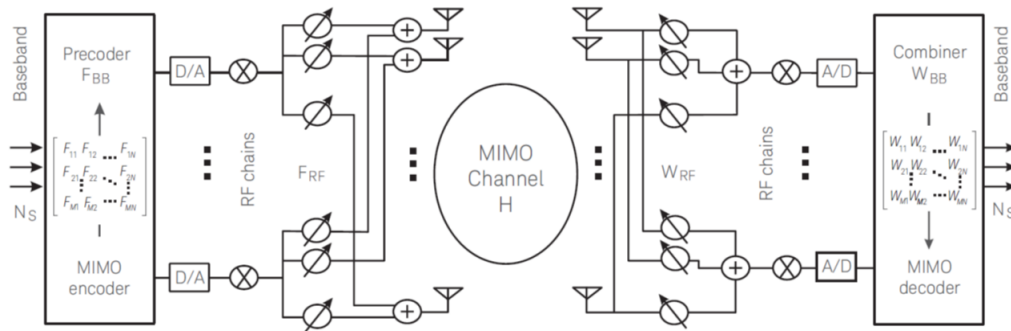
FIGURE A.7: Complete hybrid BF / MIMO architecture from Keysight ®.

A physicist, a biologist and a mathematician sit in a sidewalk cafe, looking at the building across the road. Two people go into the building, then three people come out.
Physicist: "This must be a measuring error!".
Biologist: "This is proof of procreation!".
Mathematician: "If one more person goes into the building, it will be empty!"

Bibliography

[1] ITU, *Draft new report itu-r m. minimum requirements related to technical performance for imt-2020 radio interface(s)*, 2017. [Online]. Available: http://www.itu.int/en/mediacentre/Pages/2017-PR04.aspx.

[2] E. Commission, *The eu framework programme for research and innovation*, 2014-2020. [Online]. Available: https://ec.europa.eu/programmes/horizon2020/.

[3] 3GPP, *Tr 38.900 v.14.3.1: Technical specification group radio access network; study on channel model for frequency spectrum above 6 ghz (release 14)*, 2017.

[4] ——, *Release 15*, 2017. [Online]. Available: http://www.3gpp.org/release-15.

[5] D. Astely, E. Dahlman, A. Furuskar, Y. Jading, M. Lindstrom, and S. Parkvall, "Lte: The evolution of mobile broadband", *IEEE Communications Magazine*, 2009.

[6] A. Ghosh, R. Ratasuk, B. Mondal, N. Mangalvedhe, and T. Thomas, "Lte-advanced: Next-generation wireless broadband technology", *IEEE Wireless Communications*, 2010.

[7] M. R. (Agilent), *LTE and the Evolution to 4G Wireless: Design and Measurement Challenges*. Wiley, 2013.

[8] N. Michailow, M. Matthe, I. Gaspar, A. Caldevilla, L. Mendes, A. Festag, and G. Fettweis, "Generalized frequency division multiplexing for 5th generation cellular networks", *IEEE Transactions on Communications*, 2014.

[9] P. Banelli, S. Buzzi, G. Colavolpe, A. Modenini, F. Rusek, and A. Ugolini, "Modulation formats and waveforms for 5g networks: Who will be the heir of ofdm?: An overview of alternative modulation schemes for improved spectral efficiency", *IEEE Signal Processing Magazine*, 2014.

[10] IEEE, *802.11n-2009 - ieee standard for information technology local and metropolitan area networks specific requirements part 11: Wireless lan medium access control (mac)and physical layer (phy) specifications amendment 5: Enhancements for higher throughput*, 2009.

[11] ——, *802.11ac-2013 - ieee standard for information technology–telecommunications and information exchange between systems-local and metropolitan area networks specific requirements part 11: Wireless lan medium access control (mac) and physical layer (phy) specifications amendment 4: Enhancements for very high throughput for operation in bands below 6 ghz.* 2013.

[12] ——, *Task group ax*. [Online]. Available: http://www.ieee802.org/11/Reports/tgax_update.htm.

[13] W. R. C. (WRC), *Resolution com6/20: Studies on frequency-related matters for international mobile telecommunications identification including possible additional allocations to the mobile services on a primary basis in portion(s) of the frequency range between 24.25 and 86 ghz for the future development of international mobile telecommunications for 2020 and beyond*, 2015.

[14] G. MacCartney, T. Rappaport, S. Sun, and S. Deng, "Indoor office wideband millimeter-wave propagation measurements and channel models at 28 and 73 ghz for ultra-dense 5g wireless networks", *IEEE Access*, 2015.

[15] T. Rappaport, R. Heath, R. Daniels, and J. Murdock, *Millimeter Wave Wireless Communications*. Prentice Hall, 2015.

[16] T. Rappaport, G. MacCartney, M. Samimi, and S. Sun, "Wideband millimeter-wave propagation measurements and channel models for future wireless communication system design", *IEEE Transactions on Communications*, 2015.

[17] W. Hong, K. Baek, Y. Lee, Y. Kim, and S. Ko, "Study and prototyping of practically large-scale mmwave antenna systems for 5g cellular devices", *IEEE Communications Magazine*, 2014.

[18] W. Roh, J. Seol, J. Park, B. Lee, Y. Kim, J. C. K. Cheun, and F. Aryanfar, "Millimeter-wave beamforming as an enabling technology for 5g cellular communications: Theoretical feasibility and prototype", *IEEE Communications Magazine*, 2014.

[19] Y. Kim, H. Lee, P. Hwang, R. Patro, J. Lee, W. Roh, and K. Cheun, "Feasibility of mobile cellular communications at millimeter wave frequency", *IEEE Journal on Selected Areas in Communications*, 2016.

[20] 5GPPP, *Mobile and wireless communications enablers for twenty-twenty (2020) information society ii*, 2015-2017. [Online]. Available: https://www.miweba. eu/Start.

[21] ——, *Mm-wave based mobile radio access network for 5g integrated communications*, 2017. [Online]. Available: https://5g-mmmagic.eu.

[22] ——,

[23] G. Wunder, P. Jung, M. Kasparick, T. Wild, F. Schaich, Y. Chen, S. Brink, I. Gaspar, N. Michailow, A. Festag, L. Mendes, N. Cassiau, D. Ktenas, M. Dryjanski, S. Pietrzyk, B. Eged, P. Vago, and F. Wiedmann, "5gnow: Non-orthogonal, asynchronous waveforms for future mobile applications", *IEEE Communications Magazine*, 2014.

[24] MiWEBA, *Millimetre-wave evolution for backhaul and access*, 2013-2016. [Online]. Available: https://www.miweba.eu/Start.

[25] G. XHaul, *Deliverable 3.1: Analysis of state of the art on scalable control plane design and techniques for user mobility awareness. definition of 5g-xhaul control plane requirements*, 2016. [Online]. Available: http://www.5g-xhaul-project.eu/.

[26] IEEE, *802.11ad-2012 - ieee standard for information technology–telecommunications and information exchange between systems–local and metropolitan area networks–specific requirements-part 11: Wireless lan medium access control (mac) and physical layer (phy) specifications amendment 3: Enhancements for very high throughput in the 60 ghz band*, 2012.

[27] ——, *Part 15.3c: Wireless medium access control (mac) and physical layer (phy) specifications for high rate wireless personal area networks (wpans)*, 2003.

[28] ——, *Task group ay*. [Online]. Available: http://www.ieee802.org/11/ Reports/tgay_update.htm.

[29] W. Hong, K. Baek, and S. Ko, "Millimeter-wave 5g antennas for smartphones: Overview and experimental demonstration", *IEEE Trans. on Antennas and Propagation*, 2017.

[30] B. Yu, K. Yang, C. Sim, and G. Yang, "A novel 28 ghz beam steering array for 5g mobile device with metallic casing application", *IEEE Trans. on Antennas and Propagation*, 2018.

[31] M.-T. Martinez-Ingles, J.-M.M.-G. Pardo, J.-V. Rodriguez, J. Pascual-Garcia, and L. J. Llacer, "Experimental comparison between centimeter and millimeter-wave ultrawideband radio channels", *Radio Science, Agu Publications*, 2014.

[32] C. Diakhate, J. Conrat, J. Cousin, and A. Sibille, "Millimeter-wave outdoor-to-indoor channel measurements at 3, 10, 17 and 60 ghz", *European Conference on Antennas and Propagation (EUCAP)*, 2017.

[33] E. Larsson, O. Edfors, and F. T.T. L. Marzetta, "Massive mimo for next generation wireless systems", *IEEE Communications Magazine*, 2014.

[34] J. Parson, *The Mobile Radio Channel*. Wiley, 2000.

[35] H. Bertoni, *Radio Propagation for Modern Wireless Systems*. Prentice Hal, 2000.

[36] N.-. Consortium. [Online]. Available: https://www.nsnam.org/.

[37] J. Proakis, *Digital Communications*. McGraw-Hill, 2000.

[38] A. Molisch, *Wireless Communications*. Wiley, 2011.

[39] A. Ishimaru, *Electromagnetic Wave Propagation, Radiation, and Scattering*. Prentice Hall, 1991.

[40] M. Sadiku, *Numerical Techniques in Electromagnetics*. CRC Press, 2000.

[41] F. Fuschini, E. Vitucci, M.Barbiroli, G. Falciasecca, and V. Degli-Esposti, "Ray tracing propagation modeling for future small-cell and indoor applications: A review of current techniques", *Radio Science, AGU Publications*, 2015.

[42] ITU-R, *P.833-8: Attenuation in vegetation*, 2013.

[43] ——, *P.676-10: Attenuation by atmospheric gases*, 2013.

[44] ——, *P.840-6: Attenuation due to clouds and fog*, 2013.

[45] ——, *P.838-3: Specific attenuation model for rain for use in prediction methods*, 2005.

[46] ——, *P.1238-8: Propagation data and prediction methods for the planning of indoor radiocommunication systems and radio local area networks in the frequency range 300 mhz to 100 ghz*, 2015.

[47] ——, *P.1411-8: Propagation data and prediction methods for planning of short-range outdoor radiocommunication systems and radio local area networks in the frequency range 300 mhz to 100 ghz*, 2015.

[48] C.Gustafson and F.Tufvesson, "Characterization of 60ghz shadowing by human bodies and simple phantoms", *European Conference on Antennas and Propagation (EuCAP)*, 2011.

[49] M. Jacob, S. Priebe, A. Maltsev, A. Lomayev, V. Erceg, and T. Kuerner, "A ray tracing based stochastic human blockage model for the ieee 802.11ad 60ghz channel model", *European Conference on Antennas and Propagation (EuCAP)*, 2011.

[50] M. Jacob, S. Priebe, T. Kuerner, M.Peter, M.Wisotzki, R.Felbecker, and W.Keusgen, "Fundamental analyses of 60ghz human blockage", *European Conference on Antennas and Propagation (EuCAP)*, 2013.

[51] C. Balanis, *Antenna Theory*. Wiley, 1997.

[52] A. Ludwig, "The definition of cross polarization", *IEEE Transactions on Antennas and Propagation*, 1973.

[53] J. Roy and L. Shafai, "Generalization of the ludwig-3 definition for linear copolarization and cross polarization", *IEEE Transactions on Antennas and Propagation*, 2001.

[54] H. Thompson, G. Siqueira, and R. Cole, "Polarization diversity for urban millimetric mobile radio communications: Comparison of initial propagation measurement results with prediction", *IEEE Vehicular Technology Conference (VTC)*, 1992.

[55] A. Kajiwara, "Indoor propagation measurements at 94 ghz", *IEEE Personal Indoor and Mobile Radio Communications Symposium (PIMRC)*, 1995.

[56] ——, "Effects of polarization, antenna directivity, and room size on delay spread in los indoor radio channel", *IEEE Transactions on Vehicular Technology*, 1997.

[57] T. Manabe, K. Sato, H. Masukawa, K. Taira, T. Ihara, Y. Kasashima, and K. Yamaki, "Polarization dependence of multipath propagation and high-speed transmission characteristics of indoor millimeter-wave channel at 60 ghz", *IEEE Transactions on Vehicular Technology*, 1995.

[58] T. Manabe, Y. Miura, and T. Ihara, "Effects of antenna directivity and polarization on indoor multipath propagation characteristics at 60 ghz", *IEEE Journal on Selected Areas in Communications*, 1996.

[59] A. Maltsev, E. Perahia, R. Maslennikov, A. Sevastyanov, A. Lomayev, and A. Khoryaev, "Impact of polarization characteristics on 60-ghz indoor radio communication systems", *IEEE Antennas an Wireless Propagation Letters*, 2010.

[60] C. Balanis, *Advanced Engineering Electromagnetics*. Wiley, 1989.

[61] J. Roy, "New results for the effective propagation constants of nonuniform plane waves at the planar interface of two lossy media", *IEEE Transactions on Antennas and Propagation*, 2003.

[62] W. Burnside and K. Burgener, "High frequency scattering by a thin lossless dielectric slab", *IEEE Transactions on Antennas and Propagation*, 1983.

[63] R. Kouyoumjian and P. Pathak, "A uniform geometrical theory of diffraction for an edge in a perfectly conducting surface", *Proceedings of the IEEE*, 1974.

[64] R. Lubbers, "Finite conductivity uniform gtd versus knife edge diffraction in prediction of propagation path loss", *IEEE Transactions on Antennas and Propagation*, 1984.

[65] ——, "Propagation prediction for hilly terrain using gtd wedge diffraction", *IEEE Transactions on Antennas and Propagation*, 1984.

[66] ——, "A heuristic utd slope diffraction coefficient for rough lossy wedges", *IEEE Transactions on Antennas and Propagation*, 1989.

[67] J. Pascual-Garcia, M.-T. Martinez-Ingles, J.-M. Molina-Garcia-Pardo, J.-V. Rodriguez, and V. Degli-Esposti, "Experimental parameterization of a diffuse scattering model at 60 ghz", *IEEE-APS Topical Conference on Antennas and Propagation in Wireless Communications (APWC)*, 2015.

[68] T. Elfouhaily and C. Guerin, "A critical survey of approximate scattering wave theories from random rough surfaces", *Waves Random Media, IOP*, 2004.

[69] P. Beckmann and A. Spizzichino, *The Scattering of Electromagnetic Waves from Rough Surfaces*. Artech House Radar Library, 1987.

[70] J. Harvey, A. Krywonos, and C. Vernold, "Modified beckmann-kirchoff scattering model for rough surfaces with large incident and scattering angles", *Optical Engineering, SPIE*, 2007.

[71] D. Didascalou, M. Doettling, N. Geng, and W. Wiesbeck, "An approach to include stochastic rough surface scattering into deterministic ray-optical wave propagation modeling", *IEEE Transactions on Antennas and Propagation*, 2003.

[72] M. Al-Nuaimi and M. Ding, "Prediction models and measurements of microwave signals scattered from buildings", *IEEE Transactions on Antennas and Propagation*, 1994.

[73] Y. Ouattara, E. Richalot, O. Picon, G. Kubicke, C.Bourlier, and J. Wiart, "Radiowaves scattering from irregular building facades through mom analysis", *European Conference on Antennas and Propagation (EuCAP)*, 2011.

[74] J. Ogilvy, *Theory of Wave Scattering From Random Rough Surfaces*. CRC Press, 1991.

[75] C. Jansen, S. Priebe, C. Moller, M. Jacob, H. Dierke, M. Koch, and T. Kuerner, "Diffuse scattering from rough surfaces in thz communication channels", *IEEE Transactions on Terahertz Science and Technology*, 2011.

[76] V. Degli-Esposti and H. Bertoni, "Evaluation of the role of diffuse scattering in urban microcellular propagation", *IEEE Vehicular Technology Conference (VTC)*, 1999.

[77] V. Degli-Esposti, "A diffuse scattering model for urban propagation prediction", *IEEE Transactions on Antennas and Propagation*, 2001.

[78] V. Degli-Esposti, D.Guiducci, A. de Marsi, P. Azzi, and F. Fuschini, "An advanced field prediction model including diffuse scattering", *IEEE Transactions on Antennas and Propagation*, 2004.

[79] V. Degli-Esposti, F. Fuschini, E. Vitucci, and G. Falciasecca, "Measurement and modelling of scattering from buildings", *IEEE Transactions on Antennas and Propagation*, 2007.

[80] V. Degli-Esposti, F. Fuschini, and E. Vitucci, "A fast model for distributed scattering from buildings", *European Conference on Antennas and Propagation (EuCAP)*, 2009.

[81] F. Fuschini, V. Degli-Esposti, and E. Vitucci, "A model for forward-diffuse scattering through a wall", *European Conference on Antennas and Propagation (EuCAP)*, 2010.

[82] E. Vitucci, F. Mani, V. Degli-Esposti, and C. Oestges, "A study on polarimetric properties of scattering from building walls", *IEEE Vehicular Technology Conference (VTC)*, 2010.

[83] L. Minghini, R. D Errico, V. Degli-Esposti, and E. Vitucci, "Electromagnetic simulation and measurement of diffuse scattering from building walls", *European Conference on Antennas and Propagation (EuCAP)*, 2014.

[84] F. Mani, F. Quintin, and C. Oestges, "Directional spreads of dense multipath components in indoor environments: Experimental validation of a ray tracing approach", *IEEE Transactions on Antennas and Propagation*, 2012.

[85]   ——, "Accuracy of depolarization and delay spread predictions using advanced ray-based modeling in indoor scenarios", *EURASIP Journal on Wireless Communications and Networking*, 2011.

[86]   F. Fuschini, H. El-Sallabi, V. Degli-Esposti, L. Vuokko, D. Guiducci, and P. Vainikainen, "Analysis of multipath propagation in urban environment through multidimensional measurements and advanced ray tracing simulation", *IEEE Transactions on Antennas and Propagation*, 2008.

[87]   E. Vitucci, F. Mani, V. Degli-Esposti, and C. Oestges, "Polarimetric properties of diffuse scattering from building walls: Experimental parametrization of a ray-tracing model", *IEEE Transactions on Antennas and Propagation*, 2012.

[88]   V. Degli-Esposti, V. Kilomonen, E. Vitucci, and P. Vainikainen, "Analysis and modeling on co and cross-polarized urban radio propagation for dual-polarized mimo wireless systems", *IEEE Transactions on Antennas and Propagation*, 2011.

[89]   E. Vitucci, V. Degli-Esposti, F. Fuschini, J. Lu, M. Barbiroli, J. Wu, M. Zoli, J. Zhu, and H. Bertoni, "Ray tracing rf field prediction: An unforgiving validation", *International Journal of Antennas and Propagation, Hindawi*, 2015. [Online]. Available: http://dx.doi.org/10.1155/2015/184608.

[90]   G. Athanasiadou and A. Nix, "Investigation into the sensitivity of the power predictions of a microcellular ray tracing propagation model", *IEEE Transactions on Vehicular Technology*, 2000.

[91]   F. Gil, Claro, J. Ferreira, C. Pardelinha, and L. Correia, "A 3d interpolation method for base-station-antenna radiation patterns", *IEEE Antennas and Propagation Magazine*, 2011.

[92]   T. Petrita and A. Ignea, "A new method for interpolation of 3d antenna pattern from 2d plane patterns", *IEEE International Symposium on Electronics and Telecommunications (ISETC)*, 2012.

[93]   A. Glassner, *An Introduction to Ray Tracing*. Kaufmann, 1989.

[94]   A. Petrin, T. Rick, and T. Kuhlen, *Wave Propagation in Materials for Modern Applications, Chapter 6: Accelerating Radio Wave Propagation Algorithms by Implementation on Graphics Hardware*. INTECH, 2010.

[95]   Y. Tao, H. Lin, and H. Bao, "Gpu-based shooting and bouncing ray method for fast rcs prediction", *IEEE Transactions on Antennas and Propagation*, 2010.

[96]   S. et al., "Millimeter-wave propagation: Characterization and modeling toward fifth generation systems", *IEEE Antennas and Propagation Magazine*, 2016.

[97]   M. Afsar, J. Birch, R. Clarke, and G. Chantry, "The measurement of the properties of materials", *IEEE Proceedings*, 1986.

[98]   M. Venkatesh and G. Raghavan, "An overview ïż£of dielectric properties measuring techniques", *Canadian Biosystems Engineering*, 2005.

[99]   A. Tech., *Basics of measuring the dielectric properties of materials - application note*. [Online]. Available: http://literature.cdn.keysight.com/litweb/pdf/5989-2589EN.pdf.

[100] Rohde and Schwarz, *Measurements of dielectric material properties - application note*, 2012. [Online]. Available: https://www.rohde-schwarz.com/us/applications/measurement-of-dielectric-material-properties-application-note_56280-15697.html.

[101] A. Boughriet, C. Legrand, and A. Chapoton, "Non-iterative stable transmission/reflection method for low-loss material complex permittivity determination", *IEEE Transactions on Microwave Theory and Techniques*, 1997.

[102] A. J. Canos-Marin, B. Garcia-Banos, J. M. Catala-Civera, F. L. Penaranda-Foix, and J. D. Gutierrez-Cano, "Improvement in the accuracy of dielectric measurement of open-ended coaxial resonators by an enhanced de-embedding of the coupling network", *IEEE Transactions on Microwave Theory and Techniques*, 2013.

[103] C. N. Works, T. W. Dakin, and F. W. Boggs, "A resonant-cavity method for measuring dielectric properties at ultrahigh frequencies", *Trans. Amer. Inst. Electr. Eng.*, 1944.

[104] D. K. Ghodgaonkar, V. V. Varadan, and V. K. Varadan, "Free-space measurement of complex permittivity and complex permeability of magnetic materials at microwave frequencies", *IEEE Transactions on Instrumentation and Measurement*, 1990.

[105] Z. Akhter and M. Akhtar, "Free-space time domain position insensitive technique for simultaneous measurement of complex permittivity and thickness of lossy dielectric samples", *IEEE Transactions on Instrumentation and Measurement*, 2016.

[106] G. Brancaccio, E. D Alterio, L. D. Stefano, L. D. Guida, M. Feo, and S. Luce, "A free-space method for microwave characterization of materials in aerospace application", *Proc. IEEE Metrology for Aerospace (MetroAeroSpace)*, 2014.

[107] J. Baker-Jarvis, E. J. Vanzura, and W. A. Kissick, "Improved technique for determining complex permittivity with the transmission-reflection method", *IEEE Transactions on Microwave Theory and Techniques*, 1990.

[108] P. Corona, G. Ferrara, and C. Gennarelli, "A new technique for free-space permittivity measurements of lossy dielectrics", *IEEE Transactions on Instrumentation and Measurement*, 1987.

[109] S. Kim, D. Novotny, J. A. Gordon, and J. R. Guerrieri, "A free-space measurement method for the low-loss dielectric characterization without prior need for sample thickness data", *IEEE Trans. Antennas and Propagation*, 2016.

[110] M. Born and E. Wolf, *Principles of Optics*. Pergamon, 1985.

[111] V. Degli-Esposti, M. Zoli, E. M. Vitucci, F. Fuschini, M. Barbiroli, and J. Chen, "A method for the electromagnetic characterization of construction materials based on fabry-perot resonance", *IEEE Access*, 2017. [Online]. Available: DOI: 10.1109/ACCESS.2017.2767278.

[112] M. Qi, Y. Bai, and B. Mi, "Fabry-perot-like resonance of a subwavelength single slit for measurement of permittivities of microcrystalline liquids and gases", *Progress In Electromagnetics Research Symposium (PIERS)*, 2016.

[113] D. Doyle, T. Starr, and C. Christodoulou, "Dielectric characterization of 3d printed materials with a confocal fabry-perot resonator for space utilization", *Proc. IEEE Antennas and Propagation Soc. Int. Symposium (APSURSI)*, 2014.

[114] W. B. Seo and J. J. Choi, "Dielectric measurements using fabry-perot open resonators at millimeter wave frequencies (26-110 ghz)", *Proc. 3rd IEEE Int. Vac. Electron. Conf. (IVELEC)*, 2002.

[115]   A. Kazemipour, M. Hudlicka, T. Kleine-Ostmann, and T. Schrader, "A reliable simple method to extract the intrinsic material properties in millimeter/submillimeter wave domain", *Proc. 29th Conf. Precision Electromagn. Meas. (CPEM)*, 2014.

[116]   S. Orfanidis, *Electromagnetic Waves and Antennas*. online, 2002. [Online]. Available: http://www.ece.rutgers.edu/orfanidi/ewa/.

[117]   ITU-R, *P.2040: Effects of building materials and structures on radiowave propagation above about 100 mhz*, 2015.

[118]   F. Fuschini, S. Haefner, M. Zoli, R. Mueller, E. M. Vitucci, D. Dupleich, M. Barbiroli, J. Luo, E. Schulz, V. Degli-Esposti, and R. S. Thomae, "Item level characterization of mm-wave indoor propagation", *Journal on Wireless Communications, EURASIP*, 2016. [Online]. Available: DOI10.1186/s13638-015-0502-3.

[119]   R. Mueller, S. Haefner, D. Dupleich, J. Luo, E. Schulz, and R. Herrmann, "Ultra-wideband channel sounder for measurements at 70 ghz", *IEEE V.T. Conf., Glasgow*, 2015.

[120]   D. Pena, R. Feick, H. Hristov, and W. Grote, "Measurement and modeling of propagation losses in brick and concrete walls for the 900 mhz band", *IEEE Trans. on Antennas and Propagation*, 2003.

[121]   E. Vitucci, F. Mani, C. Oestges, and V. Degli-Esposti, "Analysis and modeling of the polarization characteristics of diffuse scattering in indoor and outdoor radio propagation", *Conf. on Applied Electromagnetics and Communications*, 2013.

[122]   J. Lu, D. Steinbach, P. Cabrol, P. Pietraski, and R. Pragada, "Propagation characterization of an office building in the 60 ghz band", *European Conference on Antennas and Propagation (EuCAP)*, 2014.

[123]   I. Cuinas, J. Pugliese, A. Hammoudeh, and M. Sanchez, "Comparison of the electromagnetic properties of building materials at 5.8 ghz and 62.4 ghz", *IEEE Vehicular Technology Conference (VTC)*, 2000.

[124]   L. Correia and P. Frances, "Estimation of materials characteristics from power measurements at 60 ghz", *IEEE Personal Indoor and Mobile Radio Communications Symposium (PIMRC)*, 1994.

[125]   ITU-R, *P.1238-7: Propagation data and prediction methods for the planning of indoor radiocommunication systems and radio local area networks in the frequency range 900 mhz to 100 ghz*, 2012.

[126]   K. Korolev and M. Afsar, "Complex dielectric permittivity measurements of materials in millimeter waves", *IEEE Spectroscopy and Material Properties*, 2005.

[127]   N. Chahat, M. Zhadobov, R.Sauleau, and S. Alekseev, "New method for determining dielectric properties of skin and phantoms at millimeter waves based on heating kinetics", *IEEE Transactions on Microwave Theory and Techniques*, 2012.

[128]   D. Ferreira, I. Cuinas, R. Calderihna, and T. Fernandes, "A review on the electromagnetic characterisation of building materials at micro- and millimetre wave frequencies", *European Conference on Antennas and Propagation (EuCAP)*, 2014.

[129] V. Mohtashami and A. Shishegar, "Effects on inaccuracy of material permittivies on ray tracing results for site-specific indoor propagation modeling", *IEEE APS Topical Conference on Antennas and Propagation in Wireless Communications (APWC)*, 2013.

[130] A. Navarro, N. Cardona, and D. Guevara, "Measurement-based ray-tracing models calibration in urban environments", *IEEE Antennas and Propagation Society International Symposium (APSURSI)*, 2013.

[131] C. Yang, B. Wu, and C. Ko, "A ray-tracing method for modeling indoor wave propagation and penetration", *IEEE Transactions on Antennas and Propagation*, 1998.

[132] F. Layer, R. Kattenbach, and H. Fruchtig, "Modeling and analysis of dominant propagation effects in real indoor environment at 5.2 ghz", *IEEE International Symposium on Personal, Indoor and Mobile Radio Communications (PIMRC)*, 1998.

[133] J. Jemai, R. Piesiewicz, and T. Kuerner, "Calibration of an indoor radio propagation prediction model at 2.4ghz by measurements of the ieee 802.11b preamble", *IEEE Vehicular Technology Conference (VTC)*, 2005.

[134] I. Cuinas and M. Sanchez, "Building material characterization from complex transmittivity measurements at 5.8ghz", *IEEE Transactions on Antenna and Propagation*, 2000.

[135] E. Stone, *Nist construction automation program report no. 3 electromagnetic signal attenuation in construction materials*, 1997. [Online]. Available: https : / / www . nist . gov / publications / electromagnetic - signal - attenuation - construction-materials.

[136] B. Feitor, R.Caleirinha, T. Fernandes, D. Ferreira, and N. Leonor, "Estimation of dielectric concrete properties from power measurement at 18.7 and 60 ghz", *IET Loughborough Antennas and Propagation Conference (LAPC)*, 2011.

[137] W. Ellison, A. Balana, G. Delbos, K. Lamkaouchi, L. Emyard, C. Guillou, and C. Prigent, "New permittivity measurements of seawater", *Radio Science*, 1998.

[138] M. Fiacco, M. Parks, H. Radi, and S. Saunders, "Final report: Indoor propagation factors at 17 and 60ghz", *Centre for Communication Systems Research (CCSR), University of Surrey*, 1998.

[139] S. Stavrou and E. Saunders, "Review of constitutive parameters of building materials", *International Conference on Antennas and Propagation (ICAP)*, 2003.

[140] J. Shokou, S. Noghanian, and H. Keshavarz, "Reflection coefficient measurement for north american house flooring at 57-64 ghz", *IEEE Anntennas and Propagation Letters*, 2011.

[141] R. Felbecker, W. Keusgen, A. Kortke, and M. Peter, "Estimation of effective permittivity and effective thickness of inhomogeneous materials at 52-70 ghz", *European Conference on Antennas and Propagation*, 2009.

[142] A. Guraliuc, M. Zhadobov, O. D. Sagazan, and R. Sauleau, "Solid phantom for body-centric propagation measurements at 60 ghz", *IEEE Transactions on Microwave Theory and Techniques*, 2014.

[143] M. Ghaddar, L. Talbi, G. Delisle, and J. LeBel, "Deflecting-obstacle effects on signal propagation in the 60 ghz band", *IEEE Transactions on Antennas and Propagation*, 2013.

[144] R. Piesiewicz, T. Kleine-Ostmann, N. Krumbholz, D. Mittleman, M. Koch, and T. Kuerner, "Terahertz characterization of building materials", *IEEE Electronics Letters*, 2005.

[145] R. Piesiewicz, C. Jansen, S. Wietzke, D. Mittleman, M. Koch, and T. Kuerner, "Properties of building and plastic materials in the thz range", *International Journal of Infrared and Millimeter Waves, Springer*, 2007.

[146] C. Jansen, R. Piesiewicz, D. Mittleman, T. Kuerner, and M. Koch, "The impact of reflections from stratified building materials on the wave propagation in future indoor terahertz communication systems", *IEEE Transactions on Antennas and Propagation*, 2008.

[147] M. Peter, W. Keusgen, and R. Felbecker, "Measurement and ray-tracing simulation of the 60 ghz indoor broadband channel: Model accuracy and parametrization", *European Conference on Antennas and Propagation (EuCAP)*, 2007.

[148] R. Piesiewicz, C. Jansen, D. Mittleman, T. Kleine-Ostmann, M. Koch, and T. Kuerner, "Scattering analysis for the modeling of thz communication systems", *IEEE Transactions on Antennas and Propagation*, 2007.

[149] A.Fricke, S.Rey, M.Achir, P. L. Bars, T. Kleine-Ostmann, and T. Kuerner, "Reflection and transmission properties of plastic materials at thz frequencies", *International Conference on Infrared, Millimeter, and Terahertz Waves (IRMMW-THz)*, 2013.

[150] M. Zhadobov, N.Chahat, R. Sauleau, C. L. Quement, and Y. L. Drean, "Millimeter-wave interactions with the human body: State of knowledge and recent advances", *International Journal of Microwave and Wireless Technologies*, 2011.

[151] N. Chahat, M. Zhadobov, and R. Sauleau, "Broaband tissue-equivalent phantom for ban applications at millimeter waves", *IEEE Transactions on Microwave Theory and Techniques*, 2012.

[152] A. Guraliuc, M. Zhadobov, R. Sauleau, L. Marnat, and L. Dussopt, "Millimeter-wave electromagnetic field exposure from mobile terminals", *European Conference on Networks and Communications (EuCNC)*, 2015.

[153] A.Pellegrini, A.Brizzi, L.Zhang, K. Ali, Y. Hao, X. Wu, C. Costantinou, Y. Nechayev, P. Hall, N. Chahat, M. Zhadobov, and R. Sauleau, "Antennas and propagation for body-centric wireless communications at millimeter-wave frequencies: A review", *IEEE Antennas and Propagation Magazine*, 2013.

[154] M.-T. Martinez-Ingles, J. Pascual-Garcia, J.-V. Rodriguez, J.-M. Molina-Garcia-Pardo, L. Juan-Llacer, D. P. Gaillot, M. Lienard, and P. Degauque, "Indoor radio channel characterization at 60 ghz", *European Conference on Antennas and Propagation (EuCAP)*, 2013.

[155] M.-T. Martinez-Ingles, D. P. Gaillot, J. Pascual-Garcia, J.-M. Molina-Garcia-Pardo, M. Lienard, and J.-V. Rodriguez, "Deterministic and experimental indoor mmw channel modeling", *IEEE Antennas and Wireless Propagation Letters*, 2014.

[156] W. Fan, I. Carton, J. Nielsen, K. Olesen, and G. Pedersen, "Measured wideband characteristics of indoor channels at centimetric and millimetric bands", *Eurasip: Journal on Wireless Communications and Networking*, 2016.

[157] K. Haneda, J. Jarvelainen, A. Karttunen, M. Kyro, and J. Putkonen, "Statistical spatio-temporal radio channel model for large indoor environments at 60 and 70 ghz", *IEEE Trans. on Ant. and Propagat.*, 2015.

[158]   K. Haneda, "Channel models and beamforming at millimeter-wave frequency bands", *IEICE Trans. on Communications*, 2015.

[159]   F. Fuschini, S. Haefner, M. Zoli, R. Mueller, E. Vitucci, D. Dupleich, N. Barbiroli, J. Luo, E.Schulz, V. Degli-Esposti, and R. Thomae, "Analysis of in-room mm-wave propagation: Directional channel measurements and ray tracing simulations", *Journal of Infrared Millimeter and Teraherz Waves, Spinger*, 2017. [Online]. Available: DOI10.1007/s10762-017-0366-1.

[160]   E. M. Vitucci, F. Fuschini, and V. Degli-Esposti, "Ray tracing simulation of the radio channel time-and angle dispersion in large indoor environments", *EuCAP*, 2014.

[161]   F. Mani and C. Oestges, "Ray-tracing evaluation of diffuse scattering in outdoor scenario", *EUCAP*, 2011.

[162]   M. Jacob, S. Priebe, R. Dickhoff, T. Klein-Ostmann, T. Schrader, and T. Kuerner, "Diffraction in mm and sub mmwave indoor propagation channels", *IEEE Trans. on Microwave Theory and Tech*, 2012.

[163]   J. Jarvelainen, M. Kurkela, and K. Haneda, "Impacts of room structure models on the accuracy of 60 ghz indoor radio propagation prediction", *IEEE Antennas and Propagat. Letters*, 2015.

[164]   G. Foschini, "Layered space-time architecture for wireless communication in a fading environment when using multi-element antennas", *Bell Labs Technical Journal*, 1996.

[165]   G. Foschini, D. Chizhik, J. Gans, C. Papadias, and R. Valenzuela, "Analysis and performance of some basic space-time architectures", *IEEE Journal on Selected Areas in Communications*, 2003.

[166]   S. Alamouti, "A simple transmit diversity technique for wireless communications", *IEEE Journal on Selected Areas in Communications*, 1998.

[167]   V. Tarokh, N. Seshadri, and A. Calderbank, "Space-time codes for high data rate wireless communication: Performance criterion and code construction", *IEEE Transactions on Information Theory*, 1998.

[168]   G. Foschini and M. Gans, "On limits of wireless communications in a fading environment when using multiple antennas", *Wireless Personal Communications, Kluwer*, 1998.

[169]   E. Telatar, "Capacity of multi-antenna gaussian channels", *Transactions on Emerging Telecommunications Technologies, Wiley*, 1999.

[170]   T. Marzetta and B. Hochwald, "Capacity of a mobile multiple-antenna communication link in a rayleigh flat fading", *IEEE Transactions on Information Theory*, 1999.

[171]   A. Paulraj, D. Gore, R. Nabar, and H. Bolcskei, "An overview of mimo communications - a key to gigabit wireless", *Proceedings of the IEEE*, 2004.

[172]   V. Tarokh and H. J. an R.Calderbank, "Space-time block codes from orthogonal designs", *IEEE Transactions on Information Theory*, 1999.

[173]   T. M. an E.G. Larsson, H. Yang, and H. Q. Ngo, *Fundamentals of Massive MIMO*. Cambridge University Press, 2016.

[174]   A. Goldsmith, S. Jafar, N. Jindal, and S.Vishwanath, "Capacity limits of mimo channels", *IEEE Journal on Selected Areas in Communications*, 2003.

[175] J. Mietzner, R. Schober, L. Lampe, W. Gerstacker, and P. Hoeher, "Multiple-antenna techniques for wireless communications - a comprehensive literature survey", *IEEE Communications Surveys and Tutorials*, 2009.

[176] D. Brennan, "Linear diversity combining techniques", *Proceedings of the IRE*, 1959.

[177] J. Lemieux, M. El-Tanany, and H. Hafez, "Experimental evaluation of space - frequency - polarization diversity in the indoor wireless channel", *IEEE Transactions on Vehicular Technology*, 1991.

[178] P. Balaban and J. Salz, "Optimum diversity combining and equalization in digital data transmission with applications to cellular mobile radio", *IEEE Transactions on Communications*, 1992.

[179] D. Gesbert, M. Shafi, D. Shiu, P. Smith, and A. Naguib, "From theory to practice: An overview of mimo space-time coded wireless systems", *IEEE Journal on Selected Areas in Communications*, 2003.

[180] C. Oestges and B. Clerckx, *MIMO Wireless Communications: From Real-World Propagation to Space-Time Code Design*. Academic Press, 2007.

[181] L. Zheng and D. Tse, "Diversity and multiplexing: A fundamental tradeoff in multiple-antenna channels", *IEEE Transactions on Information Theory*, 2003.

[182] H. Bolcskei, M. Borgmann, and A. Paulraj, "Impact of the propagation environment on the performance of space-frequency coded mimo-ofdm", *IEEE Journal on Selected Areas in Communications*, 2003.

[183] Q. Spencer, A. Swindlehurst, and M. Haardt, "Zero-forcing methods for downlink spatial multiplexing in multiuser mimo channels", *IEEE Transactions on Signal Processing*, 2004.

[184] T. Yoo and A. Goldsmith, "On the optimality of multiantenna broadcast scheduling using zero-forcing beamforming", *IEEE Journal on Selected Areas in Communications*, 2006.

[185] G.Caire and S. Shamai, "On the achievable throughput of a multiantenna gaussian broadcast channel", *IEEE Transactions on Information Theory*, 2003.

[186] L. Lu, G. Y. Li, A. Swindlehurst, A. Ashikhmin, and R. Zhang, "An overview of massive mimo: Benefits and challenges", *IEEE Journal of Selected Topics in Signal Processing*, 2014.

[187] Q. He, L. Xiao, X. Zhong, and S. Zhou, "Performance of massive mimo with zero-forcing beamforming and reduced downlink pilots", *International Sysmposium on Wireless Personal Multimedia Communications (WMPC)*, 2014.

[188] F. Rusek, D. Persson, B. K. Lau, E. Larsson, T. L. Marzetta, O. Edfors, and F. Tufvesson, "Scaling up mimo: Opportunities and challenges with very large arrays", *IEEE Signal Processing Magazine*, 2012.

[189] A. Swindlehurst, E.Ayanoglu, P. Heydari, and F.Capolino, "Millimeter-wave massive mimo: The next wireless revolution?", *IEEE Communications Magazine*, 2014.

[190] S. Mumtaz, J. Rodriguez, and L. Dai, *mmWave Massive MIMO*. Elsevier, 2016.

[191] L. Godara, "Applications of antenna arrays to mobile communications, part i: Performance improvement, feasibility, and system considerations, part ii: Beam-forming and direction-of-arrival considerations", *Proceedings of the IEEE*, 1997.

[192] H. V. Trees, *Detection, Estimation, and Modulation Theory, Part IV, Optimum Array Processing*. Wiley, 2002.

[193] S. Sun, T. Rappaport, R. Heath, K. Nix, and S. Rangan, "Mimo for millimeter-wave wireless communications: Beamforming, spatial multiplexing, or both?", *IEEE Communications Magazine*, 2014.

[194] F. Zafari, A. Gkelias, and K. Leung, "A survey of indoor localization systems and technologies", *arXiv: Computer Science - Networking and Internet Architecture*, 2017.

[195] A. Yassin, Y. Nasser, M. Awad, A. Al-Dubai, R. Liu, C. Yuen, R. Raulefs, and E. Aboutanios, "Recent advances in indoor localization: A survey on theoretical approaches and applications", *IEEE Communications Surveys and Tutorials*, 2017.

[196] R. F. Brena, J. P. Garcia-Vazquez, C. E. Galvan-Tejada, D. Munoz-Rodriguez, C. Vargas-Rosales, and J.Fangmeyer, "Evolution of indoor positioning technologies: A survey", *Hindawi: Journal of Sensors*, 2017.

[197] IEEE, *Task group az, next generation positioning*. [Online]. Available: http://www.ieee802.org/11/Reports/tgaz_update.htm.

[198] M. Koivisto, A. Hakkarainen, M.Costa, P. Kela, K.Leppanen, and M. Valkama, "High-efficiency device positioning and location-aware communications in dense 5g networks", *IEEE Communication Magazine*, 2017.

[199] O. Bazan, "A survey on mac protocols for wireless ad-hoc networks with beamforming antennas", *IEEE Communications Surveys e Tutorials*, 2012.

[200] J. Palacios, D. D. Donno, and J. Widmer, "Tracking mm-wave channel dynamics: Fast beam training strategies under mobility", *arXiv: Computer Science - Networking and Internet Architecture*, 2016. [Online]. Available: https://arxiv.org/abs/1612.07957.

[201] T. Nitsche, A. Flores, E. Knightly, and J. Widmer, "Steering with eyes closed: Mm-wave beam steering without in-band measurement", *IEEE Conference on Computer Communications (INFOCOM)*, 2015.

[202] J. Singh and S. Ramakrishna, "On the feasibility of codebook-based beamforming in millimeter wave systems with multiple antenna array", *IEEE Transactions on Wireless Communications*, 2015.

[203] K. Hosoya, N. Prasad, K. Ramanchandran, N. Orinashi, S. Kishimoto, S. Rangarajan, and K. Maruhashi, "Multiple sector id capture (midc): A novel beamforming technique for 60-ghz band multi-gbps wlan/pan systems", *IEEE Transactions on Antennas and Propagation*, 2015.

[204] S. Kutty and D. Sen, "Beamforming for millimeter wave communications: An inclusive survey", *IEEE Communications Survey and Tutorials*, 2016.

[205] M. Kountouris, D. Gesbert, and T. Salzer, "Enhanced multiuser random beamforming: Dealing with not so large number of users cases", *IEEE Journal on Selected Areas in Communications*, 2008.

[206] S. Jun, D. Kim, and J. Kang, "User seletion for multi-user mmwave systems with phased-zero-forcing hybrid precoder", *IEEE Annual Consumer Communications and Networking Conference (CCNC)*, 2017.

[207] S. Hu and F. Rusek, "A generalized zero-forcing precoder for multiple antenna gaussian broadcast channels", *IEEE International Sysmposium of Information Theory (ISIT)*, 2017.

[208] V. Degli-Esposti, F. Fuschini, E. Vitucci, N. Barbiroli, M. Zoli, L. Tian, X. Yin, D. Duplecih, R. Mueller, C. Schneider, and R. Thomae, "Ray-tracing-based mm-wave beamforming assessment", *IEEE Access*, 2014. [Online]. Available: `DigitalObjectIdentifier10.1109/ACCESS.2014.2365991`.

[209] V. Degli-Esposti, F. Fuschini, E. Vitucci, M. Barbiroli, M. Zoli, D. Dupleich, R. Mueller, C. Schneider, and R. S. Thomae, "Polarimetric analysis of mm-wave propagation for advanced beamforming applications", *European Conference on Antennas and Propagation (EuCAP)*, 2015.

[210] E. E. 567, *Broadband radio access networks (bran); 60 ghz multiple-gigabit was/rlan systems; harmonized en covering the essential requirements of article 3.2 of the r and tte directive*, 2009.

[211] C. document Rec. ERC 7003, *Relating to the use of short range devices (srd)*, 2014. [Online]. Available: `http://www.ieee802.org/11/Reports/tgaz_update.htm`.

[212] S. Sun, G. R. MacCartney, M. K. Samimi, S. Nie, and T. S. Rappaport, "Millimeter wave multi-beam antenna combining for 5g cellular link improvement in new york city", *IEEE International Conference on Communications (ICC)*, 2014.

[213] D. Dupleich, J. Luo, S. Haefner, R. Mueller, C. Schneider, and R. Thomae, "A hybrid polarimetric wide-band beam-former architecture for 5g mm-wave communications", *Proceedings of the 20th International ITG Workshop onSmart Antennas (WSA)*, 2016.

[214] D. Pozar, *Microwave and RF Wireless Systems*. Wiley, 2001.

[215] T. Rappaport, J. Murdock, and F. Gutierrez, "State of the art in 60-ghz integrated circuits and systems for wireless communications", *Proceedings of the IEEE*, 2011.

[216] G. Auer, V. Giannini, C. Desset, I. Godor, P. Skillermark, M. Olsson, M. Imran, D. Sabella, M. Gonzalez, O. Blume, and A. Fehske, "How much energy is needed to run a wireless network?", *IEEE Wireless Communications*, 2011.

[217] J. Dunsmore, *Measuring Amplifiers*. Wiley, 2012.

[218] C. Bowick, *RF Circuit Design*. Newnes, 2007.

[219] W. Arden, M. Brillouet, P. Cogez, M. Graef, B. Huizig, and R. Mahnkopf, *Irc itrs: More-than-moore white paper*. [Online]. Available: `http://www.itrs2.net/uploads/4/9/7/7/49775221/irc-itrs-mtm-v23.pdf`.

[220] B. Razavi, *RF Microelectronics*. Prentice Hall, 2011.

[221] R. Romanofsky, *Array phase shifters: Theory and technology*, 2007.